

Journal: Monthly Notices of the Royal Astronomical Society  
Article doi: 10.1093/mnras/sty669  
Article title: True versus apparent shapes of bow shocks  
First Author: Jorge A. Tarango-Yong  
Corr. Author: William J. Henney



## INSTRUCTIONS

We encourage you to use Adobe's editing tools (please see the next page for instructions). If this is not possible, please list clearly in an e-mail. Please do not send corrections as track changed Word documents.

Changes should be corrections of typographical errors only. Changes that contradict journal style will not be made.

These proofs are for checking purposes only. They should not be considered as final publication format. The proof must not be used for any other purpose. In particular we request that you: do not post them on your personal/institutional web site, and do not print and distribute multiple copies. Neither excerpts nor all of the article should be included in other publications written or edited by yourself until the final version has been published and the full citation details are available. You will be sent these when the article is published.

- 1. Licence to Publish:** Oxford Journals requires your agreement before publishing your article. If you haven't already completed this, please sign in with your My Account information and complete the online licence form. Details on how to do this can be found in the Welcome to Oxford Journals email.
- 2. Permissions: Permission to reproduce any third party material in your paper should have been obtained prior to acceptance. If your paper contains figures or text that require permission to reproduce, please inform me immediately by email.**
- 3. Author groups:** Please check that all names have been spelled correctly and appear in the correct order. Please also check that all initials are present. Please check that the author surnames (family name) have been correctly identified by a pink background. If this is incorrect, please identify the full surname of the relevant authors. Occasionally, the distinction between surnames and forenames can be ambiguous, and this is to ensure that the authors' full surnames and forenames are tagged correctly, for accurate indexing online.
- 4. Figures:** If applicable, figures have been placed as close as possible to their first citation. Please check that they are complete and that the correct figure legend is present. Figures in the proof are low resolution versions that will be replaced with high resolution versions when the journal is printed.
- 5. Missing elements:** Please check that the text is complete and that all figures, tables and their legends are included.
- 6. Special characters and equations:** Please check that special characters, equations and units have been reproduced accurately.
- 7. URLs:** Please check that all web addresses cited in the text, footnotes and reference list are up-to-date.
- 8. Funding:** If applicable, any funding used while completing this work should be highlighted in the Acknowledgements section. Please ensure that you use the full official name of the funding body.
- 9. Manuscript tagging:** The information in the table that appears before your manuscript contains the manuscript information that will be captured in the tagging online. Please check that this information is accurate as it cannot be changed after publication. If any of the information is incorrect, please mark the changes onto the table.

AUTHOR QUERIES - TO BE ANSWERED BY THE CORRESPONDING AUTHOR

The following queries have arisen during the typesetting of your manuscript. Please answer these queries by marking the required corrections at the appropriate point in the text.

Query No.	Nature of Query	Author's Response
Q1	<p>Author: The figures have been processed according to the information you entered during the submission of your manuscript. Please note that there is a charge of £200 (+VAT) for publishing in colour in print. There is no charge to publish figures in black and white in print and in colour online. If you have already requested print colour figures or have now decided to have print colour figures please confirm that you are willing to pay the £200 (+VAT) charge. You will be invoiced upon publication.</p> <p>If you do not wish to have your figures published in colour in print, please confirm. Black and white versions of figures are provided at the end of the paper. Please check the black and white versions to assess their quality for the print version of the journal, please contact us if you have any concerns.</p>	
Q2	Author: Please supply email addresses for between one and three authors who are willing to correspond with readers and for their email address to be included in the article	
Q3	Author: To check that we have your surnames correctly identified and tagged (e.g. for indexing), we have coloured pink the names that we have assumed are surnames. If any of these are wrong, please let us know so that we can amend the tagging.	
Q4	Author: Please note that it is journal style to refer to 'our' Galaxy with a capital 'G' (e.g. in case of Galaxy, Galactic Centre or Galactocentric) and to other galaxies with a lowercase 'g'. Please check that all the notations in this paper are correct.	
Q5	Author: If you refer to any data bases in your paper, please note the journal policy for properly crediting those responsible for compiling the data base. Rather than citing only a URL, if at all possible please also cite a reference (and include it in the reference list), or if a reference is not available then the names of those who compiled the data base. Note that some data bases do provide guidelines on how they should be cited – please check for these and follow them in your paper where appropriate.	
Q6	Author: The MNRAS list of approved key words has been revised and updated. The new list is appended to these proofs. If you had previously selected key words from the old list, please now check them carefully against the new list in case they need to be changed, or there are new ones that you would like to add. If you had not previously selected key words from the MNRAS approved list, please now choose up to six from the new list.	
Q7	Author: Please check the figures in the PDF proof carefully.	
Q8	Author: Journal style rules state that vectors and tensors must be written in bold italic ( $\mathbf{X}$ ), matrices must be written in bold san serif ( $\mathbf{X}$ ) and scalars must be written in italic ( $X$ ). Please check carefully that the notations used throughout this paper are correct.	

<b>Query No.</b>	<b>Nature of Query</b>	<b>Author's Response</b>
<b>Q9</b>	Author: Please confirm whether the edits made to the sentence 'After completing this work, it was brought to our...' retain the intended sense.	
<b>Q10</b>	Author: When used to mean the numerical value '3.14', the Greek letter 'pi' must always be written in roman (i.e. 'π' rather than 'π'). Please check all the notations throughout the text carefully.	
<b>Q11</b>	Author: Please note that computer software/programming languages must be styled in SMALL CAPITAL LETTERS, according to journal style. Please check and correct this paper accordingly.	
<b>Q12</b>	Author: Please update this reference, if possible, with full details to be added to the references list.	
<b>Q13</b>	Author: Please list all the authors if eight or fewer.	
<b>Q14</b>	Author: Please check whether the reference is okay as set.	
<b>Q15</b>	Author: Please check whether the reference is okay as set.	

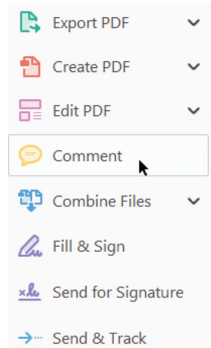
## MAKING CORRECTIONS TO YOUR PROOF

These instructions show you how to mark changes or add notes to your proofs using Adobe Acrobat Professional versions 7 and onwards, or Adobe Reader DC. To check what version you are using go to **Help** then **About**. The latest version of Adobe Reader is available for free from [get.adobe.com/reader](http://get.adobe.com/reader).

### DISPLAYING THE TOOLBARS

#### Adobe Reader DC

In Adobe Reader DC, the Comment toolbar can be found by clicking 'Comment' in the menu on the right-hand side of the page (shown below).

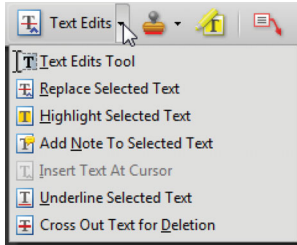


The toolbar shown below will then display along the top.



#### USING TEXT EDITS AND COMMENTS IN ADOBE

This is the quickest, simplest and easiest method both to make corrections, and for your corrections to be transferred and checked.



##### 1. Click Text Edits

2. Select the text to be annotated or place your cursor at the insertion point and start typing.
3. Click the **Text Edits** drop down arrow and select the required action.

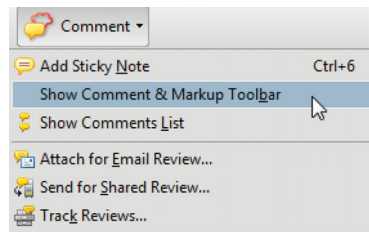
You can also right click on selected text for a range of commenting options, or add sticky notes.

#### SAVING COMMENTS

In order to save your comments and notes, you need to save the file (**File, Save**) when you close the document.

#### Acrobat Professional 7, 8, and 9

In Adobe Professional, the Comment toolbar can be found by clicking 'Comment(s)' in the top toolbar, and then clicking 'Show Comment & Markup Toolbar' (shown below).



The toolbar shown below will then be displayed along the top.



#### USING COMMENTING TOOLS IN ADOBE READER

All commenting tools are displayed in the toolbar. You cannot use text edits, however you can still use highlighter, sticky notes, and a variety of insert/replace text options.



#### POP-UP NOTES

In both Reader and Acrobat, when you insert or edit text a pop-up box will appear. In **Acrobat** it looks like this:



In **Reader** it looks like this, and will appear in the right-hand pane:



**DO NOT MAKE ANY EDITS DIRECTLY INTO THE TEXT, USE COMMENTING TOOLS ONLY.**

Element	Included in this paper
<b>Manuscript category</b>	Article
<b>Funder ID</b>	None
<b>Orcid IDs</b>	None
<b>Contributors</b>	Jorge A. <a href="#">Tarango-Yong</a> , William J. <a href="#">Henney</a>
<b>Supplementary data files cited</b>	None
<b>Related article(s)</b>	
<b>Corresponding author</b>	William J. <a href="#">Henney</a>
<b>Title</b>	True versus apparent shapes of bow shocks
<b>Keywords</b>	<a href="#">hydrodynamics</a> , circumstellar matter, stars: winds, outflows
<b>Collection ID</b>	

# True versus apparent shapes of bow shocks

Q1

Q2  
5 Jorge A. Tarango-Yong and William J. Henney\*

Q3 Instituto de Radioastronomía y Astrofísica, Universidad Nacional Autónoma de México, Apartado Postal 3-72, 58090 Morelia, Michoacán, México

10 Accepted 2018 March 9. Received 2018 March 8; in original form 2017 December 6

67

72

## ABSTRACT

Astrophysical bow shocks are a common result of the interaction between two supersonic plasma flows, such as winds or jets from stars or active galaxies, or streams due to the relative motion between a star and the interstellar medium. For cylindrically symmetric bow shocks, we develop a general theory for the effects of inclination angle on the apparent shape. We propose a new two-dimensional classification scheme for bow shapes, which is based on dimensionless geometric ratios that can be estimated from observational images. The two ratios are related to the flatness of the bow's apex, which we term *planitude*, and the openness of its wings, which we term *alatitude*. We calculate the expected distribution in the planitude–latitude plane for a variety of simple geometrical and physical models: quadrics of revolution, wilkinoids, cantoids, and ancantoids. We further test our methods against numerical magnetohydrodynamical simulations of stellar bow shocks and find that the apparent planitude and alatitude measured from infrared dust continuum maps serve as accurate diagnostics of the shape of the contact discontinuity, which can be used to discriminate between different physical models. We present an algorithm that can determine the planitude and alatitude from observed bow shock emission maps with a precision of 10 to 20 per cent.

77

82

87

92

Key words: hydrodynamics – circumstellar matter – stars: winds, outflows.

97

## 1 INTRODUCTION

The archetypal bow shock is formed when a solid body moves supersonically through a compressible fluid. Terrestrial examples include the atmospheric re-entry of a space capsule, or the sonic boom produced by a supersonic jet (van Dyke 1982). In astrophysics, the term bow shock is employed more widely, to refer to many different types of curved shocks that have approximate cylindrical symmetry. Instead of a solid body, astrophysical examples usually involve the interaction of *two* supersonic flows, such as the situation of a stellar wind emitted by a star that moves supersonically through the interstellar medium (van Buren & McCray 1988; Kobulnicky, Gilbert & Kiminki 2010; van Marle et al. 2011; Mackey et al. 2012, 2015). In such cases, two shocks are generally produced, one in each flow. Sometimes, especially in heliospheric studies (Zank 1999; Scherer & Fichtner 2014), the term ‘bow shock’ is reserved for the shock in the ambient medium, with the other being called the ‘wind shock’ or ‘termination shock’. However, in other contexts such as colliding wind binaries (Stevens, Blondin & Pollock 1992; Gayley 2009), such a distinction is not so useful. A further class of astrophysical bow shock is driven by highly collimated, supersonic jets of material, such as the Herbig–Haro objects (Schwartz 1978; Hartigan, Raymond & Hartmann 1987) that are powered by jets from young stars or protostars. Additional examples are seen in planetary

nebulae (Phillips, Cuesta & Ramos-Larios 2010; Meaburn, Boumis & Akras 2013), active galaxies (Wilson & Ulvestad 1987), and in galaxy clusters (Markevitch et al. 2002). In the jet-driven case, the term ‘working surface’ is often applied to the entire structure comprising the two shocks plus the shocked gas in between them, separated by a *contact discontinuity*. The working surface may be due to the interaction of the jet with a relatively quiescent medium, or may be an ‘internal working surface’ within the jet that is due to supersonic temporal variations in the flow velocity (Raga et al. 1990).

102

107

In empirical studies, the relationship between these theoretical constructs and the observed emission structures is not always clear. In such cases, the term ‘bow shock’ is often used in a more general sense to refer to the entire arc of emission. In this paper, we will concentrate on *stellar bow shocks*, in which the position of the star can serve as a useful reference point for describing the bow shape. The empirical terminology that we will employ is illustrated in Fig. 1. The *apex* is the point of closest approach of the bow to the star, which lies on the approximate symmetry axis, and the region around the apex is sometimes referred to as the *head* of the bow. The *wings* are the swept-back sides of the bow, which lie in a direction from the star that is orthogonal to the axis, with the *far wings* being the wing region farthest from the apex. Finally, the *tail* is the region near the axis but in the opposite direction from the apex. Fig. 2 shows an idealized schematic of how a double bow shock shell is formed from the interaction of two supersonic streams: an *inner wind* and an *outer wind*, with the inner wind being the weaker of the two (in

Q7

112

117

122

\* E-mail: w.henney@astrosmo.unam.mx

129

134

139

144

196

201

206

211

216

221

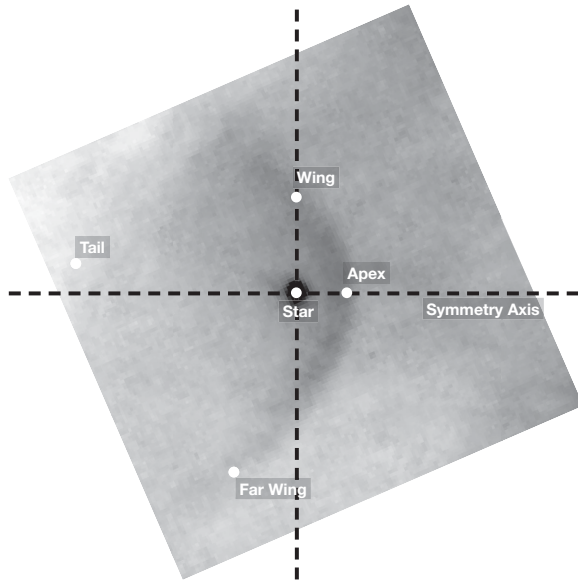
226

231

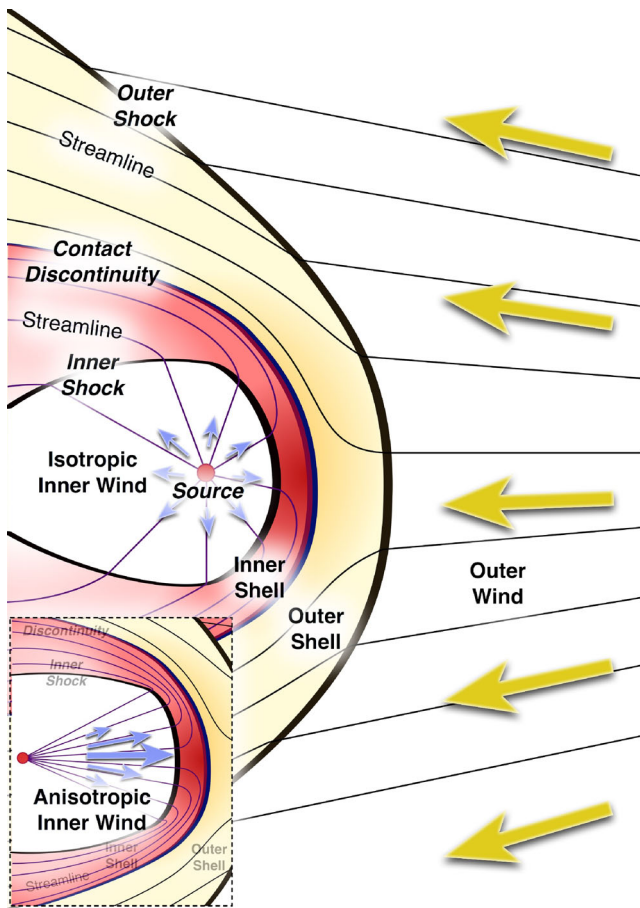
236

241

246



**Figure 1.** Descriptive terminology for a stellar bow shock. The apex is the closest approach of the bow to the star, while the wings are the parts of the bow that curve back past the star.

COLOUR ONLINE,  
B&W IN PRINT

**Figure 2.** Quasi-stationary bow shock structure formed by the interaction of two supersonic winds. Lower-left inset box shows the case where the inner wind is anisotropic. The streamlines (thin lines) are drawn to be qualitatively realistic: they are straight in regions of hypersonic flow, but curved in subsonic regions, responding to pressure gradients in the shocked shells. Streamline slopes are discontinuous across oblique shocks.

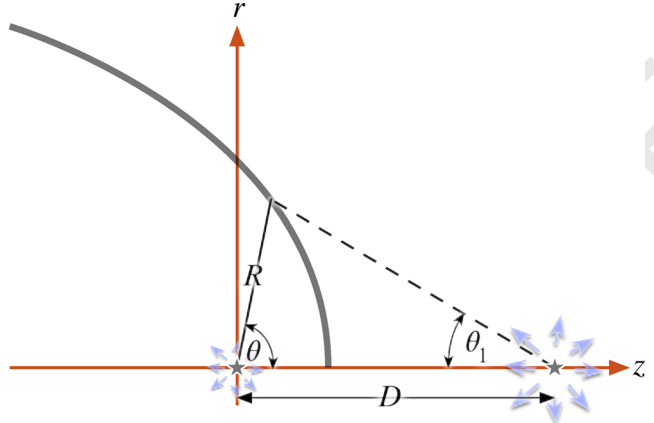


**Figure 3.** Schematic diagram of cylindrically symmetric two-wind interaction problem in the thin-shell limit, following Canto, Raga & Wilkin (1996).

terms of momentum), so that the shell curves back around the inner source. The outer wind may be from another star, or may be a larger scale flow of the interstellar medium, such as the *champagne flow* produced by the expansion of an H II region away from a molecular cloud (Tenorio-Tagle 1979; Shu et al. 2002; Medina et al. 2014). Alternatively, it may be due to the supersonic motion of the inner source through a relatively static medium, in which case the outer wind will not be divergent as shown in the figure but rather plane parallel. The thickness of the shocked shells at the apex depends on the Mach number,  $\mathcal{M}$ , of the flows and the efficiency of the post-shock cooling. For sufficiently strong cooling, the post-shock cooling zone thickness is negligible and the shock can be considered isothermal. In this case, the shell thickness is of the order of  $\mathcal{M}^{-2}$  times the source-apex separation (Henney 2002), which can become very small for high Mach numbers. The shell thickness will tend to increase towards the wings, due to the increasing shock obliqueness, which reduces the perpendicular Mach number. In the extreme thin-shell limit, the entire bow structure can be treated as a surface. The bow radius measured from the inner source (star) is  $R(\theta, \phi)$ , where  $\theta$  is the polar angle, measured from the star-apex axis, and  $\phi$  is the azimuthal angle, measured around that axis. Assuming cylindrical symmetry about the axis, this reduces to  $R(\theta)$ , which is illustrated in Fig. 3, following Canto et al. (1996). The separation between the two sources is  $D$  and the complementary angle, as measured at the position of the outer source, is  $\theta_1$ . The minimum value of  $R(\theta)$  is the stagnation radius,  $R_0$ , which occurs at the apex ( $\theta = 0$ ). In a steady state, ram-pressure balance on the axis implies that

$$\frac{R_0}{D} = \frac{\beta^{1/2}}{1 + \beta^{1/2}}, \quad (1)$$

where  $\beta$  is the momentum ratio between the two winds. If the winds are isotropic, with inner wind mass-loss rate  $\dot{M}_w$  and terminal velocity  $V_w$ , while the outer wind has corresponding values  $\dot{M}_{w1}$  and  $V_{w1}$ , then the momentum ratio is

$$\beta = \frac{\dot{M}_w V_w}{\dot{M}_{w1} V_{w1}}. \quad (2)$$

The case where the outer wind is a parallel stream (Wilkin 1996) corresponds to the limit  $\beta \rightarrow 0$ , in which case  $D$  is no longer a meaningful parameter.

The paper is organized as follows. In Section 2, we outline the geometric parameters that are necessary for describing bow shapes and introduce two dimensionless ratios: planitude and alatitude. In Section 3, we derive general results for the projection of bow

258

263

268

273

278

283

288

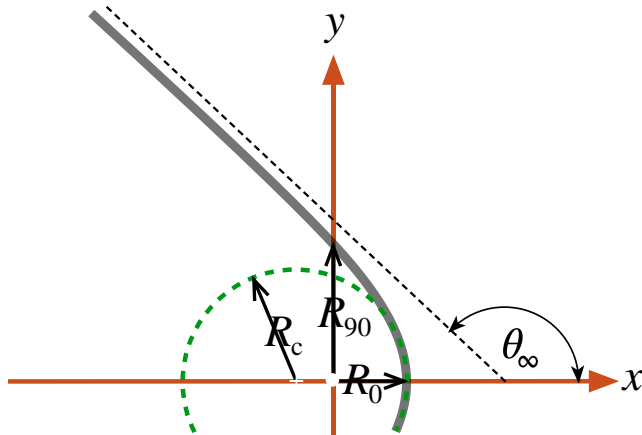


**Figure 4.** Parameters for characterizing a bow shape. Bow radius from the star, measured parallel ( $R_0$ ) and perpendicular ( $R_{90}$ ) to the symmetry axis, together with radius of curvature ( $R_c$ ) at apex and asymptotic opening angle ( $\theta_\infty$ ) of the far wings.

shapes on to the plane of the sky. In Section 4, we apply the results to the simplest possible class of geometric bow models: the quadrics of revolution, which comprise spheroids, paraboloids, and hyperboloids, each of which occupies a distinct region of the planitude–alatitude plane. In Section 5, we consider thin-shell hydrodynamic models for the parallel-stream case (wilkinoids) and wind–wind case (cantoids), including extension to an anisotropic inner wind (ancantoids). We calculate the location of the models in the planitude–alatitude plane as a function of the inclination of the bow shock axis to the plane of the sky. In Section 6, we test our methods against the results of more realistic numerical simulations of bow shocks, including the derivation of the shape parameters from maps of infrared dust emission. In Section 7, we apply our methods to example observations of proplyd bow shocks in the Orion nebula, paying close attention to the systematic uncertainties that arise when our algorithms are applied to real data. In Section 8, we summarize our results and outline how following papers will apply these ideas to a more extensive set of observations, models, and numerical simulations.

## 2 PLANITUDE AND ALATITUDE OF BOW SHAPES

The stagnation radius  $R_0$  describes the linear scale of the bow shock, but in order to characterize its shape, more parameters are required. To efficiently capture the diversity of bow shapes, we propose the parameters shown in Fig. 4. The perpendicular radius  $R_{90}$  is the value of  $R(\theta)$  at  $\theta = 90^\circ$ , whereas  $R_c$  is the radius of curvature of the bow at the apex ( $\theta = 0$ ). For a cylindrically symmetric bow, we show in Appendix A that this is given by

$$R_c = \frac{R_0^2}{R_0 - R_{\theta\theta,0}}, \quad (3)$$

where  $R_{\theta\theta,0}$  is  $d^2R/d\theta^2$  evaluated at  $\theta = 0$ .

A fourth parameter is the asymptotic opening angle of the far wings,  $\theta_\infty$ , which is useful in the case that the wings are asymptotically conical. However, in many bow shocks, the wings tend towards the asymptotic angle only slowly, making  $\theta_\infty$  difficult to measure, especially since the emission from the far wings is often weak at best. In contrast, the three radii,  $R_0$ ,  $R_{90}$ , and  $R_c$ , are straightforward to determine from observations. One simple method to estimate the

radius of curvature is to make use of the Taylor expansion<sup>1</sup> of  $R(\theta)$  about the apex (with  $\theta$  in radians):

$$R(\theta) = R_0 + \frac{1}{2} R_{\theta\theta,0} \theta^2 + \mathcal{O}(\theta^4), \quad (4)$$

so that fitting a polynomial in  $\theta^2$  to  $R(\theta)$  for  $|\theta| < \Delta\theta$  yields  $R_0$  and  $R_{\theta\theta,0}$  from the first two coefficients, and hence  $R_c$  from equation (3). Experience has shown that  $\Delta\theta = 30^\circ$ , and three terms in the polynomial are good choices, where the third term is used only as a monitor (if the coefficient of  $\theta^4$  is not small compared with  $R_0$ , then it may indicate a problem with the fit).

Since we have three radii, we can construct two independent dimensionless parameters:

$$\text{Planitude } \Pi \equiv \frac{R_c}{R_0} \quad (5)$$

$$\text{Alatitude } \Lambda \equiv \frac{R_{90}}{R_0}, \quad (6)$$

and these will be the principal shape parameters that we will use in the remainder of the paper. The *planitude*,  $\Pi$ , is a measure of the flatness of the head of the bow around the apex, while the *alatitude*,  $\Lambda$ , is a measure of the openness of the bow wings. Although ‘planitude’ can be found in English dictionaries, ‘alatitude’ is a new word that we introduce here, derived from the Latin *ala* for ‘wing’.

Several previous studies have discussed the relation between  $R_{90}$  and  $R_0$  as a diagnostic of bow shape (e.g. Robberto et al. 2005; Cox et al. 2012; Meyer et al. 2016), but as far as we know, we are the first to include  $R_c$ . Robberto et al. (2005, section 4.2) use the ratios  $R_0/D$  and  $R_{90}/D$  in analysing proplyd bow shapes in the Trapezium cluster in the centre of the Orion nebula (Hayward, Houck & Miles 1994; García-Arredondo, Henney & Arthur 2001; Smith et al. 2005). In that case, the source of the outer wind is known, and so  $D$  is well determined (at least, in projection), but for many bow shocks  $D$  is not known, and is not even defined for the moving-star or parallel-stream case. Cox et al. (2012, section 4.1) compare the observed shapes of bow shocks around cool giant stars with an analytic model, and use  $A$  and  $B$  for the projected values of  $R_0$  and  $R_{90}$ , respectively (see the next section for discussion of projection effects). Meyer et al. (2016, section 3.2) analyse the distribution of  $R_0/R_{90}$  (the reciprocal of our  $\Lambda$ ) for hydrodynamic simulations of bow shocks around runaway OB stars.

## 3 PROJECTION ON TO THE PLANE OF THE SKY

In this section, we calculate the apparent shape on the plane of the sky of the limb-brightened border of a shock or shell that is idealized as an arbitrary cylindrically symmetric surface.

### 3.1 Frames of reference

Consider body-frame Cartesian coordinates  $(x, y, z)$ , where  $x$  is the symmetry axis, and spherical polar coordinates  $(R, \theta, \phi)$ , where  $\theta$  is the polar angle and  $\phi$  the azimuthal angle. Since the surface is

<sup>1</sup> This method assumes both that  $R(\theta)$  is even (true for a cylindrically symmetric bow) and that the orientation of the axis is already known. Generalization to the cases where these assumptions do not hold is discussed in Appendix E.

382

387

392

397

402

Q8

407

412

417

422

427

432

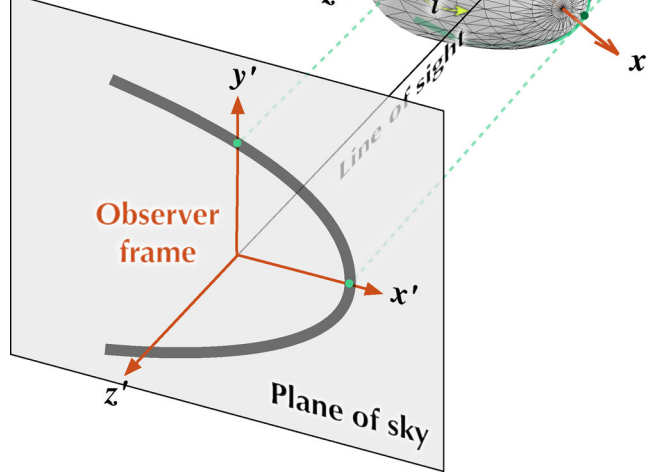


**Figure 5.** Relationship between body frame (unprimed coordinates) and observer frame (primed coordinates). Note that the plane of the sky is a projective plane, not a geometric plane in Euclidean 3-space, see discussion in the text.

cylindrically symmetric, it is can be specified as  $R = R(\theta)$ , so that Cartesian coordinates on the surface are

$$\mathbf{r} \equiv \begin{pmatrix} x \\ y \\ z \end{pmatrix} = \begin{pmatrix} R(\theta) \cos \theta \\ R(\theta) \sin \theta \cos \phi \\ R(\theta) \sin \theta \sin \phi \end{pmatrix}. \quad (7)$$

Suppose that the viewing direction makes an angle  $i$  with the  $z$ -axis, so that we can define observer-frame coordinates  $(x', y', z')$ , which are found by rotating the body-frame coordinates about the  $y$ -axis. The same vector,  $\mathbf{r}$ , expressed in the observer frame is then

$$\mathbf{r} = \begin{pmatrix} x' \\ y' \\ z' \end{pmatrix} = \mathbf{A}_y(i) \begin{pmatrix} x \\ y \\ z \end{pmatrix} = \begin{pmatrix} x \cos i - z \sin i \\ y \\ z \cos i + x \sin i \end{pmatrix}, \quad (8)$$

where the rotation matrix  $\mathbf{A}_y(i)$  is given in Appendix B. The inclination angle  $i$  is defined so that  $i = 0^\circ$  when the surface is viewed perpendicular to its axis (*side on*) and  $i = \pm 90^\circ$  when it is viewed along its axis (*end on*), with positive  $i$  when the apex points towards the observer.

The relationship between the two frames is illustrated in Fig. 5. All quantities in the observer's frame are denoted by attaching a prime to the equivalent quantity in the body frame. There are two ways of interpreting the primed coordinates. On the one hand, the 3-vector  $(x', y', z')$  specifies a point in Euclidean space,  $\mathbb{R}^3$ , but an alternative interpretation is to take the 2-vector  $(x', y')$  as specifying a point in a *projective space*,  $\mathbb{P}^2$  (see e.g. section 15.6 of Penrose 2004). Each ‘point’ in  $\mathbb{P}^2$  is equivalent to a line in  $\mathbb{R}^3$ , specifically: a line of sight that passes through the observer. Thus,  $(x', y')$  gives the celestial coordinates on the *plane of the sky*, with  $x'$  being the projected symmetry axis of the surface. We assume that the observer is located at a very large distance, relative to the size of the

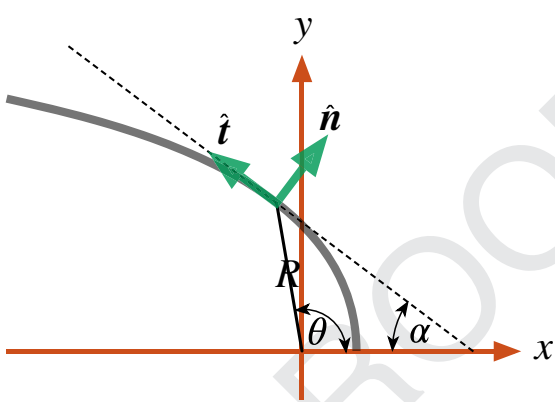


**Figure 6.** Unit vectors in the body frame that are normal and tangential to the surface  $R(\theta)$  in a plane of constant azimuth,  $\phi$ .

bow, so that all lines of sight are effectively parallel to the  $z'$ -axis, with the observer at  $z' = -\infty$ . But, from the point of view of the plane of the sky, the  $z'$  coordinate is strictly irrelevant since it is a projective plane, and not a Euclidean plane. In the following, we will switch between the  $\mathbb{R}^3$  and  $\mathbb{P}^2$  interpretations as convenient, resolving ambiguity where necessary via the adjectives ‘Euclidean’ for  $\mathbb{R}^3$  and ‘plane-of-sky’ or ‘projected’ for  $\mathbb{P}^2$ .

444

445

459

### 3.2 Unit vectors normal and tangential to the surface

We define unit vectors  $\hat{n}$ ,  $\hat{t}$ , such that  $\hat{n}$  is normal to the surface, while  $\hat{t}$  is tangent to the surface in a plane of constant  $\phi$ . For  $\phi = 0$ , the surface lies in the  $xy$  plane and it is straightforward to show (Fig. 6) that in this case the unit vectors are given by

$$\hat{t}_0 = \begin{pmatrix} -\cos \alpha \\ \sin \alpha \\ 0 \end{pmatrix} \quad \text{and} \quad \hat{n}_0 = \begin{pmatrix} \sin \alpha \\ \cos \alpha \\ 0 \end{pmatrix}, \quad (9)$$

where  $\alpha$  is the *slope angle*, given by

$$\tan \alpha = - \left. \frac{dy}{dx} \right|_{R(\theta)} = \frac{1 + \omega \tan \theta}{\tan \theta - \omega} \quad (10)$$

and  $\omega$  is a dimensionless *local growth factor*:

$$\omega(\theta) = \frac{1}{R} \frac{dR}{d\theta}. \quad (11)$$

For general  $\phi \neq 0$ , we find  $\hat{n}$  and  $\hat{t}$  by rotating equations (9) around the  $x$ -axis with the matrix  $\mathbf{A}_x(\phi)$  (equation B5):

$$\hat{n} = \mathbf{A}_x(\phi) \hat{n}_0 = \begin{pmatrix} \sin \alpha \\ \cos \alpha \cos \phi \\ \cos \alpha \sin \phi \end{pmatrix} \quad (12)$$

$$\hat{t} = \mathbf{A}_x(\phi) \hat{t}_0 = \begin{pmatrix} -\cos \alpha \\ \sin \alpha \cos \phi \\ \sin \alpha \sin \phi \end{pmatrix}. \quad (13)$$

484

489

### 3.3 Tangent line

The boundary on the plane of the sky of the projected surface is the locus of those lines of sight that graze the surface tangentially. This corresponds to a curved line on the surface itself, which we denote the *tangent line*, and which is defined by the condition

$$\hat{n} \cdot \hat{z}' = 0. \quad (14)$$

494

We denote by  $\phi_T$  that value of  $\phi$  that satisfies this relation for a given inclination,  $i$ , and polar angle,  $\theta$ . From equations (12), (14), (B4), and (10), this is

$$501 \quad \sin \phi_T = -\tan i \tan \alpha = \tan i \frac{1 + \omega \tan \theta}{\omega - \tan \theta}. \quad (15)$$

From equations (7) and (8) it follows that the observer-frame coordinates of the tangent line are given by

$$506 \quad \begin{pmatrix} x'_T \\ y'_T \\ z'_T \end{pmatrix} = R(\theta) \begin{pmatrix} \cos \theta \cos i - \sin \theta \sin \phi_T \sin i \\ \sin \theta (1 - \sin^2 \phi_T)^{1/2} \\ \cos \theta \sin i + \sin \theta \sin \phi_T \cos i \end{pmatrix}. \quad (16)$$

Note that, in general,  $z'_T$  is not a linear function of  $x'_T$  and  $y'_T$ , so that the tangent line  $(x'_T, y'_T, z'_T)$  is not a plane curve in three-dimensional Euclidean space,  $\mathbb{R}^3$ . However, for the projected shape  $(x'_T, y'_T)$  of the tangent line on the plane of the sky,  $\mathbb{P}^2$ , the value of  $z'_T$  does not matter (see above). The projected shape can also be described in polar form as  $R'(\theta')$ , where

$$516 \quad R' = (x'_T^2 + y'_T^2)^{1/2} \quad \text{and} \quad \tan \theta' = y'_T / x'_T. \quad (17)$$

Equation (15) will not have a solution for arbitrary values of  $\theta$  and  $i$ , but only when  $|\tan i \tan \alpha| < 1$ . In particular, if  $i \neq 0$ , then the tangent line only exists for  $\theta > \theta_0$ , where  $\theta_0$  is the value of  $\theta$  on the tangent line's projected symmetry axis ( $\theta' = 0$ ). From equations (16) and (17), it follows that  $\sin^2 \phi_T = 1$  at  $\theta = \theta_0$ , which yields the implicit equation

$$526 \quad \tan \theta_0 = \frac{|\tan i| + \omega(\theta_0)}{1 - \omega(\theta_0)|\tan i|}. \quad (18)$$

In addition, if the surface is sufficiently ‘open’ ( $\alpha \geq \alpha_{\min} > 0$  for all  $\theta$ ), then for those inclinations with  $|i| > (90^\circ - \alpha_{\min})$  the tangent line does not exist for any value of  $\theta$ . In other words, when the viewing angle is sufficiently close to face-on, the projected surface has no ‘edge’ and will no longer look like a bow shock to the observer.

Q9 After completing this work, it was brought to our attention that the principal results of this section had already been derived in appendix B of the PhD thesis by Wilkin (1997). For instance, Wilkin’s equation 8 is equivalent (apart from differences in notation) to our equation (15).

### 3.4 Characteristic radii on the plane of the sky

In order to compare the shell shape given by  $R(\theta)$  with observations, it is convenient to define the following apparent radii in the observer frame:  $R'_0$  and  $R'_{90}$ . These are projected distances of the shell tangent line from the origin. The first is measured in the direction of the symmetry axis, and the second in a perpendicular direction. More concretely  $R'_0 = x'_T(y'_T = 0)$  and  $R'_{90} = y'_T(x'_T = 0)$ . From equations (15) and (16), we find that

$$546 \quad R'_0 = R(\theta_0) \cos(\theta_0 + i). \quad (19)$$

Here  $\theta_0$  is the solution of equation (18), and

$$551 \quad R'_{90} = R(\theta_{90}) \sin \theta_{90} (1 - \sin^2(\phi_T(\theta_{90})))^{1/2}, \quad (20)$$

where  $\theta_{90}$  is the solution of the implicit equation:

$$556 \quad \cot \theta_{90} = \frac{1 - (1 + \omega(\theta_{90})^2 \sin^2 2i)^{1/2}}{2\omega(\theta_{90}) \cos^2 i}. \quad (21)$$

The projected alatitude (see Section 2) is then given by  $\Lambda' = R'_{90}/R'_0$ .

Similarly, the projected planitude is  $\Pi' = R'_c/R'_0$ , where  $R'_c$  is found by applying the equivalent of equation (3) for primed quantities:

$$563 \quad R'_c = \frac{(R'_0)^2}{R'_0 - R'_{\theta'\theta',0}}. \quad (22)$$

### 3.5 Line-of-sight velocities on the tangent line

Motions in a thin shocked shell will be predominantly tangential to the shell surface. In addition, for the particular case of wind–wind bow shocks, the flow in each azimuthal slice can be shown to be independent (Wilkin 2000), which implies that the shell velocity is parallel to  $\hat{t}$ . The projected line-of-sight shell velocity is therefore

$$573 \quad v_{\text{los}} = (\hat{t}' \cdot -\hat{z}') v_{\parallel}(\theta) = \frac{v_{\parallel}(\theta)(1 + \omega^2)^{1/2} \sin i}{\sin \theta - \omega \cos \theta}, \quad (23)$$

where  $v_{\parallel}(\theta)$  is the gas velocity along the shell and the standard sign convention has been adopted such that velocities away from the observer are deemed positive.

## 4 QUADRICS OF REVOLUTION

For an arbitrary surface of revolution, application of equations (15) and (16) to determine the projected shape of the tangent line is not straightforward and in general requires numerical techniques. However, analytical results can be found for the important class of surfaces known as *quadrics of revolution* (Goldman 1983; Gfrerrer & Zsombor-Murray 2009), which are formed by rotating a conic section plane curve about its symmetry axis. Examples are the sphere, spheroids (oblate and prolate), and right circular paraboloids and hyperboloids.<sup>2</sup> We ignore the degenerate cases of cylinders, cones, and pairs of parallel planes. While mathematically simple, these quadrics are sufficiently flexible that they can provide a useful approximation to more complex bow shock shapes.

The shape of the quadric curves in the  $xy$  plane ( $\phi = 0$ ) is shown in Figs 7(a) and (b) for the ellipse and hyperbola case, respectively. The conic section itself is fully described by two lengths,  $a$  and  $b$ , which are the semi-axes.<sup>3</sup> However, the curve can be translated along the  $x$ -axis to an arbitrary point with respect to the star, so that the apex distance  $R_0$  has no necessary relation to  $a$  or  $b$ , and therefore the star/bow combination requires *three* independent lengths for its specification. The displacement  $x_0$  from the star to the ‘centre’ of the conic section is

$$603 \quad x_0 = R_0 - \sigma a \quad \text{with} \quad \sigma = \begin{cases} +1 & \text{ellipse} \\ -1 & \text{hyperbola} \end{cases}. \quad (24)$$

For hyperbolae, the centre is ‘outside’ the bow and  $x_0$  is always positive, whereas for ellipses the centre is ‘inside’ the bow and  $x_0$  is usually negative, except when  $a < R_0$  (see Fig. 7).

A general parametric form<sup>4</sup> for the  $xy$  coordinates of the quadrics (in the  $\phi = 0$  plane, and with the star at the origin) Q10

<sup>2</sup> We consider only the case of a single sheet of a two-sheet hyperboloid or paraboloid, since these are the versions that resemble a bow, whereas the one-sheet versions resemble the waist of an hourglass.

<sup>3</sup> Note that we do not require that  $a > b$ , so either  $a$  or  $b$  may be the semi-major axis.

<sup>4</sup> The special case of the parabola needs to be treated differently, see Appendix C.

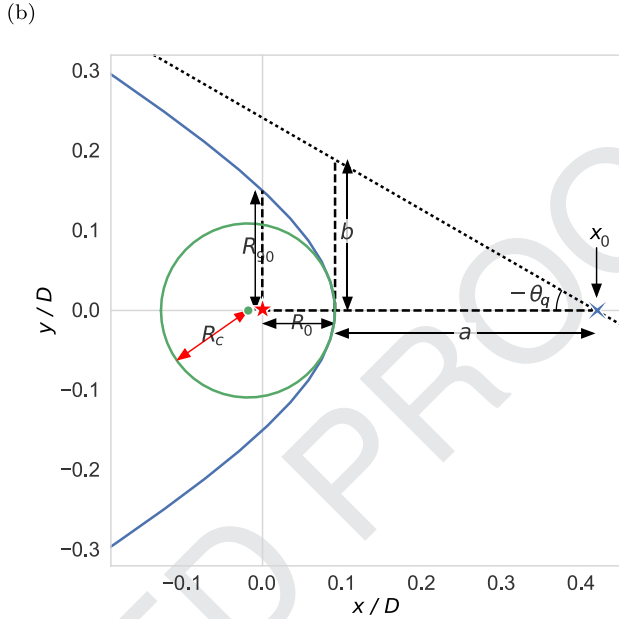
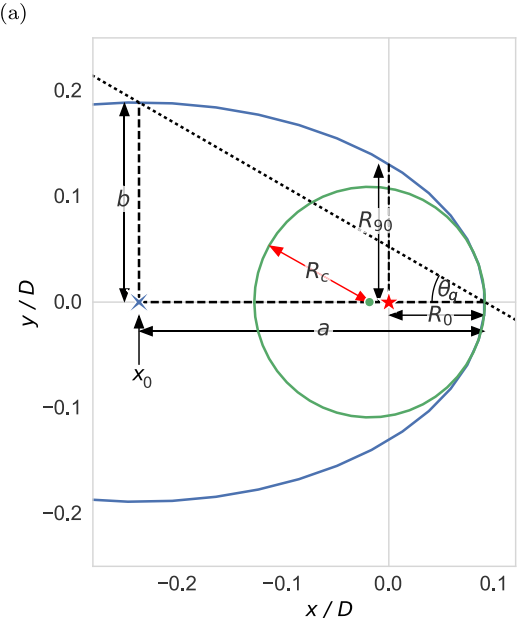


**Figure 7.** Example off-centre conic sections that can form quadrics of revolution: (a) ellipse, (b) hyperbola. The relationship is shown between the conic section parameters  $a$ ,  $b$ ,  $\theta_Q$  and the bow shock characteristic radii  $R_0$ ,  $R_{90}$ ,  $R_c$ , as defined in Fig. 4. The origin (centre of the weaker flow) is indicated by a red star, the centre of curvature of the apex of the bow shock is indicated by a green dot, and the geometric centre of the conic section is indicated by a blue cross, which is offset by  $x_0$  from the origin. Note that  $R_0$ ,  $R_{90}$ ,  $R_c$ ,  $a$ , and  $b$  are all lengths and are always positive, whereas  $x_0$  is a displacement and may be positive or negative.

as a function of  $t = [0, \pi]$  is then

$$\begin{aligned} x &= x_0 + \sigma a \mathcal{C}(t) \\ y &= b \mathcal{S}(t), \end{aligned} \quad (25)$$

where

$$\mathcal{S}, \mathcal{C} = \begin{cases} \sin, \cos & \text{ellipse} \\ \sinh, \cosh & \text{hyperbola} \end{cases}. \quad (26)$$

Except for the circle case ( $\sigma = +1$ ,  $a = b$ ), the parametric variable  $t$  is not actually an angle in physical space. Instead, the polar form of the bow shape  $R(\theta)$  must be found by substituting equations (25) into  $\theta = \tan^{-1} y/x$  and  $R = (x^2 + y^2)^{1/2}$ .

The type of quadric surface can be characterized by the *quadric parameter*:

$$\mathcal{Q} \equiv \sigma \frac{b^2}{a^2}, \quad (27)$$

where  $\mathcal{Q} < 0$  corresponds to open surfaces (hyperboloids) and  $\mathcal{Q} > 0$  corresponds to closed surfaces (oblate spheroids with  $\mathcal{Q} > 1$  and prolate spheroids with  $\mathcal{Q} < 1$ ). Special cases are the sphere ( $\mathcal{Q} = 1$ ) and the paraboloid ( $\mathcal{Q} = 0$ ). Alternatively, one can define a *quadric angle*:

$$\theta_Q = \sigma \tan^{-1}(b/a), \quad (28)$$

which is marked in Fig. 7. In the case of hyperboloids, the asymptotic opening angle of the wings (Section 2 and Fig. 4) is  $\theta_\infty = \pi + \theta_Q$  (note that  $\theta_Q < 0$  in this case), and the minimum slope angle is  $\alpha_{\min} = |\theta_Q|$ , see discussion following equation (18).

The set of parameters  $(\mathcal{Q}, a, x_0)$  are then sufficient to characterize the star/bow combination, where  $a$  is the quadric scale and  $x_0$  is its centre displacement from the star. However, we can also characterize the star/bow by  $(R_0, \Pi, \Lambda)$ , where  $R_0$  is the star-apex distance, and  $\Pi$  and  $\Lambda$  are the planitude and alatitude, see Section 2. We now

derive the equivalences between these two descriptions. The apex radius of curvature for a conic section is

$$R_c = \frac{b^2}{a} = a|\mathcal{Q}|, \quad (29)$$

whereas the perpendicular radius,  $R_{90}$ , is the value of  $y$  when  $x = 0$ , which can be found from equations (24) and (25) as

$$R_{90}^2 = \mathcal{Q} (a^2 - x_0^2). \quad (30)$$

Combining equations (5), (6), (24), and (27)–(30) yields

$$R_0 = x_0 + \sigma a \quad (31)$$

$$\Pi = \frac{a\mathcal{Q}}{a + \sigma x_0} \quad (32)$$

$$\Lambda = \left( \mathcal{Q} \frac{a - \sigma x_0}{a + \sigma x_0} \right)^{1/2} \quad (33)$$

with  $\sigma = \text{sgn } \mathcal{Q}$ . It also follows that the quadric parameter in terms of the planitude and alatitude is

$$\mathcal{Q} = 2\Pi - \Lambda^2. \quad (34)$$

Hence, it is the sign of  $2\Pi - \Lambda^2$  that determines  $\sigma$  and whether a quadric is a spheroid or a hyperboloid. For example, for a constant planitude,  $\Pi$ , we can have a family of different quadric types, with varying alatitude,  $\Lambda$ , that increases from oblate, through prolate and paraboloid, to hyperboloid, as illustrated in Fig. 8.

#### 4.1 Parabolic departure function

The special case of confocal conic sections ( $\Lambda = \Pi$ ) can be written in polar form as

$$R(\theta) = R_0 \frac{1 + e}{1 + e \cos \theta}, \quad (35)$$

754

759

764

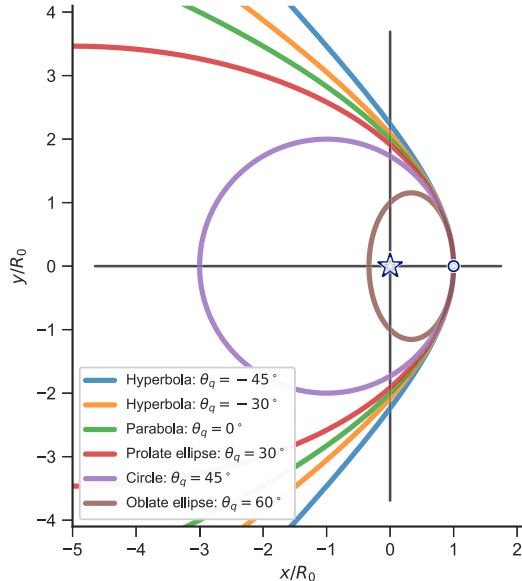


**Figure 8.** Example of a family of conic sections, all with the same planitude (flatness at apex, marked by white dot):  $\Pi = R_c/R_0 = 2$ . The quadric angle,  $\theta_Q$ , varies over the family (see the text), with lower values of  $\theta_Q$  giving larger values of the alatitude,  $\Lambda = R_{90}/R_0$ , meaning more open wings. Different values of  $\Pi$  can be achieved for the exact same quadrics by sliding them along the  $x$ -axis, which will also change the axis scales since these are normalized by  $R_0$ .

where  $e = (1 - \mathcal{Q})^{1/2}$  is the *conic eccentricity*. For the confocal parabola ( $e = 1$ ), the dimensionless reciprocal radius is therefore  $R_0/R(\theta) = \frac{1}{2}(1 + \cos\theta)$ , which suggests the following form for a *departure function* that measures the difference between a given shape  $R(\theta)$  and the parabola:

$$\Delta(\cos\theta) = \frac{R_0}{R(\theta)} - \frac{1}{2}(1 + \cos\theta). \quad (36)$$

From equations (35) and (36), it is clear that  $\Delta$  is a linear function of  $\cos\theta$  for other confocal conics, being positive for ellipses ( $e < 1$ ) and negative for hyperbolae ( $e > 1$ ). Examples are shown in Fig. 9 for a grid of nine conics centred on the confocal parabola, with  $(\Pi, \Lambda)$  ranging from  $3/4$  to  $4/3$  of  $(2, 2)$ . The hyperbolae have negative values of  $\Delta$  in the far wings, with tracks that end at  $\cos\theta_\infty$ .

Strictly speaking, the departure function is redundant if one is interested in only conic sections, since they are fully determined by  $\Pi$  and  $\Lambda$ . None the less, as we will show in following sections, it is a useful tool for studying general  $R(\theta)$ , being very sensitive to small variations in the shape.

#### 4.2 Plane-of-sky projection of quadric surfaces

794

We now apply the machinery of Section 3 to find the projected shape of a quadric bow on the plane of the sky. The intrinsic 3D shape of the shell is given by rotating equations (25) about the  $x$ -axis, but it is more convenient to first transform to a reference frame where the origin is at the centre of the conic section:

$$(X, Y, Z) = (x - x_0, y, z). \quad (37)$$

In this new frame, the quadric shape is

$$X = a\mathcal{C}(t)$$

$$Y = b\mathcal{S}(t)\cos\phi$$

$$Z = b\mathcal{S}(t)\sin\phi. \quad (38)$$

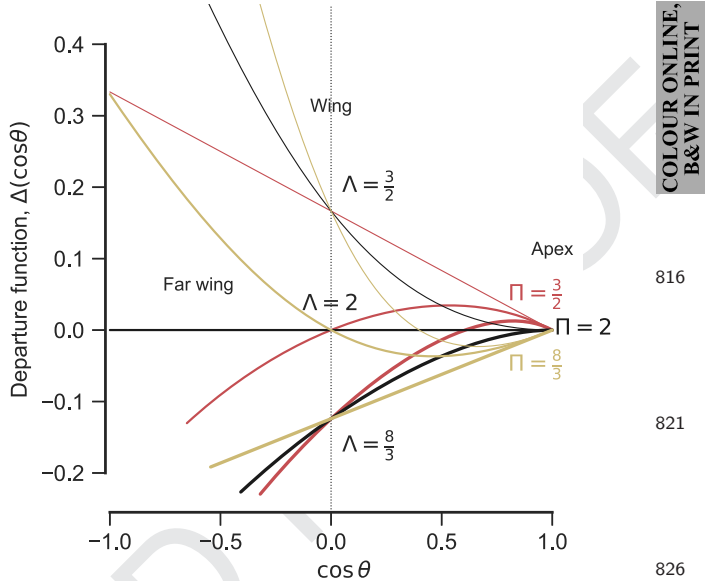


**Figure 9.** Parabolic departure function,  $\Delta(\cos\theta)$ , for conic sections with different planitude and alatitude, centred on that of the confocal parabola,  $(\Pi, \Lambda) = (2, 2)$ , which has  $\Delta(\cos\theta) = 0$ . Planitude (shown by different line colours) determines the slope of  $\Delta$  at the apex,  $\cos\theta = 1$ . Alatitude (shown by different line widths) determines the value of  $\Delta$  at  $\cos\theta = 0$ . All conics with  $\Pi = \Lambda$  have departure functions that are straight lines.

The azimuth of the tangent line as a function of inclination and parametric variable is then found from equations (10) and (15) to be

$$\sin\phi_T = \frac{b\mathcal{C}(t)}{a\mathcal{S}(t)} \tan i. \quad (39)$$

Combining equations (8), (38) and (39) gives the observer-frame Cartesian plane-of-sky coordinates of the tangent line:

$$X'_T = \frac{\mathcal{C}(t)}{a\cos i} (a^2 \cos^2 i + \sigma b^2 \sin^2 i) \\ Y'_T = b\mathcal{S}(t) \left( 1 - \frac{b^2 \mathcal{C}^2(t)}{a^2 \mathcal{S}^2(t)} \tan^2 i \right)^{1/2}. \quad (40)$$

We wish to show that this projected shape is a conic section of the same variety (ellipse or hyperbola) as the one that generated the original quadric. If this were true, then it would be possible to write the plane-of-sky coordinates as

$$X'_T = a'\mathcal{C}(t') \quad (41)$$

$$Y'_T = b'\mathcal{S}(t').$$

Comparing equations (40) and (41), we find after some algebra that the two forms for  $(X'_T, Y'_T)$  are indeed consistent, with the equivalences:

$$a' = af_{Q,i} \cos i \quad (42)$$

$$b' = b \quad (43)$$

$$t' = \mathcal{C}^{-1}[f_{Q,i}\mathcal{C}(t)], \quad (44)$$

where for convenience we define the quadric projection factor:

$$f_{Q,i} = (1 + \mathcal{Q} \tan^2 i)^{1/2}. \quad (45)$$

This demonstrates the original claim that the projected shape is also a conic section, which means that we can reuse the previous equations (31)–(34) with primed quantities substituted for unprimed

816

821

831

836

841

846

851

856

861

866

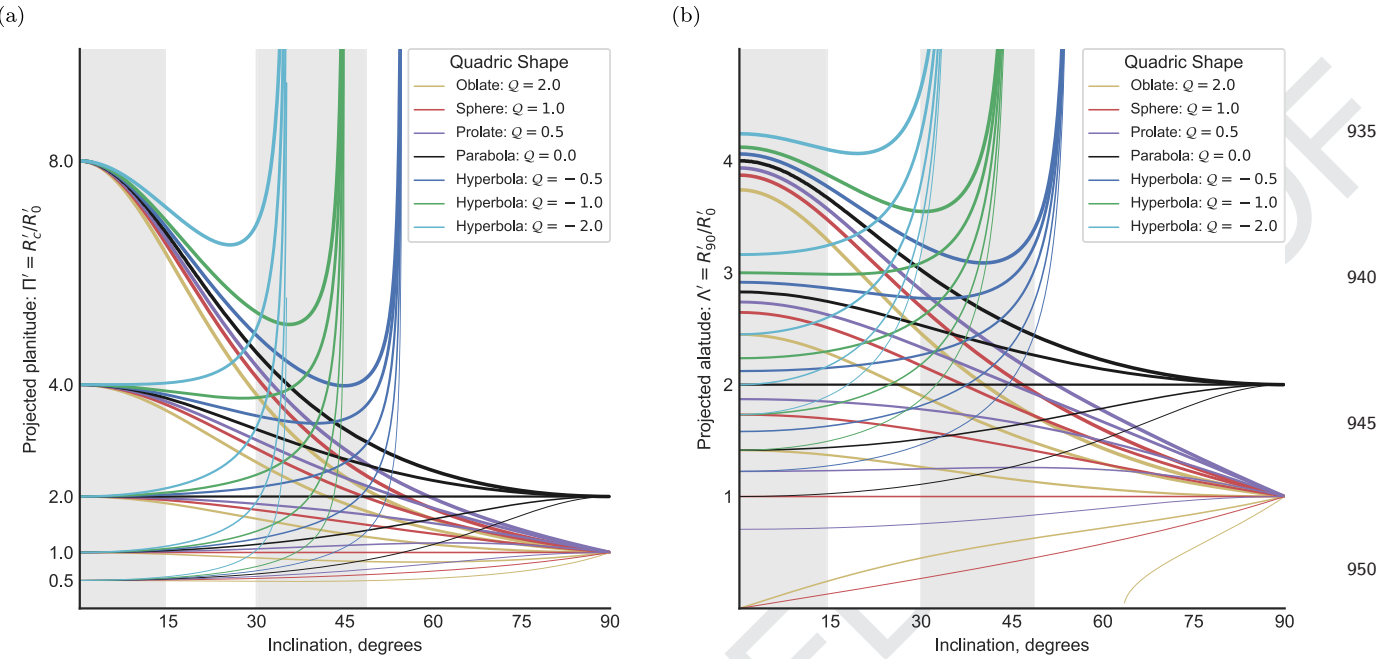


**Figure 10.** Effects of projection on quadrics of revolution: variation with inclination,  $|i|$ , of bow size and shape. Different line colours correspond to varying quadric parameter,  $Q$  (see key), while variation in line width corresponds to variation in the ‘true’ planitude,  $\Pi$ , or apex radius of curvature. Vertical grey rectangles show quartiles of  $|\sin i|$ , which will be equally populated for an isotropic distribution of orientations. (a) Projected planitude:  $\Pi'$ . (b) Projected alatitude,  $\Lambda'$ .

ones. From equations (27), (42), and (43), it follows that the quadric parameter of the projected shape is

$$Q' = \frac{Q}{f_{Q,i}^2 \cos^2 i}. \quad (46)$$

Finally, we transform the projected reference frame back to be centred on the star again:

$$(x'_T, y'_T) = (X'_T + x'_0, Y'_T), \quad (47)$$

where the projected quadric displacement  $x'_0$  follows from simple foreshortening:

$$x'_0 = x_0 \cos i. \quad (48)$$

The projection of the apex distance then follows from the primed version of equation (31) as

$$\frac{R'_0}{R_0} = \cos i \left[ 1 + \frac{\Pi}{Q} (f_{Q,i} - 1) \right], \quad (49)$$

and the projected planitude and alatitude can be calculated from equations (32), (34), (42), and (46) as

$$\Pi' = \frac{\Pi}{(R'_0/R_0) f_{Q,i} \cos i} \quad (50)$$

$$\Lambda' = (2\Pi' - Q')^{1/2}. \quad (51)$$

These are all shown in Figs 10 and 11 for a variety of quadric parameter  $Q$  (line colour) and true planitude  $\Pi$  (line thickness). The projected planitude and alatitude (Fig. 10) behave in a qualitatively similar fashion. Whatever the true values of  $\Pi$  and  $\Lambda$ , all spheroids ( $Q > 0$ ) tend towards  $\Pi' = 1$  and  $\Lambda' = 1$  as the inclination increases towards  $90^\circ$ . This is because when the spheroid is oriented edge-on, we see its circular cross-section. Hyperboloids behave differently: although  $\Pi'$  and  $\Lambda'$  initially decrease with increasing inclination (for true  $\Pi > 2$ ), they turn around and increase again

as  $|i|$  approaches the critical value  $i_{\text{crit}} = 90^\circ - |\theta_Q|$ . For  $|i| > i_{\text{crit}}$ , the tangent line does not exist (see Section 3.3) because the line of sight is ‘inside’ the asymptotic cone of the far wings (with opening half-angle  $\alpha_{\min} = |\theta_Q|$ ), and so no limb-brightened shell would be visible.<sup>5</sup> For paraboloids and spheroids,  $\alpha_{\min} = 0$ , which means that the tangent line exists for all viewing angles.

In Fig. 11(a), we show the inclination-dependent tracks of the quadrics in the diagnostic  $\Pi' - \Lambda'$  plane of projected alatitude versus projected planitude. The true planitude and alatitude, which are seen for an edge-on viewing angle  $i = 0^\circ$ , are marked by filled circles. The zones corresponding to each class of quadric (oblate spheroid, prolate spheroid, or hyperboloid) are marked by grey shading, and it can be seen that the tracks never cross from one zone to another. The convergence of all the spheroid tracks on the point  $(\Pi', \Lambda') = (1, 1)$  is apparent, as is the divergence of the hyperboloid tracks towards  $(\Pi', \Lambda') = (+\infty, +\infty)$ , whereas the paraboloids, by contrast, converge on the point  $(\Pi', \Lambda') = (2, 2)$ . Two special cases are the confocal paraboloid and the concentric sphere,<sup>6</sup> with true planitude and alatitude  $(\Pi, \Lambda) = (2, 2)$  and  $(1, 1)$ , respectively, which are the only quadrics whose apparent shape remains identical for all inclination angles.

Fig. 11(b) shows how the apparent star–apex separation varies with inclination. For moderate inclinations,  $|i| < 30^\circ$ , this depends primarily on the true planitude  $\Pi$ , with very little influence of the quadric parameter  $Q$ . For  $\Pi > 1$ , the separation increases with  $|i|$ ,

<sup>5</sup> As illustrated in fig. 8 of Graham et al. (2002), the isophotal emission contours are elliptical in such a case (assuming cylindrical symmetry) and no curved bow shape is apparent. Deviations from cylindrical symmetry can result in a curved emission arc, even for this no-tangent case (Graham et al.’s fig. 9), but that is beyond the scope of this paper.

<sup>6</sup> So named because the star is at the focus of the parabola, or the centre of the sphere.

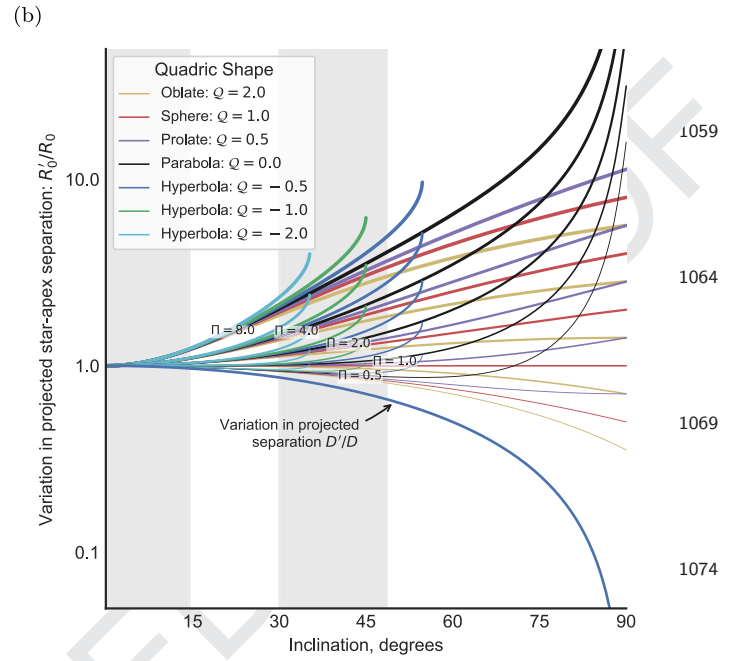
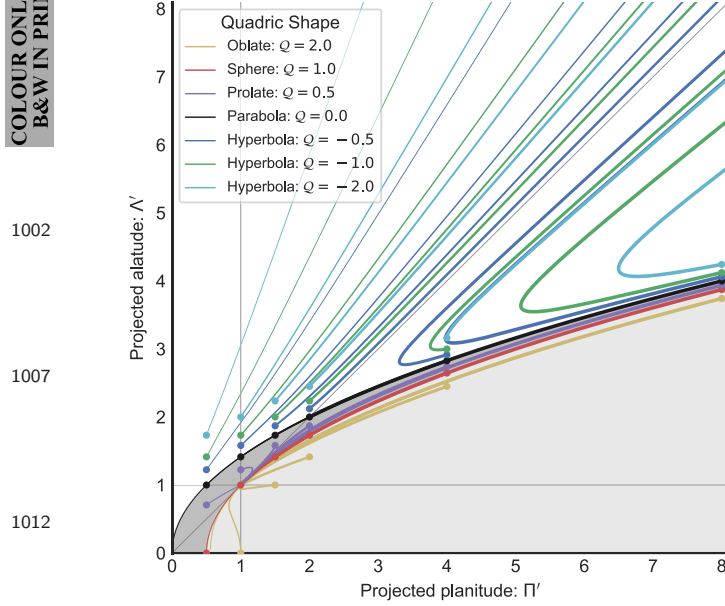


**Figure 11.** As Fig. 10, but (a) diagnostic planitude–alatitude diagram:  $\Lambda'$  versus  $\Pi'$ , and (b) projected/true star–apex distance:  $R'_0/R_0$  versus  $|i|$ . In panel (a), shading indicates different classes of quadrics: hyperboloids (white), prolate spheroids (dark grey), and oblate spheroids (light grey), with the limiting case of paraboloids shown by the thin black line.

whereas for  $\Pi < 1$ , it decreases slightly. Note, however, that for the cases where the projected distance to the source of the external flow,  $D'$ , can be measured, then  $R'_0/D'$  is always an increasing function of  $|i|$ . For larger inclinations,  $|i| > 30^\circ$ , the strands for different  $Q$  begin to separate, with hyperbolae showing the strongest increase of  $R'_0$  with  $|i|$ .

A complementary view of the effects of projection is shown in Fig. 12, which shows ‘snapshots’ of  $(\Pi', \Lambda')$  for a sequence of six values of the inclination, equally spaced in  $|\sin i|$ , so that each panel is equally likely for an isotropic distribution of orientations. The distributions of the true  $\Pi$  and  $\Lambda$  are each assumed to be uniform in the range  $[0.5, 4.5]$ , giving a uniformly filled square of values for  $|i| = 0$ , which becomes increasingly distorted as  $|i|$  increases. The colour scale represents  $Q$  and the symbol size is proportional to  $R'_0/R_0$ . It can be seen that the points tend to cluster closer and closer to the diagonal,  $\Lambda' = \Pi'$ , as the inclination increases, and that the points just below this line tend to have the largest values of  $R'_0/R_0$ . The green shaded region shows the zone of true  $\Lambda$ ,  $\Pi$  for hyperboloids where the tangent lines still exist for that value of  $|i|$ . This becomes smaller and smaller as  $|i|$  increases, which explains why the hyperboloid zone becomes increasingly depopulated: all quadrics that lie above this region when  $i = 0^\circ$  will no longer be visible as a bow for this value of  $|i|$ . Note that this figure is merely illustrative of the qualitative effects of projection, since in reality there is no particular reason to expect a uniform distribution in true  $\Pi$  and  $\Lambda$ .

## 5 THIN-SHELL BOW SHOCK MODELS

More physically realistic examples of bow shapes are provided by steady-state hydrodynamic models for the interaction of hypersonic flows in the thin-shell limit. The classic examples are the solutions for the wind–parallel stream and wind–wind problems (see Section 1) of Canto et al. (1996, hereafter CRW), where it is assumed that the two shocks are highly radiative and that the post-shock flows

are perfectly mixed to form a single shell of negligible thickness. In this approximation, the shape of the shell is found algebraically by CRW from conservation of linear and angular momentum, following an approach first outlined in Wilkin (1996). For the wind–stream case, the resulting bow shape was dubbed *wilkinoid* by Cox et al. (2012) and has the form

$$R(\theta) = R_0 \csc \theta (3(1 - \theta \cot \theta))^{1/2}. \quad (52)$$

For the wind–wind case, a family of solutions are found that depend on the value of  $\beta$ , the wind momentum ratio,<sup>7</sup> see Fig. 3, equations (1) and (2), and surrounding discussion in Section 1. We propose that these shapes be called *cantoids*. The exact solution for the cantoid shapes (equations 23 and 24 of CRW) is only obtainable in implicit form, but an approximate explicit solution (equation 26 of CRW) is very accurate for  $\beta \leq 0.1$ . The wilkinoid shape corresponds to the  $\beta \rightarrow 0$  limit of the cantoids. Note that CRW employ cylindrical polar coordinates,  $z$  and  $r$ , see our Fig. 3, and we follow this usage for the thin-shell models discussed in this section. CRW’s  $z$ -axis corresponds to the Cartesian  $x$ -axis used in Sections 3 and 4 of the current paper, while the  $r$ -axis corresponds to  $y$  when  $\phi = 0$ .

A generalization of the cantoids to the case of an anisotropic<sup>8</sup> inner wind is developed next, giving rise to what we call *ancantoids*, which depend on an anisotropy index,  $k$ , in addition to  $\beta$ .

### 5.1 Bow shocks from anisotropic wind–wind interactions

We wish to generalize the results of CRW to the case where the inner wind is no longer isotropic, but instead has a density that falls

<sup>7</sup> By always placing the weaker of the two winds at the origin, it is only necessary to consider  $\beta \leq 1$ .

<sup>8</sup> Note that the wind anisotropy axis must be aligned with the star–star axis to maintain cylindrical symmetry.

1126

1131

1136

1141

1146

1151

1156

1161

1166

1171

1176

1183

1188

1193

1198

1203

1208

1213

1

1223

1228

1233

1238

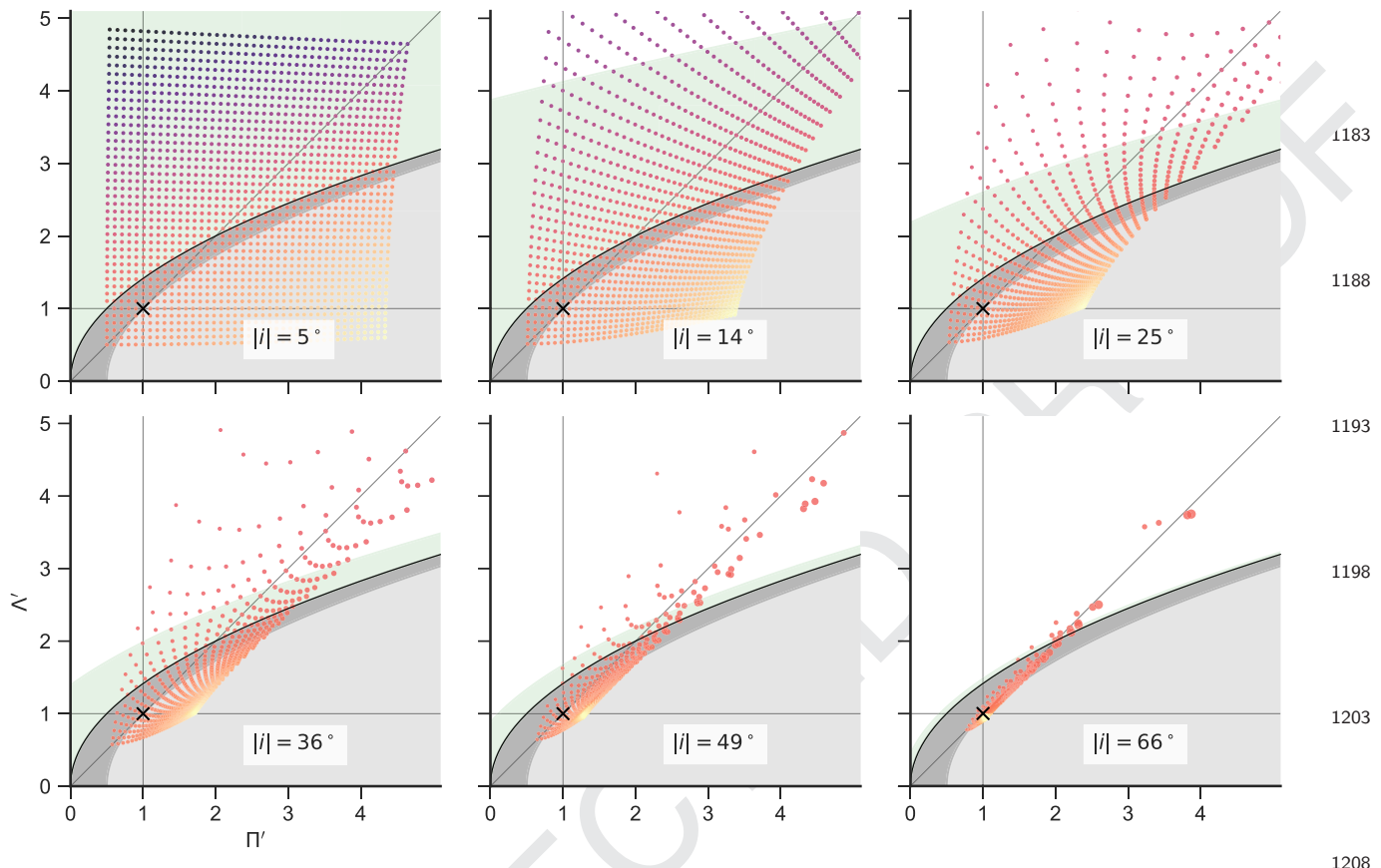


**Figure 12.** Variation with inclination angle of the apparent shape of quadric bows with true planitude and alatitude that are uniformly distributed over the ranges  $\Pi = [0.5, 4.5]$ ,  $\Lambda = [0.5, 4.5]$ . Panels show the apparent  $(\Pi', \Lambda')$  as the inclination is increased through uniform intervals in  $|\sin i|$ . Symbol colour represents the quadric parameter,  $\mathcal{Q}$ , increasing from dark blue, through orange, to yellow. Symbol size is proportional to the increase in apparent star–apex distance,  $R'_0/R_0$ .

off with angle,  $\theta$ , away from the symmetry axis. Specifically, at some fiducial spherical radius,  $R_0$ , from the origin, the wind mass density is given by

$$\rho(R_0, \theta) = \begin{cases} \rho_0 \cos^k \theta & \text{for } \theta \leq 90^\circ \\ 0 & \text{for } \theta > 90^\circ \end{cases}, \quad (53)$$

where  $\rho_0$  is the density on the symmetry axis and  $k \geq 0$  is an *anisotropy index*. The wind velocity is still assumed to be constant and the wind streamlines to be radial, so the radial variation of density at each angle is  $\rho(R, \theta) = \rho(R_0, \theta)(R/R_0)^{-2}$  and the wind mass-loss rate and momentum loss rate per solid angle both have the same  $\cos^k \theta$  dependence as the density. Examples are shown in Fig. 13 for a variety of different values of  $k$ . As  $k$  increases, the wind becomes increasingly jet-like.

Our primary motivation for considering such an anisotropic wind is the case of the Orion nebula proplyds and their interaction with the stellar wind of the massive star  $^{12}\text{Ori C}$  (García-Arredondo et al. 2001). The inner ‘wind’ in this case is the transonic photoevaporation flow away from a roughly hemispherical ionization front, where photoionization equilibrium, together with monodirectional illumination of the front, implies that the ionized hydrogen density,  $n$ , satisfies  $n^2 \propto \cos \theta$ , which is equivalent to  $k = 0.5$  in equation (53). Since the primary source of ionizing photons is the same star that is the source of the outer wind, it is natural that the inner wind’s axis should be aligned with the star–star axis in this case. For other potential causes of wind anisotropy (for instance, bipolar flow from an accretion disc), there is no particular reason for the axes to be

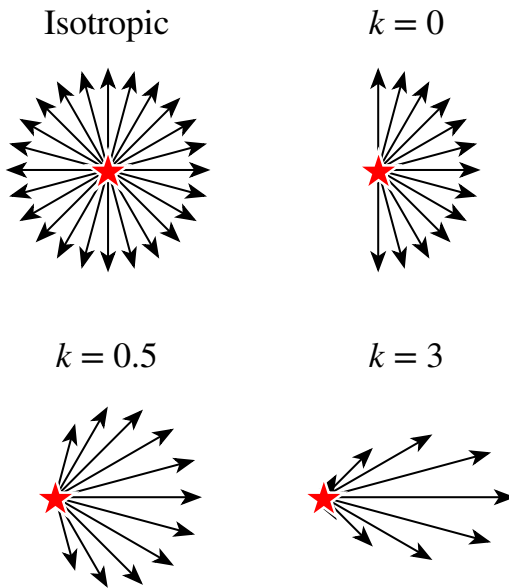


**Figure 13.** Schematic diagram of wind flow patterns in isotropic and non-isotropic cases for different values of the anisotropy index,  $k$ . Arrow length represents the wind momentum loss rate per solid angle.

aligned, so cylindrical symmetry would be broken. Nevertheless, we calculate results for general  $k$  with aligned axes, so as to provide a richer variety of cylindrically symmetric bow shock shapes than are seen in the cantoids.

1245 The general solution for the bow shock shape,  $R(\theta)$ , in the CRW formalism is

$$R(\theta) = \frac{j_w + j_{w1}}{(\dot{\Pi}_{wr} + \dot{\Pi}_{wr1}) \cos \theta - (\dot{\Pi}_{wz} + \dot{\Pi}_{wz1}) \sin \theta}, \quad (54)$$

1250 where  $\dot{\Pi}_{wr}$ ,  $\dot{\Pi}_{wz}$ ,  $j_w$  are the accumulated linear radial momentum, linear axial momentum, and angular momentum, respectively, due to the inner wind emitted between the axis and  $\theta$ . The equivalent quantities for the outer wind have subscripts appended with ‘1’. The inner wind momenta for our anisotropic case (replacing CRW’s equations 9 and 10) are

$$\begin{aligned} \dot{\Pi}_{wz} &= \frac{k+1}{2(k+2)} \dot{M}_w^0 V_w \max[(1 - \cos^{k+2} \theta), 1] \\ \dot{\Pi}_{wr} &= (k+1) \dot{M}_w^0 V_w I_k(\theta), \end{aligned} \quad (55)$$

1260 where

$$\dot{M}_w^0 = \frac{2\pi}{k+1} r_0^2 \rho_0 V_w \quad (56)$$

1265 is the total mass-loss rate of the inner wind. The integral

$$I_k(\theta) = \int_0^{\max(\theta, \pi/2)} \cos^k \theta \sin^2 \theta d\theta \quad (57)$$

1270 has an analytic solution in terms of the hypergeometric function,  ${}_2F_1(-\frac{1}{2}; \frac{1+k}{2}; \frac{3+k}{2}; \cos^2 \theta)$ , but is more straightforwardly calculated by numerical quadrature. The angular momentum of the inner wind about the origin is  $j_w = 0$  because it is purely radial. The outer wind momenta are unchanged from the CRW case, but are given here for completeness:

$$\begin{aligned} \dot{\Pi}_{wz1} &= -\frac{\dot{M}_{w1}^0 V_{w1}}{4} \sin^2 \theta_1 \\ \dot{\Pi}_{wr1} &= \frac{\dot{M}_{w1}^0 V_{w1}}{4} (\theta_1 - \sin \theta_1 \cos \theta_1) \\ \dot{J}_{w1} &= \frac{\dot{M}_{w1}^0 V_{w1}}{4} (\theta_1 - \sin \theta_1 \cos \theta_1) D. \end{aligned} \quad (58)$$

We define  $\beta$  in this case as the momentum ratio *on the symmetry axis*, which means that

$$1285 \dot{M}_{w1}^0 V_{w1} = 2(k+1)\beta \dot{M}_w^0 V_w. \quad (59)$$

Substituting equations (55)–(59) into equation (54) and making use of the geometric relation between the interior angles of the triangle shown in Fig. 3:

$$1290 R \sin(\theta + \theta_1) = D \sin \theta_1, \quad (60)$$

yields

$$1295 \theta_1 \cot \theta_1 = 1 + 2\beta \left( I_k(\theta) \cot \theta - \frac{1 - \cos^{k+2} \theta}{k+2} \right), \quad (61)$$

which is the generalization of CRW’s equation 24 to the anisotropic case. Equation (61) is solved numerically to give  $\theta_1(\theta)$ , which is then combined with equations (60) and (1) to give the dimensionless bow shape,  $R(\theta; \beta, k)/R_0$ , where we now explicitly indicate the dependence of the solution on two parameters: axial momentum ratio,  $\beta$ , and anisotropy index,  $k$ . We refer to the resultant bow shapes as *ancantoids*.

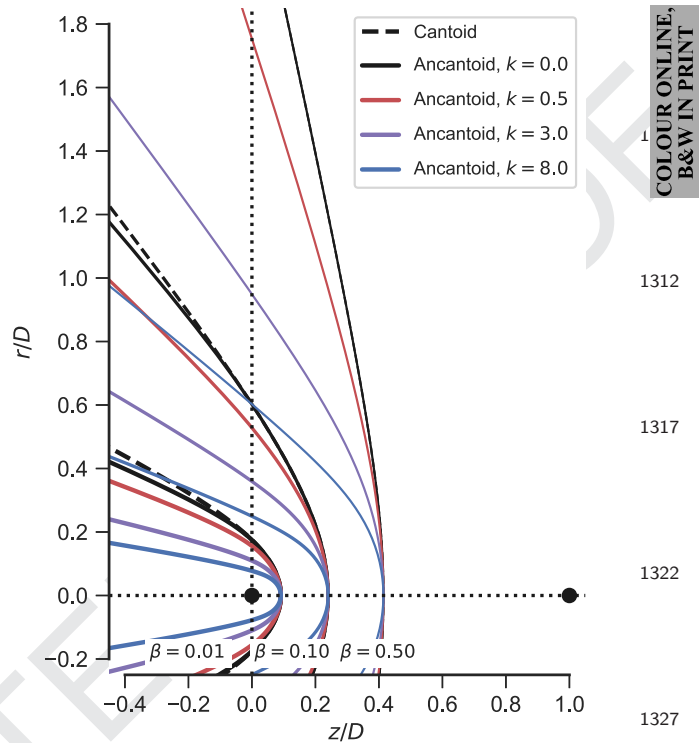


**Figure 14.** Bow shock shapes for interacting winds in the thin-shell approximation: cantoids and ancantoids. Coordinates are normalized by  $D$ , the distance between the two wind sources, which are indicated by black dots on the axis. The weaker source is at  $(0.0, 0.0)$  and the stronger source is at  $(1.0, 0.0)$ . Results are shown for different values of the wind momentum ratio,  $\beta$  (different line widths), and for the case where the weaker wind is isotropic (black lines) or anisotropic (coloured lines).

## 5.2 True shapes of cantoids and ancantoids

The shapes of the ancantoid bow shocks are shown in Fig. 14 for three different values of  $\beta$ , and are compared with the CRW results for cantoids (dashed curves). The location of these shapes in the planitude–alatitude plane is shown in Fig. 15, where the grey background shading indicates the zones of different quadric classes, as in Section 4, Figs 11 and 12. Values of  $\Pi$  and  $\Lambda$  are calculated via the analytic expressions derived in Appendices D1 and D2, respectively, which are only approximate in the case of  $\Lambda$ . However, the filled square symbols show the exact results for  $\beta = 0.5$ , which can be seen to lie extremely close to the approximate results, even for the worst case of  $k = 0$ . The leading term in the relative error of equation (D14) scales as  $(\beta/(k+2))^2$ , so the approximation is even better for smaller  $\beta$  and larger  $k$ .

It is apparent from Fig. 14 that the  $k = 0$  ancantoid is identical to the cantoid for  $\theta \leq 90^\circ$  ( $z > 0$ , to the right of vertical dotted line in Fig. 14), but is slightly more swept back in the far wings.<sup>9</sup> Since the true planitude and alatitude depend on  $R(\theta)$  only in the range  $\theta = [0, 90^\circ]$ , the cantoid and the  $k = 0$  ancantoid behave identically in Fig. 15. There is a general tendency for the bows to be flatter and more open with increasing  $\beta$  and decreasing  $k$ , with the cantoid being most open at a given  $\beta$ . All the models cluster close to the diagonal  $\Lambda \simeq \Pi$  in the planitude–alatitude plane, but with a tendency for  $\Lambda > \Pi$  at higher anisotropy. There is therefore a degeneracy

<sup>9</sup> Due to the discontinuity in the inner wind density at  $\theta = 90^\circ$  (see Fig. 13), there is a discontinuity in the second derivative of the bow shape.

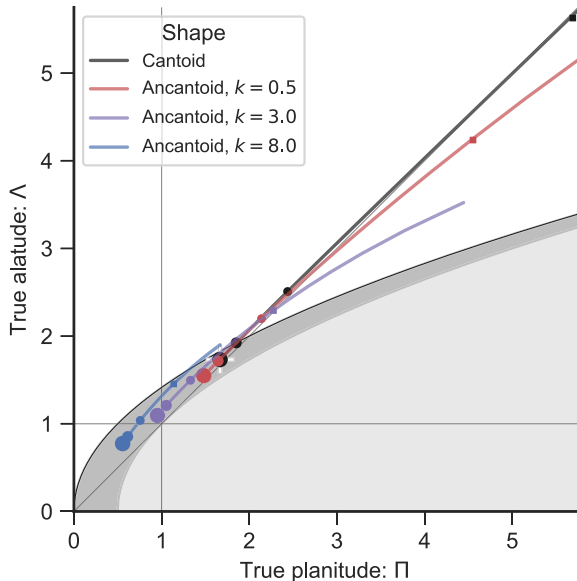


**Figure 15.** True shapes of cantoids and ancantoids in the  $\Pi-\Lambda$  plane, calculated according to results of Appendix D. For each line,  $\beta$  varies over the range  $[0, 1]$  from lower left to upper right (although the black and red lines are truncated on the upper right), and line colours correspond to different anisotropy indices, matching those used in Fig. 14. Circle symbols mark particular  $\beta$  values: 0, 0.01, 0.1, from largest to smallest circle. Square symbols mark  $\beta = 0.5$ , but with  $\Lambda$  calculated exactly, instead of using the approximation of equation (D14). The white plus symbol marks the result for the wilkinoid:  $(\Pi, \Lambda) = (\frac{5}{3}, \sqrt{3})$ . Background shading indicates the domains of different quadric classes: hyperboloids (white), prolate spheroids (dark grey), and oblate spheroids (light grey).

between  $\beta$  and  $k$  for higher values of  $\beta$ . The wilkinoid shape, which corresponds to the  $\beta \rightarrow 0$  limit of the cantoids, is marked by a white plus symbol in Fig. 15, and lies in the prolate spheroid region of the plane. Cantoids lie either in the prolate spheroid or hyperboloid regions, according to whether  $\beta$  is less than or greater than about 0.01. For ancantoids of increasing  $k$ , this dividing point moves to higher values of  $\beta$ , until almost the entire range of models with  $k = 8$  are within the prolate spheroid zone.

However, the true planitude and alatitude, which are what would be observed for a side-on viewing angle ( $i = 0$ ), are not at all sensitive to the behaviour of the far wings of the bow shock, which has a rather different implication as to which variety of quadric best approximates each shape. We illustrate this in Fig. 16, which shows two different ways of estimating the quadric angle,  $\theta_Q$  (see Section 4). The first is from  $(\Pi, \Lambda)$ , as in Fig. 15:

$$\theta_Q^{\text{head}} = \text{sgn}(2\Pi - \Lambda^2) \tan^{-1} |2\Pi - \Lambda^2|^{1/2}, \quad (62)$$

which follows from equations (27), (28), and (34). The second is from the asymptotic opening angle of the wings,  $\theta_\infty$  (Fig. 4):

$$\theta_Q^{\text{tail}} = \theta_\infty - 180^\circ, \quad (63)$$

where  $\theta_\infty$  is calculated from equation (D17) for ancantoids or equation (D19) for cantoids. If the bow shock shape were truly a quadric, then these two definitions would agree. However, as seen in Fig. 16, this is not the case for the cantoids and ancantoids. While  $[b]\theta_Q^{\text{head}}$  generally corresponds to a prolate spheroid (except for the largest values of  $\beta$ ),  $[b]\theta_Q^{\text{tail}}$  always corresponds to a hyperbola. This tension between the shape of the head and the shape of the far wings has important implications for the projected shapes (as we will see in the

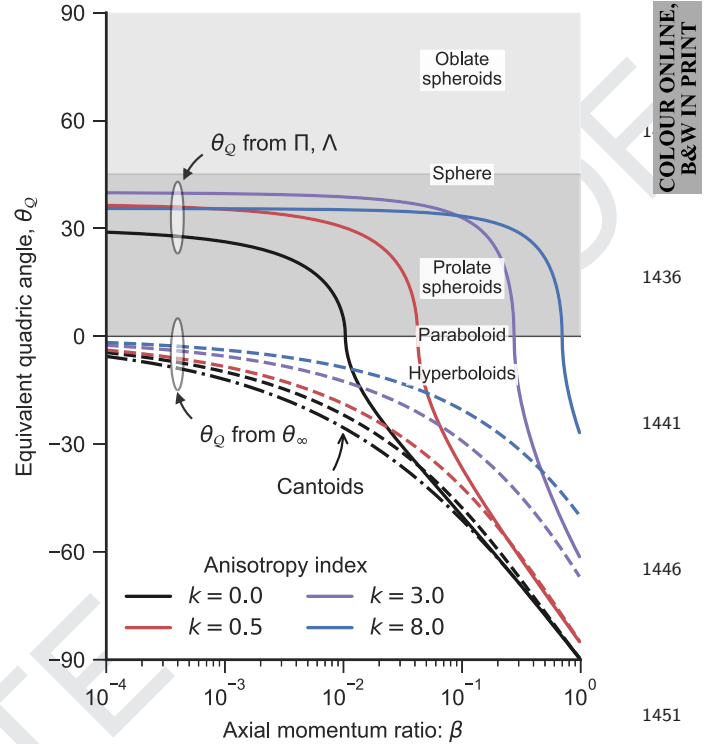


**Figure 16.** Equivalent quadric angles,  $\theta_Q$ , for ancantoids and cantoids. Solid lines show values of  $\theta_Q$  calculated from  $(\Pi, \Lambda)$ , which is representative of the shape of the head, while dashed lines show  $\theta_Q$  calculated from  $\theta_\infty$ , which is representative of the tail. Dot-dashed line shows the result for cantoids, which differ from the  $k = 0$  ancantoids in  $\theta_\infty$ , but not in  $(\Pi, \Lambda)$ . Grey shading and line colours have the same meaning as in Fig. 15.

next section), since the far wings influence the projected planitude and alatitude when the inclination is large.

Fig. 17 shows the parabolic departure function (see Section 4.1) for the thin-shell models. This provides an alternative perspective on the resultant bow shapes, with two different types of behaviour being apparent. Models with high  $\beta$  and low anisotropy behave similarly to the hyperboloids, such as the  $(\Pi, \Lambda) = (\frac{3}{2}, \frac{8}{3}), (2, \frac{8}{3}), (\frac{8}{3}, \frac{8}{3})$ , and  $(\frac{3}{2}, 2)$  cases from Fig. 9. This is the case for the  $\beta \geq 0.01$  models in Fig. 17(a), which all show departure functions that become negative in the far wings (more open than parabola) and terminate at a  $\theta_\infty < 180^\circ$ . The second type of behaviour is shown by models with low  $\beta$  or high anisotropy, which behave like spheroids for positive and mildly negative values of  $\cos \theta$ , but, unlike the spheroids, all tend towards  $\Delta = 0$  in the far tail as  $\cos \theta \rightarrow -1$ .

### 5.3 Apparent shapes of projected cantoids and ancantoids

Figs 18 and 19 show the apparent bow shapes of various thin-shell models (wilkinoid, cantoids, ancantoids)<sup>10</sup> for different inclination angles  $|i|$ . For comparison, Fig. 18(a) shows the confocal paraboloid, whose apparent shape is independent of inclination (see Appendix C). The wilkinoid (Fig. 18b) shows only subtle changes, with the wings becoming slightly more swept back as the inclination increases. The cantoids (Figs 18c and d) behave in the opposite

<sup>10</sup> See also previous studies of the projected shape of the wilkinoid (Wilkin 1997; Cox et al. 2012; Ng et al. 2017) and the cantoids (Roberto et al. 2005).

1498

1503

1508

1513 (b)

1518

1523

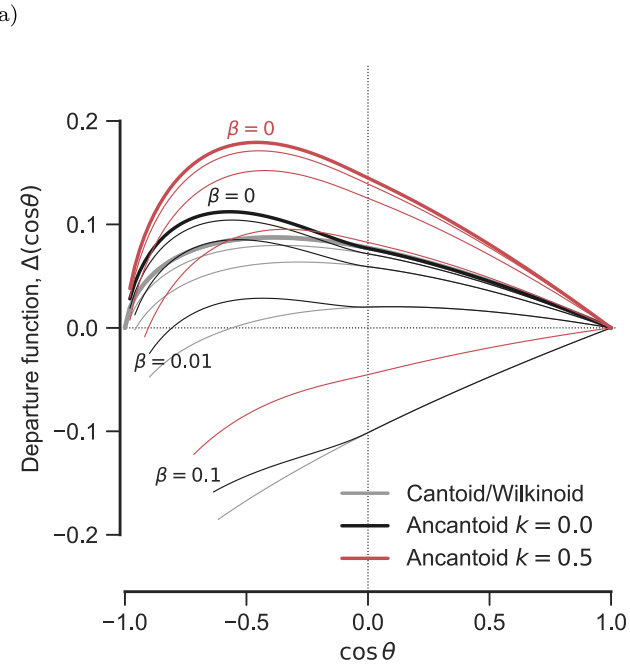
1528

1533

1538

1543

1548



(a)

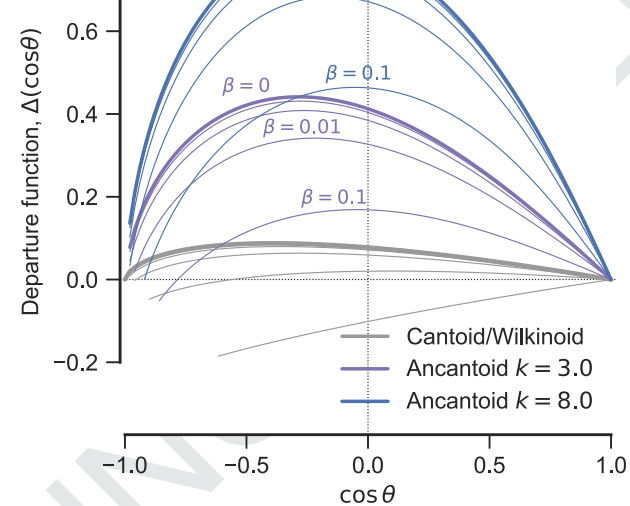


**Figure 17.** Parabolic departure function,  $\Delta(\cos \theta)$ , for ancantoids and cantoids. Heavy lines show the  $\beta = 0$  parallel-stream case (wilkinoid in the isotropic case). Light lines show increasing values of  $\beta = 10^{-4}, 0.001, 0.01, 0.1$ , as marked. (a) Cantoids (grey) and moderately anisotropic ancantoids: hemispheric,  $k = 0$  (black), and proplyd-like,  $k = 0.5$  (red). (b) Cantoids (grey) and extremely anisotropic, jet-like ancantoids:  $k = 3$  (purple) and  $k = 8$  (blue).

way, with the wings becoming markedly more open once  $|i|$  exceeds  $60^\circ$  (for  $\beta = 0.001$ ) or  $45^\circ$  (for  $\beta = 0.01$ ). The ancantoids (Fig. 19) can show more complex behaviour. For instance, in the  $k = 0.5$ ,  $\beta = 0.001$  ancantoid (Fig. 19a), the near wings begin to become more closed with increasing inclination up to  $|i| = 60^\circ$ , at which point they open up again, whereas the opening angle of the far wings increases monotonically with  $|i|$ .

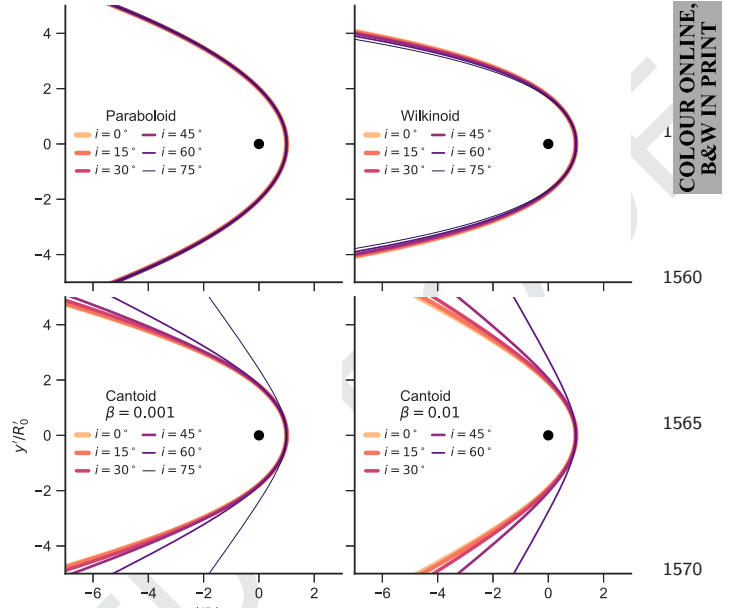


**Figure 18.** Apparent bow shapes as a function of inclination angle for isotropic thin-shell models. (a) Confocal paraboloid for comparison (shape independent of inclination). (b) Wilkinoid. (c) Cantoid,  $\beta = 0.001$ . (d) Cantoid,  $\beta = 0.01$ .

1560

1565

1570

1575

1

1585

1590

1595

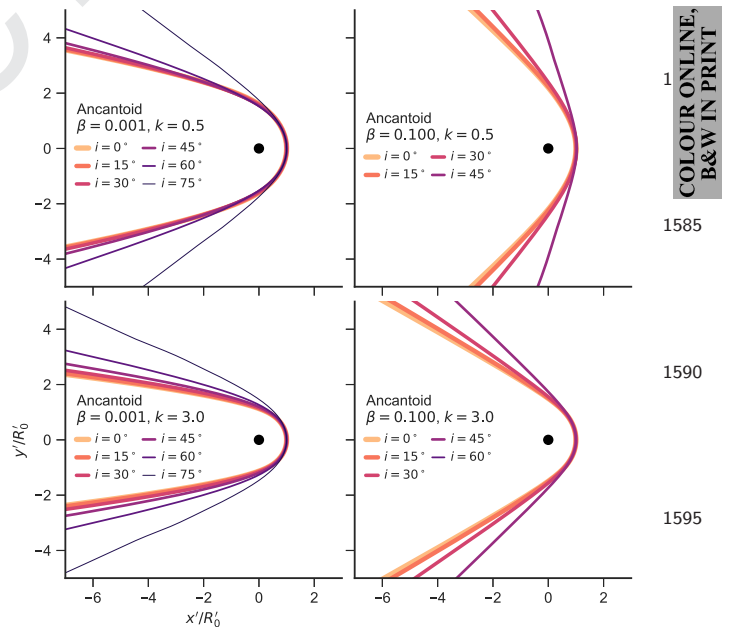


**Figure 19.** Further apparent bow shapes as a function of inclination angle for anisotropic thin-shell models (ancantoids). (a)  $\beta = 0.001, k = 0.5$ ; (b)  $\beta = 0.1, k = 0.5$ ; (c)  $\beta = 0.001, k = 3$ ; (d)  $\beta = 0.1, k = 3$ .

1600

1605

1610

The inclination-dependent tracks that are traced by the thin-shell models in the projected planitude–alatitude plane are shown in Fig. 20. The behaviour is qualitatively different from the quadric shapes shown in Fig. 11(a) in that the tracks are no longer confined within the borders of the region of a single type of quadric (hyperboloid or spheroid). At low inclinations, many of the models behave like the prolate spheroids, but then transition to a hyperboloid behaviour at higher inclinations, which is due to the tension between the shape of the head and the shape of the far wings, as

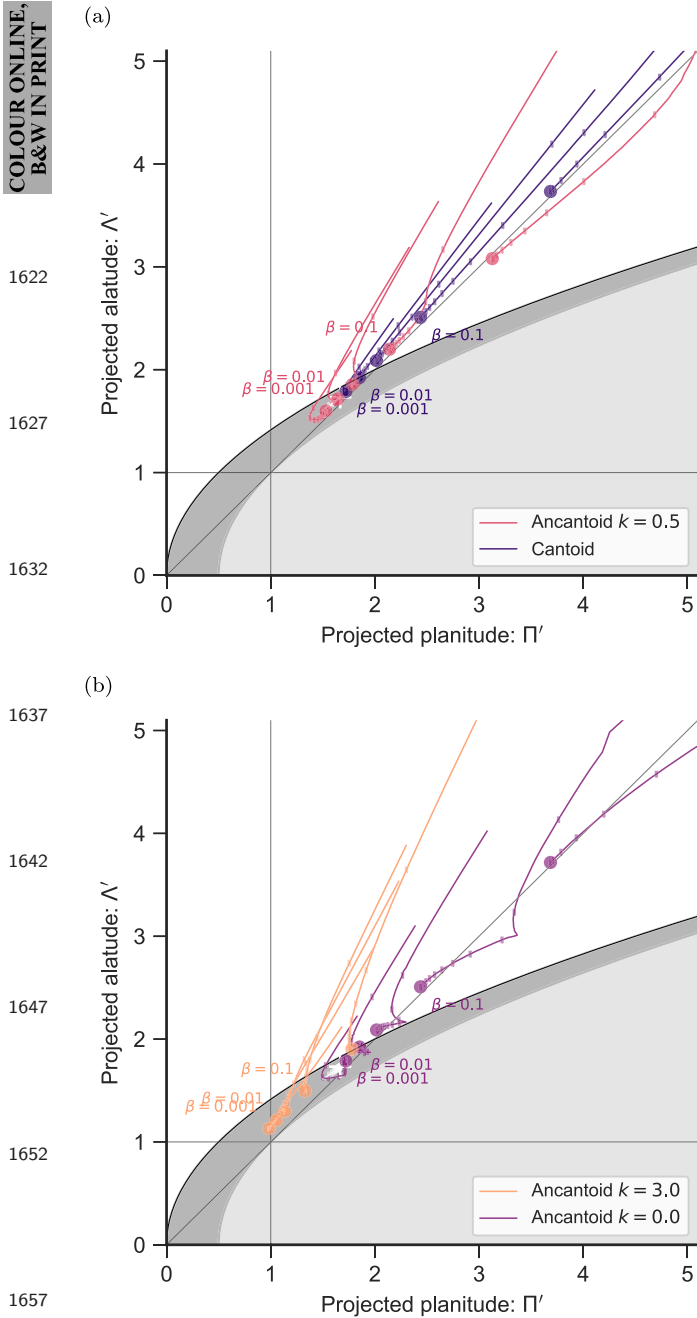


**Figure 20.** Apparent projected shapes of wilkinoid, cantoids, and ancantoids in the  $\Pi' - \Lambda'$  plane. Coloured symbols indicate the  $|i| = 0$  position for  $\beta = 0.001, 0.003, 0.01, 0.03, 0.1, 0.3$ . Thin lines show the inclination-dependent tracks of each model, with tick marks along each track for 20 equally spaced values of  $|\sin i|$ . Grey shaded regions are as in Fig. 11(a). The wilkinoid track is shown in white. (a) Isotropic wind model (cantoid) and proplyd-like model (ancantoid,  $k = 0.5$ ). (b) Hemispheric wind model (ancantoid,  $k = 0$ ) and jet-like model (ancantoid,  $k = 3$ ).

1667

discussed in the previous section. This can be seen most clearly in the  $\beta = 0.001$ ,  $k = 0.5$  ancantoid [lowest red line in Fig. 20(a), see also zoomed version in Fig. 21]. The track begins heading towards  $(\Pi', \Lambda') = (1, 1)$ , as expected for a spheroid, but then turns around and crosses the paraboloid line to head out on a hyperboloid-like track.

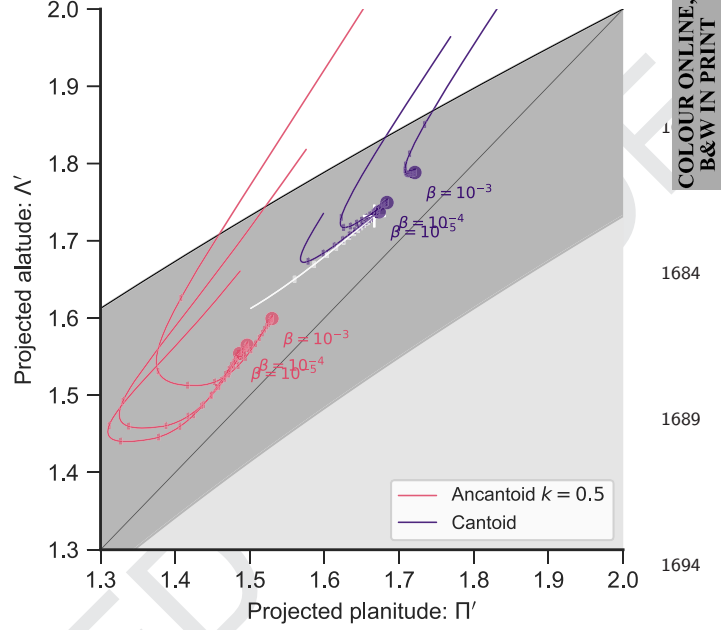


**Figure 21.** As Fig. 20(a) but zoomed in to show the wilkinoid track (white) and the convergence of the cantoid tracks (purple) to the wilkinoid as  $\beta \rightarrow 0$ .

1684

1689

1694

1704

1709

1714

1719

1724

1729

Ancantoids with different degrees of inner wind anisotropy are shown in Fig. 20(b). In all cases, the tracks follow hyperboloid-like behaviour at high inclinations, tending to populate the region just above the diagonal  $\Lambda' = \Pi'$ . The  $k = 0$  ancantoids show a kink in their tracks at the point where the projected apex passes through  $\theta = 90^\circ$ , due to the discontinuity in the second derivative of  $R(\theta)$  there (see footnote 9). The wilkinoid has a much less interesting track, most clearly seen in the zoomed Fig. 21, simply moving the short distance from  $(\frac{5}{3}, \sqrt{3})$  to  $(\frac{3}{2}, \sqrt{\frac{8}{3}})$ . Despite its location in the ellipsoid region of the plane, the fact that it has  $\theta_\infty = 180^\circ$  means that it behaves more like a parabola at high inclination, but converges on  $(\frac{3}{2}, \sqrt{\frac{8}{3}})$  instead of  $(2, 2)$  since the far wings are asymptotically cubic, rather than quadratic.

The local density of tick marks gives an indication of how likely it would be to observe each portion of the track, assuming an isotropic distribution of viewing angles. It can be seen that the ticks tend to be concentrated towards the beginning of each track, near the  $|i| = 0$  point, so the hyperboloid-like portions of the tracks would be observed for only a relatively narrow range of inclinations. This concentration becomes more marked as  $\beta$  becomes smaller, which helps to resolve the apparent paradox that the wilkinoid corresponds to the  $\beta \rightarrow 0$  limit of the cantoids, and yet follows a qualitatively different track. The detailed behaviour of the small- $\beta$  cantoid models is shown in Fig. 21, which zooms in on the region around the wilkinoid track. It can be seen that for  $\beta < 0.001$  the cantoid tracks begin to develop a downward hook, similar to the  $k = 0.5$  ancantoids discussed above. For  $\beta < 10^{-4}$ , this begins to approach the wilkinoid track, and the high-inclination, upward portion of the track becomes less and less important as  $\beta$  decreases.

## 6 MORE REALISTIC BOW SHOCK MODELS

The assumptions underlying the models of the previous section may break down in various ways. To test whether the planitude-alatitude analysis is still useful in less ‘ideal’ situations, we here apply

1734

it to more realistic simulations of stellar bow shocks. We choose a pair of hydromagnetic (HD) and magnetohydrodynamic (MHD) moving-star simulations from Meyer et al. (2017), in which the only difference is the presence (MHD case) or absence (HD case) of an ambient magnetic field with strength  $B = 7 \mu\text{G}$ , oriented parallel to the stellar velocity. In each case, the inner wind comes from a  $20 M_{\odot}$  main-sequence star, with mass-loss rate and terminal velocity that are roughly constant with time at  $\dot{M}_w \approx 4 \times 10^{-7} M_{\odot} \text{ yr}^{-1}$  and  $V_w \approx 1200 \text{ km s}^{-1}$ , while the outer wind is a parallel stream due to the star's own motion at  $40 \text{ km s}^{-1}$  through a uniform medium of density  $0.57 \text{ cm}^{-3}$ .

For these parameters, the radiative cooling distance for shocked ambient gas in the bow is a significant fraction ( $\approx 10$  per cent) of the bow shock size,  $R_0$ , tending to increase towards the wings, and the radiative cooling in the shocked stellar wind is even less efficient. This represents a significant violation of the assumptions behind the thin-shell models, since the total shocked shell thickness is of the same order as  $R_0$ . Nevertheless, the emissivity of several observationally important emission processes, such as mid-infrared thermal dust emission and the optical H $\alpha$  emission line, is concentrated near the contact discontinuity,<sup>11</sup> so it is reasonable to use this surface as a first approximation for the shape of the bow.

We have traced the contact discontinuity in the two models, using the procedure outlined in Fig. 22, and show results for the parabolic departure function (see Section 4.1) as blue symbols in Fig. 23. The MHD simulation shows a strongly negative dip in the departure function close to the apex ( $\cos \theta = 1$ ), indicating a very flat shape.<sup>12</sup> The HD simulation shows only a small negative dip in the departure function at the apex, but otherwise approximately follows the wilkinoid curve in the forward hemisphere. In both cases, the departure function is more positive than the wilkinoid in the far wings ( $\cos \theta < -0.5$ ), but we do not have data for the full range of  $\theta$ , and so two different extrapolations for  $\theta \rightarrow 180^\circ$  are shown. In the first (dashed red line in figure), we fit a low-order polynomial of  $\cos \theta$  to the points with  $\cos \theta < -0.5$  and extend it to  $\cos \theta = -1$ , which gives an asymptotically closed shape. In the second extrapolation (solid red line in figure), we fit a polynomial that is multiplied by  $(1 + \cos \theta)^{1/2}$ , which forces the departure function to zero at  $\cos \theta = -1$ , giving an asymptotically open shape, as with the wilkinoid. In a true steady state, the far wings should be asymptotically open, but as  $\theta \rightarrow 180^\circ$  the flow times become longer and longer, so that a bow shock with a finite age will be closed.

Using a 12th-order Chebyshev fit to the traced shapes, we show the apparent shape of the contact discontinuity at a series of inclination angles,  $|i|$ , in Fig. 24. The four panels show the two simulations for each of the two far-wing extrapolations. Comparison with Figs 18 and 19 shows the general tendency is the same as with the wilkinoid: that the apex becomes less flat and the wings less open

<sup>11</sup> Note that, in the non-magnetic HD models, efficient thermal conduction leads to a thick layer of hot, thermally evaporated ambient material that separates the shocked stellar wind from the cool, dense shell of shocked ambient gas (see section 3.3 of Meyer et al. 2014). In this case, the contact discontinuity is taken to be the boundary between hot and cold ambient gas, as opposed to the *material discontinuity* between shocked ambient gas and shocked wind gas. In the MHD models, the thermal conduction is almost completely suppressed, so that the material and contact discontinuities coincide.

<sup>12</sup> Meyer et al. (2017) speculate that this flatness may be the signature of the formation of a complex multiple-shock topology at the apex (de Sterck & Poedts 1999). For our purposes, the reason does not matter, merely that the magnetic and non-magnetic models predict markedly different shapes.

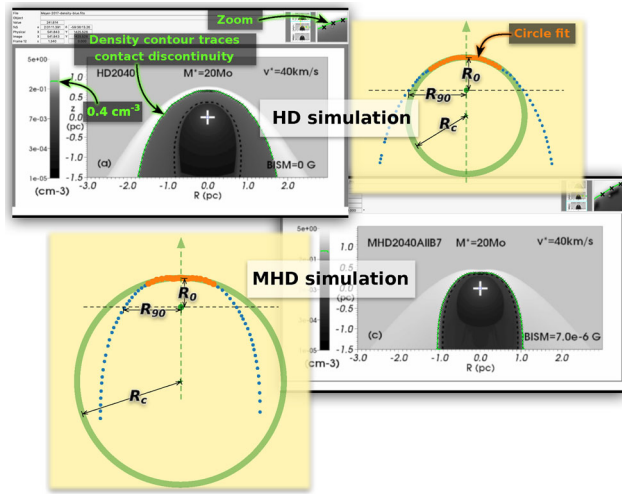


**Figure 22.** Procedure for tracing the contact discontinuity from the Meyer et al. (2017) simulations. The density maps from Meyer et al.'s fig. 3 are converted to FITS format and displayed using the software SAOIMAGE DS9 (Joye & Mandel 2003). The density contour at  $0.4 \text{ cm}^{-3}$  is displayed (shown in green in the figure), and this is traced by hand by placing 'point regions' on the image (shown by black 'x' shapes in the figure). The zoom facility of the software allows the points to be placed with any required accuracy. The points are saved to a file in the DS9 region file format, which is then read by PYTHON programs for further processing. For example, the yellow boxes show circle fits and determination of the parameters  $R_0$ ,  $R_c$ , and  $R_{90}$ . In this example, only the points shown in orange (within  $60^\circ$  of axis) are used in the fits.

as the inclination angle is increased. There is no sign of the sudden increase in openness at high inclination, as seen in the cantoids and ancantoids that are asymptotically hyperbolic. On the other hand, the projected shapes of both simulations vary much more strongly with  $|i|$  than the wilkinoid does. For the HD simulation, this is mainly apparent for  $|i| > 30^\circ$ , but for the MHD simulation it occurs at all inclinations.

The resultant inclination-dependent tracks in the planitude–alatitude plane are shown in Fig. 25. These are compared with measurements<sup>13</sup> from post-processed infrared dust continuum maps at  $60 \mu\text{m}$  (section 4.3 of Meyer et al. 2017), shown by open square symbols for  $i = 30^\circ, 45^\circ$ , and  $60^\circ$ . The agreement between the two is good. In particular, the  $60 \mu\text{m}$ -derived shapes are always very close to the tracks derived from the contact discontinuity shape. Also, the ordering of the three inclinations along the tracks corresponds to what is predicted, although quantitatively there are some slight deviations. This close agreement stems from the fact, emphasized by Meyer et al. (2014), that the long-wavelength dust emission from hot-star bow shocks tends to be dominated by material just outside the contact discontinuity. Note that there is almost no difference in the planitude–alatitude tracks between the closed and open extrapolations. This is because  $\Pi'$  and  $\Lambda'$  only depend on the portion of  $R(\theta)$  between  $\theta_0$  (equation 18) and  $\theta_{90}$  (equation 21), and these

<sup>13</sup> The shape measurements were performed by converting to contours the  $60 \mu\text{m}$  images in Meyer et al. (2017)'s fig. 10 and then tracing the ridge of minimum radius of curvature of the contours. Identical results are found from using the  $100 \mu\text{m}$  maps instead. For the  $25 \mu\text{m}$  maps, although the same results are found for low inclinations, in the maps with  $|i| \geq 45^\circ$  in the HD case, it becomes impossible to trace the limb-brightened rim because it becomes fainter than the emission from the true apex of the bow.

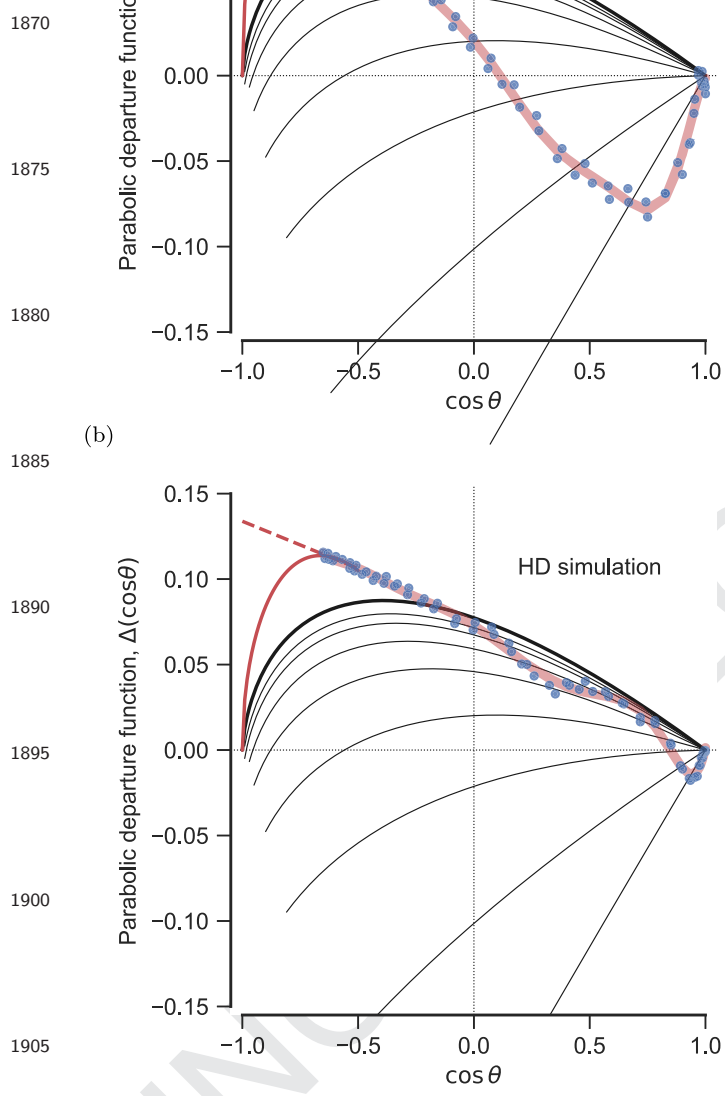


**Figure 23.** Departure function for the shape of the contact discontinuity, measured from two numerical simulations of a  $20 M_{\odot}$  main-sequence star, moving at  $40 \text{ km s}^{-1}$  through a uniform medium of density  $0.57 \text{ cm}^{-3}$  (Meyer et al. 2017). (a) MHD simulation with ambient magnetic field of strength  $7 \mu\text{G}$ , oriented parallel to the stellar velocity. (b) Hydrodynamic simulation with zero magnetic field. Blue dots show the measured shape, while the thick, pale-red line shows a 12th-order Chebyshev polynomial fit. The published shapes only extend to  $\theta \approx 130^\circ$ – $150^\circ$ , so we extrapolate the shapes out to  $\theta = 180^\circ$ . Two different extrapolations are shown, corresponding to bows that are asymptotically closed (dashed red line) or open (solid red line). For comparison, black lines show the departure function for wilkinoid (thick line) and cantoids (thin lines).

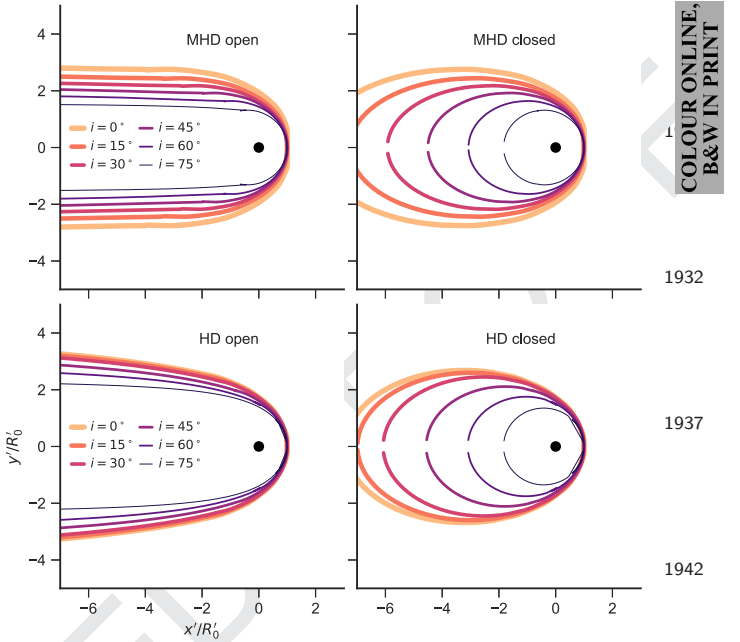


**Figure 24.** Projected shapes of contact discontinuity from simulations at different inclinations  $|i|$  (varying line colour and thickness, see key). The top row shows magnetized simulation of Fig. 23(a), and the bottom row shows non-magnetized simulation of Fig. 23(b). The left column shows asymptotically open extrapolation, and the right column shows asymptotically closed extrapolation. All shapes are normalized to the projected apex distance,  $R'_0$ .

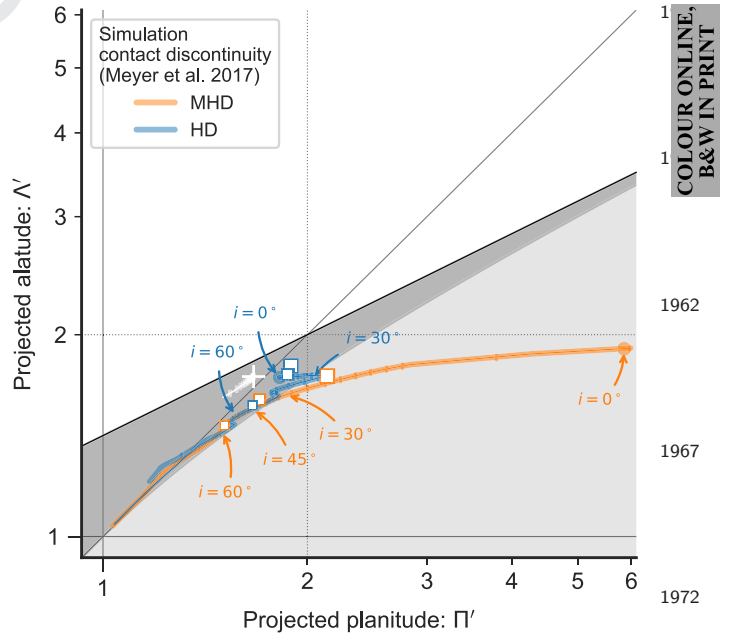


**Figure 25.** Apparent projected shapes of simulations in the  $\Pi' - \Lambda'$  plane. Thick solid lines show the predicted inclination-dependent tracks of the traced contact discontinuity shape for the asymptotically open extrapolation, with tick marks indicating 20 equal intervals in  $|\sin i|$ . Thin solid lines show the same for the asymptotically closed extrapolation, which only deviates from the open case at the high- $|i|$  end of the HD tracks. The true planitude and alatitude are marked by filled circle symbols. Open square symbols show the shapes traced from the dust emission maps at  $60 \mu\text{m}$  for inclinations of (largest to smallest)  $30^\circ$ ,  $45^\circ$ , and  $60^\circ$ . For comparison, the wilkinoid track is shown in white. Note that the scales of both axes are logarithmic in this case.

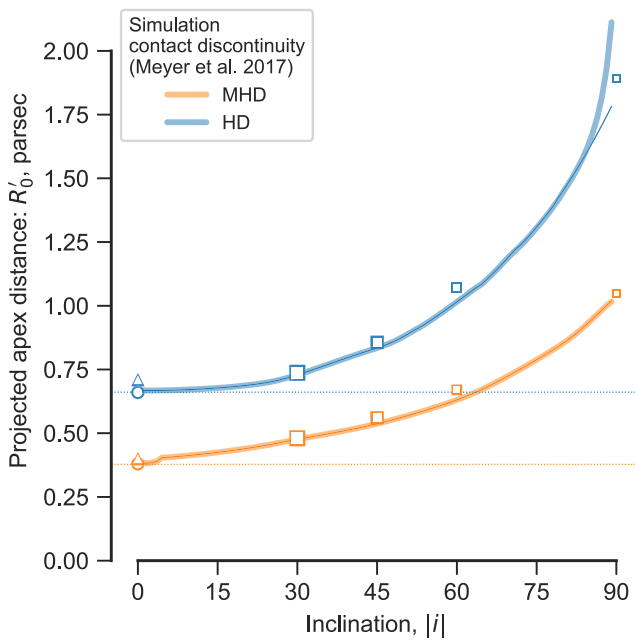


**Figure 26.** Apparent projected apex distance of simulations. Line and symbol meanings are as in Fig. 25. In addition, triangle symbols at  $|i| = 0^\circ$  denote radius measured on H $\alpha$  optical emission maps. Note that the distances for the blue square symbols have been adjusted according to the correction factor discussed in footnote 14.

are both smaller than the  $\theta$  range where extrapolation is necessary, except for in the HD case at the highest inclinations.

Fig. 26 shows the inclination dependence of the projected apex distance,  $R'_0$ . As in the previous figure, the lines show the prediction based on the shape of the contact discontinuity, while the square symbols show the results from the 60  $\mu\text{m}$  dust continuum maps.<sup>14</sup> In addition, triangle symbols show results from H $\alpha$  optical emission line maps, which are given for  $i = 0$  in fig. 7 of Meyer et al. (2017). Again, the agreement is good between the values derived from the shape of the contact discontinuity and those derived from the surface brightness maps. The greatest discrepancy is seen with the H $\alpha$  maps and the intermediate inclination dust maps, with  $R'_0$  being overestimated by a few per cent in both cases. The differences in behaviour between the two simulations are much larger than this. The larger true planitude of the MHD simulation means that the relative increase of  $R'_0$  with  $|i|$  is much stronger than in the HD simulation for  $|i| < 45^\circ$ , as expected from Fig. 10(b).

<sup>14</sup> There is an apparent error in the spatial scales for the HD simulations in figs 10 and 11 of Meyer et al. (2017), with the dust emission peaks occurring at radii that are clearly too large. The stated apex distance for the contact discontinuity in this simulation is 0.69 pc from table 2 of Meyer et al. (2014), and the position of the peak in dust column density is 0.70 pc from fig. 17(a) of Meyer et al. (2014). These are consistent with figs 3, 4, and 7 of Meyer et al. (2017), but not with figs 10 and 11. Luckily, the position of the true apex is clearly visible in the 25  $\mu\text{m}$  maps of fig. 10 at inclinations of  $45^\circ$  and  $60^\circ$ . The projected separation of the true apex is  $R_0 \cos i$ , independent of the bow shape, which allows a correction factor of 0.65 to be found, assuming that the on-axis peak in the 25  $\mu\text{m}$  emission coincides with the peak in dust column density. This correction has been applied to the blue square symbols shown in our Fig. 26.

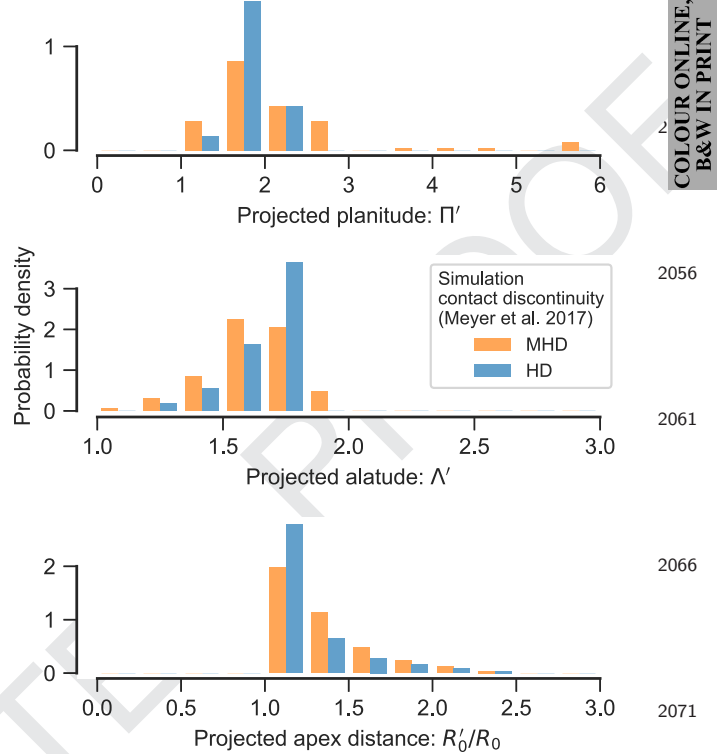


**Figure 27.** Histograms of (top to bottom) projected planitude, alatitude, and bow shock size for the shape of the contact discontinuity in the Meyer et al. (2017) simulations. The y-axis gives the probability density (per unit x-axis quantity), assuming a uniform distribution of viewing directions.

The probability densities<sup>15</sup> of the apparent shape and size of the simulation bows (measured at the contact discontinuity) are shown in Fig. 27, assuming that the viewing direction is uniformly distributed in solid angle. The modal value of the projected planitude is similar at  $\Pi' \approx 1.8$  for both simulations, but the distribution is much broader in the MHD case, which has a low-level wing extending out to  $\Pi' \approx 6$ . The projected alatitude distributions are both narrower than the planitude (note the different scale of the histogram axis), with the MHD case again being the broader of the two and peaking at a slightly lower value ( $\Lambda' \approx 1.7$  as opposed to  $\approx 1.8$  for the HD case). Finally, the distribution of projected-overtrue apex distance is also broader for the MHD case.

## 7 EXAMPLE APPLICATION TO OBSERVATIONS

As an example of measuring the projected planitude and alatitude of real bow shocks, we present an analysis of M42 000-400 and M42 069-601, which are two H $\alpha$  emission arcs (Bally, O'Dell & McCaughrean 2000; Gutiérrez-Soto 2015) associated with proplyds<sup>16</sup> in the west of the Orion nebula (M42) at a distance of roughly 0.5 pc from the high-mass Trapezium stars that ionize

<sup>15</sup> The probability density is defined so that its integral over the full range of the histogrammed variable is unity, making it independent of the histogram bin widths. This means that the characteristic width of an approximately unimodal distribution is one over the maximum probability density.

<sup>16</sup> The coordinate designation (see O'Dell & Wen 1994 for an explanation of the nomenclature) of 000-400 is very imprecise in right ascension, but we use it here for consistency with previous papers. The associated proplyd

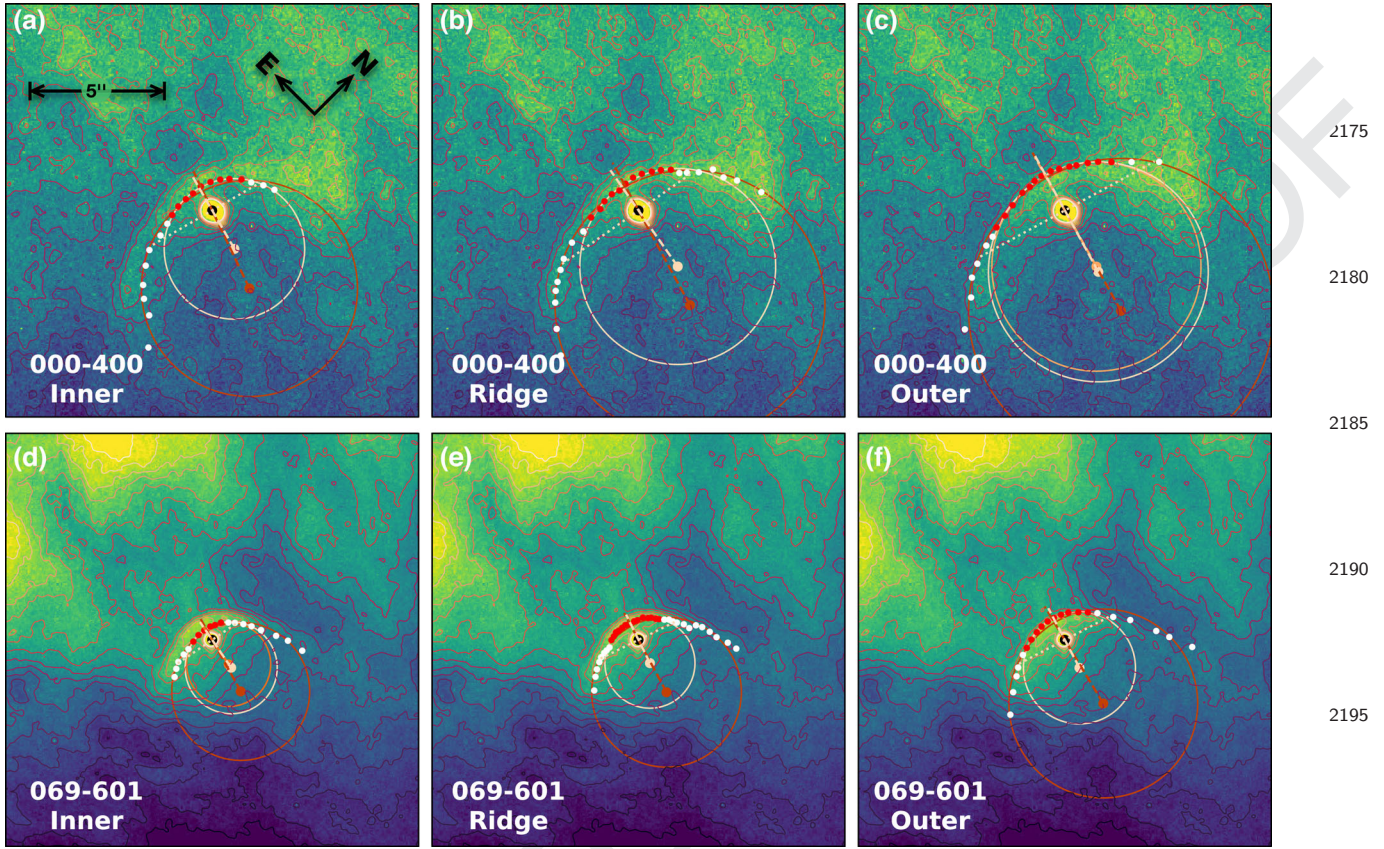


**Figure 28.** Example empirical determination of planitude and alatitude for observed bow shocks associated with proplyds in the outer Orion nebula (M42). Colour scale and contours show a *Hubble Space Telescope* H $\alpha$  image (ACS F658N filter; Bally et al. 2006) of M42 000-400 (panels a–c) and M42 069-601 (panels d–f). The image scale and orientation are indicated in panel (a) and are the same for all panels. Three different bows have been traced by eye on each object (red and white filled symbols): (a, d) inner edge, (b, e) ridge of maximum emission, and (c, f) outer edge. For each panel, the dark-coloured circle shows the initial fit to the full set of points (white and red), using the algorithm described in Appendix E. The centre of curvature and derived axis are shown by a small filled circle and dashed line in the same colour. Lighter coloured circles show three subsequent iterations where the fit is restricted to points within  $\pm\Delta\theta = 75^\circ$  of the axis. The subset of points used in the final iteration is marked in red. The perpendicular radii for the final iteration are shown by dotted lines. In panels (a), (b), and (d)–(f), the iterations converge immediately, but in panel (c) the iterations stably oscillate between two slightly different solutions.

the nebula. An image of one of these arcs (M42 069-601) was used in the illustration of bow shock terminology in Fig. 1.

### 7.1 Empirical determination of bow shock shape

We consider three different tracings of the bow shape (see Fig. 28): the peak of the emission arc ('ridge'), and its inner and outer edges. In all three cases, we placed by eye the points that define the bow, Q11 using SAOIMAGE DS9 (Joye & Mandel 2003) in a similar fashion to in Fig. 22, and guided by the image contours.<sup>17</sup>

We determine the planitude and alatitude by fitting a circle to the traced points within  $\pm\Delta\theta = 75^\circ$  of the bow axis, using the iterative algorithm described in Appendix E. The fitted circle, when combined with the position of the central source, yields the orientation of the bow axis, together with the apex distance,  $R_0$ , radius of curvature,  $R_c$ , and two perpendicular radii (one for each wing),  $R_{90+}$  and  $R_{90-}$ . These are all indicated in the panels of Fig. 28 by light-

2168 is listed with the more correct designation 4596-400 in catalogues such as Ricci, Roberto & Soderblom (2008).

<sup>17</sup> In the case of the 'ridge' method at least, it is possible to automate this step, which we will discuss in detail in a following paper.

2205 coloured lines.<sup>18</sup> The projected planitude and alatitude then follow as  $\Pi' = R_c/R_0$ ,  $\Lambda'_+ = R_{90+}/R_0$ ,  $\Lambda'_- = R_{90-}/R_0$ , which are shown in Fig. 29.

### 7.2 Analysis of sources of systematic uncertainty

The planitude is found to have a moderate dependence on the choice of  $\Delta\theta$ , as shown in Fig. 30, where it can be seen that, although the values of  $\Pi'$  are relatively stable for  $\Delta\theta \geq 60^\circ$  (light grey shaded region), they can show much larger variations for  $\Delta\theta < 60^\circ$ . The fact that the radius of curvature is defined at a point (the projected apex) might seem to argue for making  $\Delta\theta$  as small as possible, but that would lead to circle fits that were extremely sensitive to the exact positions of the few points included in the fit. A reliable fit requires four or more points, ideally spanning a total separation that is a substantial fraction of  $R_c$ , which would argue for  $\Delta\theta$  larger than about  $\Pi'/2$  rad, or  $60^\circ$ – $90^\circ$ . On the other hand, if  $\Delta\theta \geq 90^\circ$ , then the planitude and alatitude would no longer be independent since the bow would be forced to lie on the 'sphere' line,  $\Lambda' = (2\Pi' - 1)^{1/2}$  (see Section 4). Balancing these two concerns suggests an optimal

<sup>18</sup> For conciseness, we drop the prime symbol from the radii, both in this section and in Appendix E, even though they are all projected quantities.

2242

2247

2252

2257

2267

2272

2277

2282

2287

2292

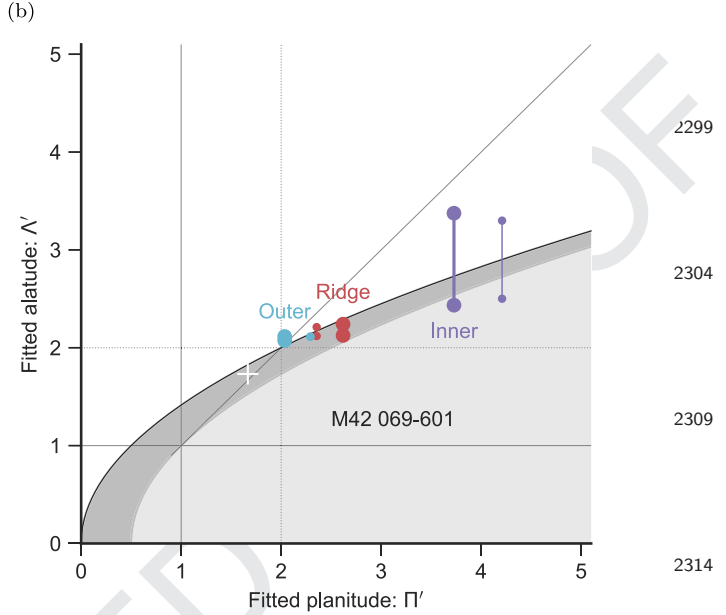
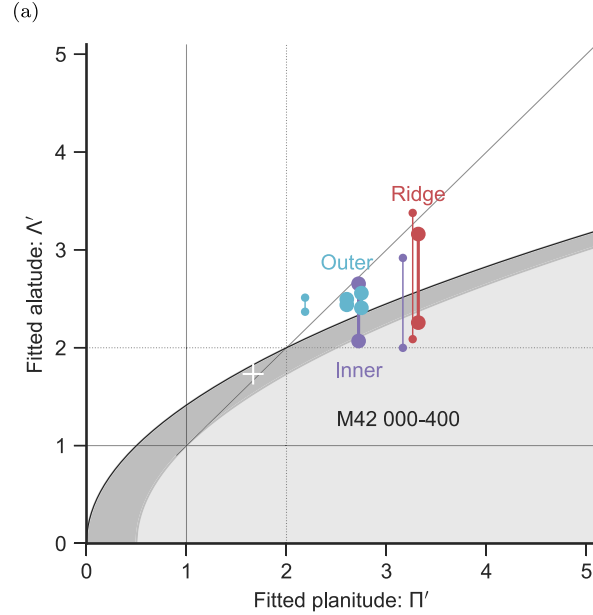


**Figure 29.** Location in the projected planitude–alatitude plane of the converged circle fits to the M42 bows: (a) 000-400, (b) 069-601. For each solution, the two values of the projected alatitude,  $\Lambda'_+$  and  $\Lambda'_-$ , corresponding to  $R_{90+}$  and  $R_{90-}$ , are joined by a vertical line. Large symbols show the results from the fits shown in Fig. 28, while small symbols show results for fits using  $\Delta\theta = 60^\circ$  instead of  $75^\circ$ . In panel (a), two slightly different  $\Pi'$  values are shown for the outer bow, since the fit does not converge to a single value [see Fig. 28(c) and Appendix E].

2319

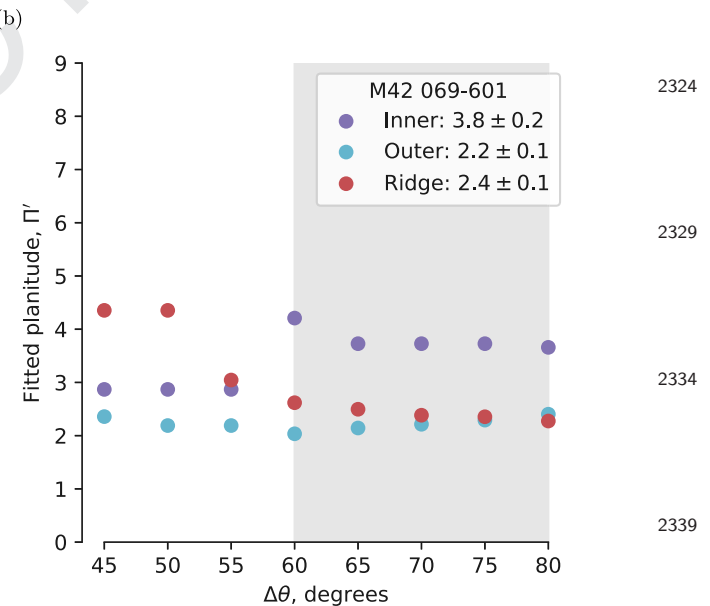
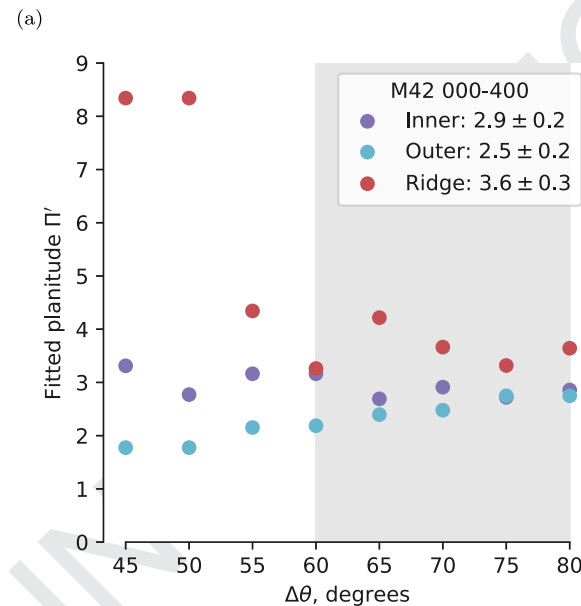


**Figure 30.** Variation of fitted planitude,  $\Pi'$ , as a function of the parameter  $\Delta\theta$ , which controls how close a point must be to the axis in order to be included in the circle fit. (a) M42 000-400, (b) M42 069-601. For the three traced bows (inner, outer, and ridge) of each object, the symbol key lists the mean and standard deviation of  $\Pi'$ , calculated over the ‘stable’ range  $\Delta\theta = 60^\circ–80^\circ$ , which is indicated by light grey shading.

2344

$\Delta\theta = 75^\circ$ , which is shown in Fig. 28, whereas in Fig. 29 we show results for both  $75^\circ$  (thick lines) and  $60^\circ$  (thin lines).

Unlike all the models considered in Sections 5 and 6, the observed bows are not necessarily symmetrical and so the alatitude for the two wings,  $\Lambda'_-$  and  $\Lambda'_+$ , may be different. We therefore calculate an average alatitude,  $\langle \Lambda' \rangle$ , and an alatitude asymmetry,  $\Delta \Lambda'$ :

$$\langle \Lambda' \rangle = \frac{1}{2} (\Lambda'_+ + \Lambda'_-) \quad \Delta \Lambda' = \frac{1}{2} (\Lambda'_+ - \Lambda'_-). \quad (64)$$

The results for these two quantities, together with the planitude, are shown in Table 1. For each object and for each tracing (inner, ridge, outer, see Fig. 28), the mean  $\pm$  standard deviation is listed for circle fits using  $\Delta\theta = 60^\circ–80^\circ$  (see Fig. 30). Additionally, the row ‘All’ for each object gives the global mean and standard deviation over all three tracings.

It can be seen from Table 1 that the uncertainty in the fitted parameters is dominated by the variations between the different tracings. For example, the one-sigma relative variation of planitude,  $\Pi'$ , is  $<10$  per cent within the individual tracings, but

2349

2354

**Table 1.** Fitted planitude and alatitude for M42 bows.

Source	Bow	$\Pi'$	$\langle \Lambda' \rangle$	$\Delta\Lambda'$
2361	000-400 Inner	$2.87 \pm 0.19$	$2.40 \pm 0.04$	$0.35 \pm 0.08$
	Ridge	$3.62 \pm 0.38$	$2.73 \pm 0.02$	$0.51 \pm 0.10$
	Outer	$2.51 \pm 0.24$	$2.46 \pm 0.02$	$-0.06 \pm 0.02$
	All	$3.00 \pm 0.54$	$2.53 \pm 0.15$	$0.16 \pm 0.16$
2366	069-601 Inner	$3.81 \pm 0.23$	$2.90 \pm 0.01$	$0.44 \pm 0.05$
	Ridge	$2.43 \pm 0.13$	$2.17 \pm 0.01$	$0.07 \pm 0.02$
	Outer	$2.22 \pm 0.15$	$2.11 \pm 0.01$	$0.01 \pm 0.01$
	All	$2.82 \pm 0.75$	$2.39 \pm 0.37$	$0.17 \pm 0.20$

≈20 per cent between tracings. For the mean alatitude,  $\langle \Lambda' \rangle$ , the variation within individual tracings is extremely small<sup>19</sup> at ≈1 per cent, but is ≈10 per cent between tracings. The alatitude asymmetry,  $\Delta\Lambda'$ , is best interpreted as a difference between the symmetry axis of the apex region and the symmetry axis of the wings. In relative terms, this is 0–20 per cent, but with large systematic variations between tracings (for instance, in both objects it is very small for the outer arcs).

It could be argued that much of the between-tracing variations in  $\Pi'$  and  $\langle \Lambda' \rangle$  are due to real differences between the shapes of the inner and outer boundaries of the emission arc. Although this may be true, in the absence of a robust theory as to exactly what feature of the observed images constitutes the bow shock, such variations nevertheless serve to limit the precision with which the bow shock shape can be measured. We therefore conclude that conservative estimates of 20 per cent precision for  $\Pi'$  and 10 per cent precision for  $\Lambda'$  are appropriate when analysing observations of a similar or better quality<sup>20</sup> to those presented in Fig. 28. This will be an important limitation when comparing the statistics of the shapes of different bow shock populations, as we will present in a following paper.

### 7.3 Derived shape of the M42 arcs

From a casual inspection of Fig. 28, it is apparent that the shapes of the two M42 arcs are closely similar, and this is confirmed by the numbers in Table 1. Both 000-400 and 069-601 are consistent with  $(\Pi', \Lambda') \approx (3.0, 2.5)$ , and if we take the absolute minimum over all the different tracings and reasonable variations in the  $\Delta\theta$  fit parameter, we find unassailable lower limits of  $(\Pi', \Lambda') > (2.1, 2.1)$ . In the rest of this section, we consider only these lower limits, since they are already sufficient for drawing interesting conclusions.

Comparison with Fig. 25 shows that both the MHD and HD simulations of Meyer et al. (2016) are inconsistent with the observations. Although  $\Pi' > 2.1$  can be satisfied,<sup>21</sup> the simulations’ projected alatitude is  $\Lambda' < 1.9$  for all inclinations, which is significantly less than the observed lower limit of 2.1. This is not particularly surprising since the simulations were not tailored to the situation of these proplyd bow shocks in M42, in which the mildly supersonic photo-

evaporation flow from an externally irradiated protoplanetary disc interacts with the mildly supersonic champagne flow from the core of the Orion nebula. The proplyd case has at least four important differences from the runaway O-star case modelled by Meyer et al. (2016). (1) The velocity of the outer wind is  $\leq 20 \text{ km s}^{-1}$  instead of  $40 \text{ km s}^{-1}$ . (2) The outer wind is slightly divergent, rather than plane parallel. (3) Both inner and outer shocks are strongly radiative, so both shells (see Fig. 2) contribute to the observed emission. (4) The inner wind is not isotropic, but instead corresponds to the  $k = 0.5$  case of equation (53). The ways in which these differences may account for the discrepancy with the observations will be explored in detail in a subsequent paper.

## 8 SUMMARY AND DISCUSSION

We have shown that the shapes of stellar bow shocks can be usefully characterized by two dimensionless numbers: the *planitude*,  $\Pi$ , or flatness of the bow’s apex, and the *alatitude*,  $\Lambda$ , or openness of the bow’s wings (Section 2). The planitude and alatitude can be estimated from ratios of lengths that can be straightforwardly measured from observations or theoretical models. We develop a general method (Section 3) for finding the projected shape,  $(\Pi', \Lambda')$ , of a bow shock’s limb-brightened edge, or *tangent line*, as a function of inclination angle,  $i$ , where the emission shell is idealized as a cylindrically symmetric surface.

We first apply this method to find inclination-dependent tracks on the projected planitude–alatitude plane for the special case of *quadric* surfaces (Section 4), such as hyperboloids, paraboloids, and spheroids, where the tangent line is a conic section. The spheroids and hyperboloids occupy distinct regions of the plane, with the paraboloids defining the boundary between the two. As the inclination is increased from  $|i| = 0$  (side-on) to  $|i| = 90^\circ$  (end-on), the tracks first tend to approach the diagonal  $\Lambda' = \Pi'$ , corresponding to confocal conics, always remaining within their own region. At the highest inclinations, the spheroids all converge at  $|i| = 90^\circ$  on the point  $(\Pi', \Lambda') = (1, 1)$  and the paraboloids on the point  $(\Pi', \Lambda') = (2, 2)$ . The hyperboloids, on the other hand, diverge as  $(\Pi', \Lambda') \rightarrow (\infty, \infty)$  for a finite  $i_{\text{crit}}$ , which depends on the asymptotic opening angle of the tail. For  $|i| > i_{\text{crit}}$ , the tangent line no longer exists for the hyperboloid, and it would no longer appear to be a curved bow shock. We introduce the parabolic departure function (Section 4.1) as tool for visualizing differences in bow shapes,  $R(\theta)$ , over the full range,  $\theta = [0^\circ, 180^\circ]$ .

We then apply the projection method to a set of thin-shell hydrodynamic models of bow shocks (Section 5): the *wilkinoid* from a wind–parallel stream interaction and the *cantoids* from wind–wind interactions. We generalize the latter to the *ancantoids*, where one of the winds is anisotropic. We find that the wilkinoid is confined to a small region of the  $\Pi'-\Lambda'$  plane, with projected planitude and alatitude varying with inclination by <15 per cent. The cantoids and ancantoids with sufficiently small values of  $\beta$ , the wind momentum ratio, have more interesting behaviour, with tracks that pass from the spheroid region at low inclinations to the hyperboloid region at high inclinations.

In the following section (Section 6), we test the projected shape analysis methods against the results of computational fluid dynamic simulations of magnetized and non-magnetized bow shocks from Meyer et al. (2017) of a runaway OB main-sequence star. We find that measurements made on maps of infrared dust emission can be accurate diagnostics of the projected shape of the contact discontinuity for this type of bow shock (Fig. 25). The distributions of projected planitude and alatitude for a population of randomly

<sup>19</sup> This is because the only way that variation in the circle fit parameters affects the alatitudes is through the axis orientation vector, and changing the orientation induces roughly opposite effects on  $\Lambda'_+$  and  $\Lambda'_-$ , which approximately cancel out in  $\langle \Lambda' \rangle$ .

<sup>20</sup> Since the uncertainties are systematic and due to unavoidably subjective decisions, it is unlikely that better quality observations would improve the situation, although poorer quality observations could make things worse.

<sup>21</sup> Either by the MHD simulations at low inclinations ( $|i| = 0^\circ\text{--}20^\circ$ ) or by the HD simulation at intermediate inclinations ( $|i| = 30^\circ\text{--}40^\circ$ ).

oriented bow shocks show systematic differences between the different simulations.

Finally (Section 7), we give an example of the application of our methods to observed emission maps of bow shocks, describing a robust algorithm for empirically determining the projected planitude and alatitude from imperfect real data. We investigate the sensitivity of the results to systematic errors due to both observational uncertainties and subjective choices in the application of the algorithm. We find that the projected planitude and alatitude can be determined with precisions of 20 per cent and 10 per cent, respectively. For our illustrative observations, we show that this is more than sufficient to rule out certain models.

This paper is the first of a series that will apply our shape analysis to a wide variety of models and observations of stellar bow shocks. In a second paper, we consider the alternative model of dusty radiation-driven bow wave (Ochsendorf et al. 2014), instead of a hydrodynamic bow shock, and also calculate the signature in the planitude–alatitude plane of oscillations in the bow shape, which may be due to instabilities or a time-varying source. In a third paper, we apply our techniques to observational data sets for three different classes of stellar bow shocks: OB stars (Kobulnicky et al. 2016), cool giants/supergiants (Cox et al. 2012), and young stars in the extended Orion nebula (Henney et al. 2013). In a fourth paper, we analyse the proplyd bow shocks in the core of the Orion nebula (García-Arredondo et al. 2001).

## ACKNOWLEDGEMENTS

We are grateful for financial support provided by Dirección General de Asuntos del Personal Académico, Universidad Nacional Autónoma de México, through grant Programa de Apoyo a Proyectos de Investigación e Innovación Tecnológica IN111215. JATY acknowledges support via a research studentship from Consejo Nacional de Ciencias y Tecnología, Mexico. This work has made extensive use of PYTHON language libraries from the SCIPY (Jones et al. 2018) and ASTROPY (Astropy Collaboration et al. 2013, 2018) projects. We appreciate the thoughtful comments of the anonymous referee, which led us to clarify the presentation of our results and prompted the addition of Section 7 and Appendices A and B.

## REFERENCES

- Astropy Collaboration et al., 2013, *A&A*, 558, A33  
 Q12 Astropy Collaboration et al., 2018, preprint ([arXiv:1801.02634](https://arxiv.org/abs/1801.02634))  
 2525 Bally J., O'Dell C. R., McCaughrean M. J., 2000, *AJ*, 119, 2919  
 Bally J., Licht D., Smith N., Walawender J., 2006, *AJ*, 131, 473  
 Canto J., Raga A. C., Wilkin F. P., 1996, *ApJ*, 469, 729 (CRW)  
 Cox N. L. J. et al., 2012, *A&A*, 537, A35  
 de Sterck H., Poedts S., 1999, *A&A*, 343, 641  
 García-Arredondo F., Henney W. J., Arthur S. J., 2001, *ApJ*, 561, 830  
 Gayley K. G., 2009, *ApJ*, 703, 89  
 Grferrer A., Zsombor-Murray P., 2009, *J. Geom. Graph.*, 13, 131  
 Goldman R., 1983, *IEEE Comput. Graph. Appl.*, 3, 68  
 Graham M. F., Meaburn J., Garrington S. T., O'Brien T. J., Henney W. J., O'Dell C. R., 2002, *ApJ*, 570, 222  
 Guggenheimer H., 2012, Dover Books on Mathematics, Differential Geometry. Dover Press, New York  
 Gutiérrez-Soto L. Á., 2015, Master's thesis, Universidad Nacional Autónoma de México, Mexico  
 Hartigan P., Raymond J., Hartmann L., 1987, *ApJ*, 316, 323  
 Hayward T. L., Houck J. R., Miles J. W., 1994, *ApJ*, 433, 157  
 Henney W. J., 2002, *Rev. Mex. Astron. Astrofis.*, 38, 71  
 Henney W. J., García-Díaz M. T., O'Dell C. R., Rubin R. H., 2013, *MNRAS*, 428, 691  
 Jones E. et al., 2018, SciPy: Open Source Scientific Tools for Python, Available at <http://www.scipy.org/>  
 Joye W. A., Mandel E., 2003, in Payne H. E., Jedzejewski R. I., Hook R. N., eds, ASP Conf. Ser. Vol. 295, Astronomical Data Analysis Software and Systems XII. Astron. Soc. Pac., San Francisco, p. 489  
 Kobulnicky H. A., Gilbert I. J., Kiminki D. C., 2010, *ApJ*, 710, 549  
 Kobulnicky H. A. et al., 2016, *ApJS*, 227, 18  
 Mackey J., Mohamed S., Neilson H. R., Langer N., Meyer D. M.-A., 2012, *ApJ*, 751, L10  
 Mackey J., Gvaramadze V. V., Mohamed S., Langer N., 2015, *A&A*, 573, A10  
 Markevitch M., Gonzalez A. H., David L., Vikhlinin A., Murray S., Forman W., Jones C., Tucker W., 2002, *ApJ*, 567, L27  
 Meaburn J., Boumis P., Akras S., 2013, *MNRAS*, 435, 3462  
 Medina S.-N. X., Arthur S. J., Henney W. J., Mellema G., Gazol A., 2014, *MNRAS*, 445, 1797  
 Meyer D. M.-A., Mackey J., Langer N., Gvaramadze V. V., Mignone A., Izzard R. G., Kaper L., 2014, *MNRAS*, 444, 2754  
 Meyer D. M.-A., van Marle A.-J., Kuiper R., Kley W., 2016, *MNRAS*, 459, 1146  
 Meyer D. M.-A., Mignone A., Kuiper R., Raga A. C., Kley W., 2017, *MNRAS*, 464, 3229  
 Mohr P. J., Phillips W. D., 2015, *Metrologia*, 52, 40  
 Ng C.-Y., Bandiera R., Hunstead R. W., Johnston S., 2017, *ApJ*, 842, 100  
 O'Dell C. R., Wen Z., 1994, *ApJ*, 436, 194  
 Ochsendorf B. B., Verdolini S., Cox N. L. J., Berné O., Kaper L., Tielens A. G. G. M., 2014, *A&A*, 566, A75  
 Penrose R., 2004, The Road to Reality: A Complete Guide to the Laws of the Universe. Jonathan Cape, London  
 Phillips J. P., Cuesta L. C., Ramos-Larios G., 2010, *MNRAS*, 409, 881  
 Quincey P., Brown R. J. C., 2017, *Metrologia*, 54, 454  
 Raga A. C., Binette L., Canto J., Calvet N., 1990, *ApJ*, 364, 601  
 Ricci L., Robberto M., Soderblom D. R., 2008, *AJ*, 136, 2136  
 Robberto M. et al., 2005, *AJ*, 129, 1534  
 Scherer K., Fichtner H., 2014, *ApJ*, 782, 25  
 Schwartz R. D., 1978, *ApJ*, 223, 884  
 Shu F. H., Lizano S., Galli D., Cantó J., Laughlin G., 2002, *ApJ*, 580, 969  
 Smith N., Bally J., Shuping R. Y., Morris M., Kassis M., 2005, *AJ*, 130, 1763  
 Stevens I. R., Blondin J. M., Pollock A. M. T., 1992, *ApJ*, 386, 265  
 Tenorio-Tagle G., 1979, *A&A*, 71, 59  
 van Buren D., McCray R., 1988, *ApJ*, 329, L93  
 van Dyke M., 1982, An Album of Fluid Motion. Parabolic Press, Stanford, CA  
 van Marle A. J., Meliani Z., Keppens R., Decin L., 2011, *ApJ*, 734, L26  
 Weisstein E. W., 2018, Radius of Curvature, From MathWorld – A Wolfram Web Resource, Available at <http://mathworld.wolfram.com/RadiusofCurvature.html>  
 Wilkin F. P., 1996, *ApJ*, 459, L31  
 Wilkin F. P., 1997, PhD thesis, Univ. California, Berkeley  
 Wilkin F. P., 2000, *ApJ*, 532, 400  
 Wilson A. S., Ulvestad J. S., 1987, *ApJ*, 319, 105  
 Zank G. P., 1999, *Space Sci. Rev.*, 89, 413

## APPENDIX A: RADIUS OF CURVATURE

The radius of curvature of a general curve can be written as (e.g. equations 2–5 of Guggenheimer 2012)

$$R_c \equiv \frac{1}{|\kappa|} = \left| \frac{ds}{d\alpha} \right|, \quad (A1) \quad 2597$$

where  $\kappa$  is the curvature,  $s$  is the path length along the curve, and  $\alpha$  is the tangent angle (see Fig. 6). In spherical polar coordinates, this becomes (Weisstein 2018)

$$R_c = \frac{(R^2 + R_\theta^2)^{3/2}}{|R^2 + 2R_\theta^2 - RR_{\theta\theta}|}, \quad (A2) \quad 2602$$

where  $R_\theta = dR/d\theta$  and  $R_{\theta\theta} = d^2R/d\theta^2$ . At the apex,  $R_\theta = 0$  by symmetry, which yields equation (3) of Section 2. Note that  $\theta$  is dimensionless and should be measured in radians (Mohr & Phillips 2015; Quincey & Brown 2017).

2609

## APPENDIX B: ROTATION MATRICES AND PLANE-OF-SKY PROJECTION

The transformation from the body-frame (unprimed) to observer-frame (primed) coordinates is a rotation about the  $y$ -axis by an angle  $i$ , which is described by the rotation matrix:

$$\mathbf{A}_y(i) = \begin{pmatrix} \cos i & 0 & -\sin i \\ 0 & 1 & 0 \\ \sin i & 0 & \cos i \end{pmatrix}. \quad (B1)$$

This is used in equation (8). A further application is to express the observer-frame Cartesian basis vectors in terms of the body-frame basis:

$$\hat{\mathbf{x}}' = \mathbf{A}_y(-i) \begin{pmatrix} 1 \\ 0 \\ 0 \end{pmatrix} = \begin{pmatrix} \cos i \\ 0 \\ -\sin i \end{pmatrix}, \quad (B2)$$

$$\hat{\mathbf{y}}' = \mathbf{A}_y(-i) \begin{pmatrix} 0 \\ 1 \\ 0 \end{pmatrix} = \begin{pmatrix} 0 \\ 1 \\ 0 \end{pmatrix}, \quad (B3)$$

$$\hat{\mathbf{z}}' = \mathbf{A}_y(-i) \begin{pmatrix} 0 \\ 0 \\ 1 \end{pmatrix} = \begin{pmatrix} \sin i \\ 0 \\ \cos i \end{pmatrix}. \quad (B4)$$

Note that in this case the sign of  $i$  is reversed because it is the inverse operation to that in equation (8).

Since we are considering cylindrically symmetric bows, all azimuths  $\phi$  are equivalent, so it is sufficient to work with two-dimensional curves in the plane  $z = 0$  (which is also  $\phi = 0$ ) and then find the three-dimensional surface by rotating about the  $x$ -axis via the rotation matrix:

$$\mathbf{A}_x(\phi) = \begin{pmatrix} 1 & 0 & 0 \\ 0 & \cos \phi & -\sin \phi \\ 0 & \sin \phi & \cos \phi \end{pmatrix}, \quad (B5)$$

where  $\phi$  takes all values in the interval  $[0, 2\pi]$ .

2649

## APPENDIX C: PARABOLOIDS AND THEIR PLANE-OF-SKY PROJECTION

Equation (25) for the  $xy$  coordinates of a quadric in the  $\phi = 0$  plane cannot be used in the case of a paraboloid ( $\mathcal{Q} = 0$ ). Instead, a convenient parametrization is

$$\begin{aligned} x &= R_0 \left( 1 - \frac{1}{2} \Pi t^2 \right) \\ y &= R_0 \Pi t, \end{aligned} \quad (C1)$$

where we have ‘baked in’ knowledge of the planitude,  $\Pi = R_c/R_0$  (see Section 2). The projected plane-of-sky coordinates of the tangent line follow from equation (8) as

$$\begin{aligned} x'_T/R_0 &= \left( 1 - \frac{1}{2} \Pi t^2 \right) \cos i + \Pi t \sin \phi_T \sin i \\ y'_T/R_0 &= \Pi t \cos \phi_T. \end{aligned} \quad (C2)$$

The azimuth of the tangent line is found from equations (10) and (15) as  $\sin \phi_T = -t^{-1} \tan i$ , so that

$$\begin{aligned} x'_T/R_0 &= \cos i \left[ 1 + \frac{1}{2} \Pi \tan^2 i - \frac{1}{2} \Pi (t^2 - \tan^2 i) \right] \\ y'_T/R_0 &= \Pi (t^2 - \tan^2 i)^{1/2}. \end{aligned} \quad (C3)$$

The projected star-apex distance,  $R'_0$ , is the value of  $x'_T$  when  $y'_T = 0$ , yielding

$$R'_0/R_0 = \cos i \left( 1 + \frac{1}{2} \Pi \tan^2 i \right). \quad (C4)$$

Note that the same result can be obtained from a Taylor expansion of equation (45) substituted into equation (49) in the limit  $\mathcal{Q} \rightarrow 0$ .

Equation (C3) can be rewritten in the form

$$\begin{aligned} x'_T &= R'_0 \left( 1 - \frac{1}{2} \Pi' t'^2 \right) \\ y'_T &= R'_0 \Pi' t', \end{aligned} \quad (C5)$$

where

$$\Pi' = \frac{2\Pi}{2 \cos^2 i + \Pi \sin^2 i} \quad (C6)$$

$$t' = \cos i (t^2 - \tan^2 i)^{1/2}, \quad (C7)$$

which demonstrates that the projected shape is also a parabola. It is apparent from equation (C6) that the projected planitude obeys

$$\lim_{i \rightarrow 90^\circ} \Pi' = 2,$$

for all values of the true planitude  $\Pi$ , as is shown by the black lines in Fig. 10(a). The projected alatitude can be found as

$$\Lambda' = (2\Pi')^{1/2}. \quad (C8)$$

For the special case of the confocal paraboloid,  $\Pi = \Lambda = 2$ , we have  $\Pi' = \Pi$  and  $\Lambda' = \Lambda$  by equations (C6) and (C8) for all inclinations, so its shape is unaffected by projection.

## APPENDIX D: ANALYTIC DERIVATION OF THIN-SHELL BOW SHAPE PARAMETERS

In this appendix, we provide analytic calculations of the planitude, alatitude, and asymptotic opening angle for the wilkinoid, cantoids, and ancantoids. We first consider the most general case of the ancantoids, and then show how results for cantoids and the wilkinoid follow as special cases.

### D1 Planitude of ancantoids

From equations (3) and (5), the planitude depends on the apex second derivative,  $R_{\theta\theta,0}$ , as

$$\Pi = (1 - R_{\theta\theta,0}/R_0)^{-1}. \quad (D1)$$

From equation (4), the second derivative can be found from the coefficient of  $\theta^2$  in the Taylor expansion of  $R(\theta)$ . Since we do not have  $R(\theta)$  in explicit analytic form, we proceed via a Taylor expansion of the implicit equations (60) and (61), retaining terms up to  $\theta^4$  to obtain from equation (61):

$$\theta_i^2 = \beta \theta^2 (1 + C_{k\beta} \theta^2) + \mathcal{O}(\theta^6), \quad (D2)$$

with the coefficient  $C_{k\beta}$  given by

$$C_{k\beta} = \frac{1}{15} - \frac{3k}{20} - \frac{\beta}{15}. \quad (D3)$$

Note that it is necessary to include the  $\theta^4$  term in the expansion of  $\theta_1^2$  so that  $\theta_1/\theta$  is accurate to order  $\theta^2$ . Then, from equation (60), we find

$$\begin{aligned} \frac{R}{D} &= \frac{\sin \theta_1}{\sin(\theta + \theta_1)} \\ &= \frac{\beta^{1/2}}{1 + \beta^{1/2}} \left\{ 1 + \theta^2 \left[ \frac{C_{k\beta}}{2(1 + \beta^{1/2})} + \frac{1}{6}(1 + 2\beta^{1/2}) \right] \right\} \\ &\quad + \mathcal{O}(\theta^4), \end{aligned} \quad (D4)$$

where in the second line we have carried out a Taylor expansion of the two sine terms and substituted equation (D2). Comparing coefficients of unity and  $\theta^2$  between equations (4) and (D4), we find

$$\frac{R_0}{D} = \frac{\beta^{1/2}}{1 + \beta^{1/2}} \quad (D5)$$

$$\frac{R_{\theta\theta,0}}{R_0} = \frac{C_{k\beta}}{1 + \beta^{1/2}} + \frac{1}{3}(1 + 2\beta^{1/2}), \quad (D6)$$

so that the final result for the planitude, from equation (D1), is

$$\text{ancantoid } \Pi = \left[ 1 - \frac{C_{k\beta}}{1 + \beta^{1/2}} - \frac{1}{3}(1 + 2\beta^{1/2}) \right]^{-1}. \quad (D7)$$

## D2 Alatitude of ancantoids

To find the alatitude,  $\Lambda = R_{90}/R_0$ , we use equation (60) at  $\theta = 90^\circ$  to write

$$\Lambda = \frac{D}{R_0} \tan \theta_{1,90}, \quad (D8)$$

where  $\theta_{1,90} = \theta_1(\theta = 90^\circ)$ , which, following equation (61), must satisfy

$$\theta_{1,90} \cot \theta_{1,90} = 1 - \frac{2\beta}{k+2}. \quad (D9)$$

Combining equations (D8) and (D9) with equation (D5) yields

$$\Lambda = \frac{(1 + \beta^{1/2})\theta_{1,90}}{\beta^{1/2}(1 - \xi_k \beta)}, \quad (D10)$$

where

$$\xi_k = \frac{2}{k+2}. \quad (D11)$$

We now take the Taylor expansion of equation (D9) to find

$$\theta_{1,90}^2 + \frac{1}{15}\theta_{1,90}^4 + \mathcal{O}(\theta_{1,90}^6) = 3\xi_k \beta, \quad (D12)$$

which, if  $\theta_{1,90}$  is small, has the approximate solution

$$\theta_{1,90} \approx \left( \frac{3\xi_k \beta}{1 + \frac{1}{5}\xi_k \beta} \right)^{1/2}. \quad (D13)$$

Substituting back into equation (D8) yields an approximate value for the alatitude of

$$\text{ancantoid } \Lambda \approx \frac{(3\xi_k)^{1/2}(1 + \beta^{1/2})}{(1 + \frac{1}{5}\xi_k \beta)^{1/2}(1 - \xi_k \beta)}. \quad (D14)$$

This approximation is surprisingly accurate, with a relative error of the order of 1 per cent even for  $\beta$  as large as 0.5 with  $k = 0$ .

## D3 Planitude and alatitude of cantoids and wilkinoid

Since  $\Pi$  and  $\Lambda$  depend on only that portion of the inner wind emitted in the forward hemisphere,  $\theta \leq 90^\circ$ , the results for the cantoids can be found by taking  $k = 0$ , in which case equations (D3), (D7), (D11), and (D14) yield

$$\text{cantoid } \begin{cases} \Pi = \frac{5}{3(1-\beta^{1/2})} \\ \Lambda = \frac{\sqrt{3}}{\left(1+\frac{1}{5}\beta\right)^{1/2}(1-\beta^{1/2})}. \end{cases} \quad (D15)$$

The wilkinoid shape is equal to the  $\beta \rightarrow 0$  limit of the cantoid, so its planitude and alatitude are given by

$$\text{wilkinoid } \begin{cases} \Pi = \frac{5}{3} \\ \Lambda = \sqrt{3}. \end{cases} \quad (D16)$$

The wilkinoid results can also be obtained directly from equation (52), and in the case of  $\Lambda$  this has already been noted by several authors (Cox et al. 2012; Meyer et al. 2016).

2795

2800

2810

## D4 Asymptotic opening angle

The asymptotic opening angle of the far wings,  $\theta_\infty$ , can be found from equation (61) for the ancantoids, together with the condition that  $\theta_\infty + \theta_{1\infty} = \pi$ . These yield the implicit equation

$$\theta_\infty - \left( \frac{k+2(1-\beta)}{k+2} \right) \tan \theta_\infty = \pi + 2\beta I_k(\pi/2), \quad (D17)$$

where

$$I_k(\pi/2) = \frac{\sqrt{\pi}}{4} \frac{\Gamma(\frac{k+1}{2})}{\Gamma(\frac{k+4}{2})} \quad (D18)$$

and  $\Gamma$  is the usual Gamma function. This can be compared with the equivalent result obtained by CRW for the cantoids:

$$\theta_\infty - \tan \theta_\infty = \frac{\pi}{1-\beta}. \quad (D19)$$

Note that, unlike in the cases of  $\Pi$  and  $\Lambda$ , equation (D17) does not reduce to equation (D19) in the limit  $k \rightarrow 0$ . This is because, for  $\theta > 90^\circ$ , the  $k = 0$  ancantoid differs from the cantoid since the former has no wind in the backward hemisphere (see Fig. 13). Therefore, there is less inner support for the far wings of the bow, and so  $\theta_\infty$  is smaller than in the cantoid case. The wilkinoid result again follows from  $\beta \rightarrow 0$ , implying that  $\theta_\infty = \pi$ , or, in other words, that the far wings are asymptotically parallel to the symmetry axis, as is the case for the paraboloid (Appendix C). In the case of the wilkinoid, however, the behaviour is cubic in the wings,  $z \sim r^3$ , as opposed to quadratic as in the paraboloid.

2830

2835

2840

## APPENDIX E: EMPIRICAL DETERMINATION OF RADIUS OF CURVATURE FOR A BOW SHOCK OF UNKNOWN ORIENTATION

Consider a set of  $N$  points on the plane of the sky,<sup>22</sup> with Cartesian coordinates  $\mathbf{r}_k = (x_k, y_k)$  for  $k = 1, \dots, N$ . We wish to estimate the radius of curvature of the smooth curve that the set of points is presumed to be sampled from. To do this, we fit a circle to the

2845

<sup>22</sup> In the main body of the paper, the prime symbol ('') is used to distinguish projected from ‘true’ quantities. In this appendix, for simplicity, we omit the primes since all quantities are projected.

2850

points as follows. The circle is defined by its centre,  $\mathbf{r}_c = (x_c, y_c)$ , and radius,  $R_c$ . For a given circle, we define a mean radius of the set of points from the circle centre:

$$2857 \quad \bar{R}_c(x_c, y_c) = \frac{1}{N} \sum_{k=1}^N |\mathbf{r}_k - \mathbf{r}_c|. \quad (\text{E1})$$

We then optimize to find best-fitting values  $(x_c^*, y_c^*)$ , which minimize the objective function

$$2862 \quad f(x_c, y_c) = \sum_{k=1}^N (|\mathbf{r}_k - \mathbf{r}_c| - \bar{R}_c(x_c, y_c))^2. \quad (\text{E2})$$

The best-fitting radius of curvature is then given by  $R_c^* = \bar{R}_c(x_c^*, y_c^*)$ .

2867 If we also know the position,  $\mathbf{r}_0 = (x_0, y_0)$ , of the bow's central source, then we can find the unit vector in the direction of the bow's projected axis as

$$2872 \quad \hat{\xi} = \frac{\mathbf{r}_0 - \mathbf{r}_c^*}{|\mathbf{r}_0 - \mathbf{r}_c^*|}, \quad (\text{E3})$$

and the apex distance from the source as<sup>23</sup>

$$2877 \quad R_0 = |\mathbf{r}_c^* + R_c^* \hat{\xi} - \mathbf{r}_0|. \quad (\text{E4})$$

A refinement of the method is then to iteratively repeat the circle fit after restricting the set of points to those lying within a certain angle  $\Delta\theta$  of the bow axis, where we find that best results are obtained with  $\Delta\theta \approx 60^\circ\text{--}75^\circ$ . That is,

$$2882 \quad |\theta_k| < \Delta\theta, \quad (\text{E5})$$

where the signed angle  $\theta_k$  of each point from the axis,<sup>24</sup> measured at the source position  $\mathbf{r}_0$ , can be calculated as

$$2887 \quad \theta_k = \arctan \left[ \frac{(\mathbf{r}_k - \mathbf{r}_0) \cdot \hat{\xi}^\perp}{(\mathbf{r}_k - \mathbf{r}_0) \cdot \hat{\xi}} \right]. \quad (\text{E6})$$

<sup>23</sup> This is only valid if the resultant  $R_0 < R_c^*$ , otherwise the opposite sign of  $\hat{\xi}$  must be taken.

<sup>24</sup> Although the sign of  $\theta_k$  is not relevant to equation (E5), it is used below in calculating the perpendicular radii.

In the preceding equation, the ‘perpendicular’ operator ( $\perp$ ) rotates its vector argument anticlockwise by  $90^\circ$ , so that  $(x, y)^\perp = (-y, x)$ .

Two or three iterations are sufficient for convergence in most cases, although in some cases it is possible that the process will converge to a stable flip-flop oscillation between two different solutions. This is due to the dependence of the  $\theta_k$ , via  $\hat{\xi}$ , on the  $\mathbf{r}_c^*$  of the previous iteration, which can lead to points entering and leaving the fitted set. We have not found this to be a serious problem in practice, since the two solutions tend to be very close to one another. It could be mitigated by averaging  $\mathbf{r}_c^*$  over two previous iterations. The alternative of measuring the angle with respect to the centre of curvature,  $\mathbf{r}_c^*$ , instead of the source,  $\mathbf{r}_0$ , is found to be much less stable.

If quantitative estimates exist for the uncertainties,  $\epsilon_k$ , in the measurements of  $\mathbf{r}_k$ , then it is appropriate to incorporate weights of  $\epsilon_k^{-2}$  in the objective function. However, it is rare for the  $\epsilon_k$  to be objectively quantifiable, since the uncertainties are often systematic and/or subjective. In the cases where the bow shape is traced by eye, based on real or synthetic observations, a more practical approach is to maintain uniform weighting but to place a greater density of points  $\mathbf{r}_k$  in regions where the shape is well determined and to place them more sparsely in regions where the shape is less certain.

Since there is no guarantee of symmetry about the axis  $\hat{\xi}$ , the perpendicular radius will in general be different in the two wings of the bow, with values  $R_{90+}$  and  $R_{90-}$ . These can be estimated by defining

$$R_k = |\mathbf{r}_k - \mathbf{r}_0| \quad (\text{E7})$$

and linearly interpolating between the points  $(\theta_k, R_k)$  at  $\theta = \pm 90^\circ$ .

Our PYTHON language implementation of this algorithm is freely available at <https://github.com/div-B>equals-0/circle-fit>. An example application to real data is given in Section 7 and Fig. 28. Note that this method is not necessary if the orientation of the bow axis is known a priori, in which case the Taylor series method described in Section 2 is more efficient and accurate.

2862  
2867  
2872  
2877

2919

2924

2934

2939

2944

2949

2897

2954

2902

2964

2907

2969

2912

2974

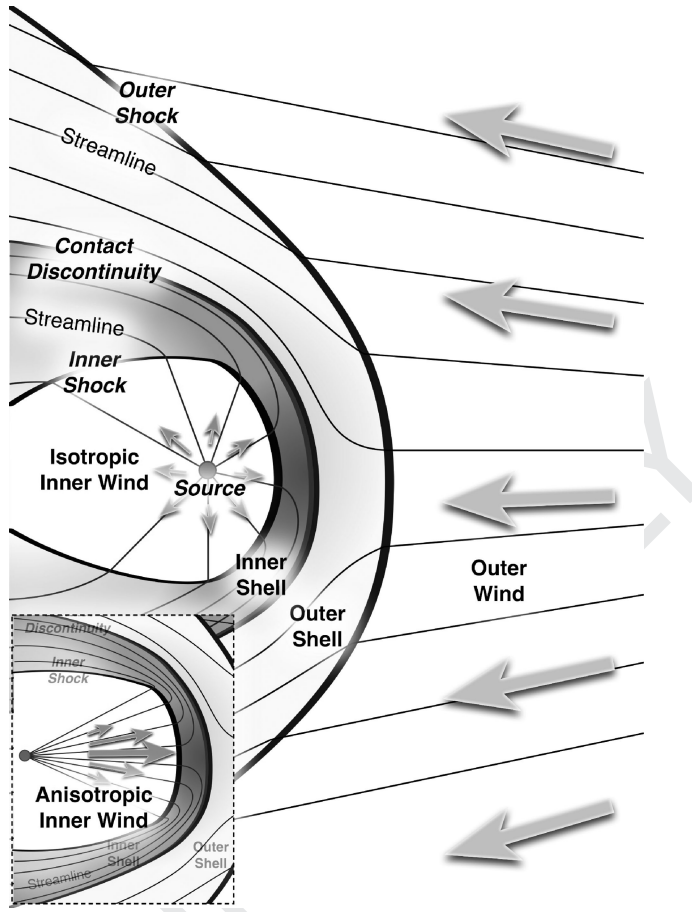


**Figure 2.** Quasi-stationary bow shock structure formed by the interaction of two supersonic winds. Lower-left inset box shows the case where the inner wind is anisotropic. The streamlines (thin lines) are drawn to be qualitatively realistic: they are straight in regions of hypersonic flow, but curved in subsonic regions, responding to pressure gradients in the shocked shells. Streamline slopes are discontinuous across oblique shocks.

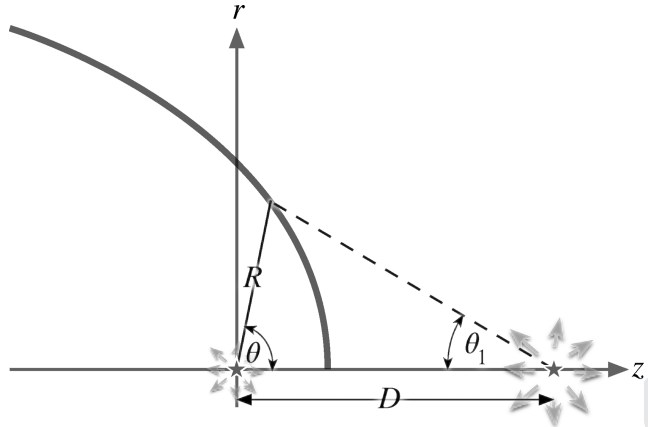


**Figure 3.** Schematic diagram of cylindrically symmetric two-wind interaction problem in the thin-shell limit, following Canto, Raga & Wilkin (1996).

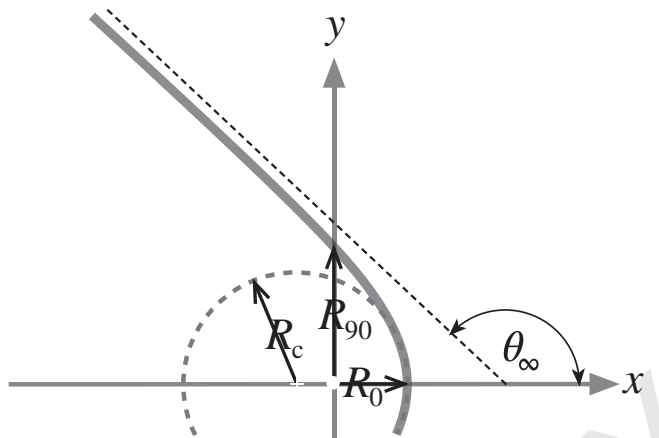


**Figure 4.** Parameters for characterizing a bow shape. Bow radius from the star, measured parallel ( $R_0$ ) and perpendicular ( $R_{90}$ ) to the symmetry axis, together with radius of curvature ( $R_c$ ) at apex and asymptotic opening angle ( $\theta_\infty$ ) of the far wings.

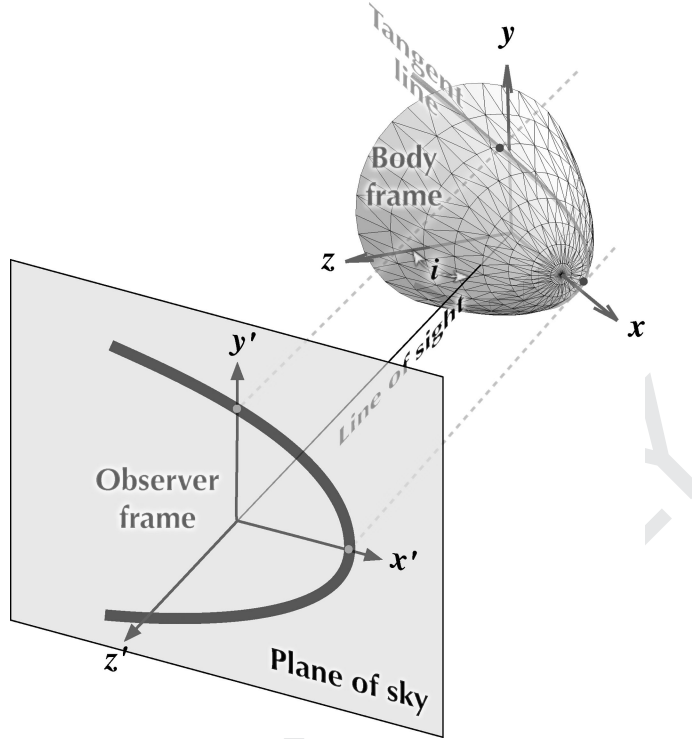


**Figure 5.** Relationship between body frame (unprimed coordinates) and observer frame (primed coordinates). Note that the plane of the sky is a projective plane, not a geometric plane in Euclidean 3-space, see discussion in the text.

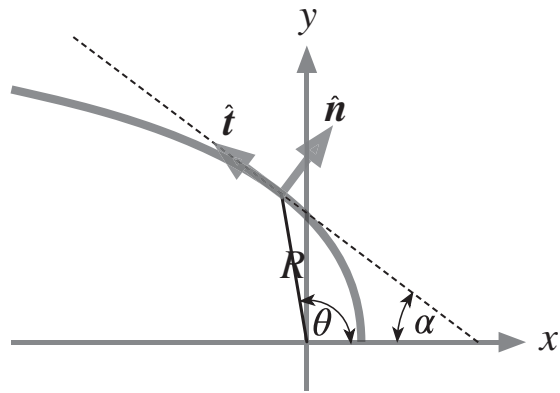
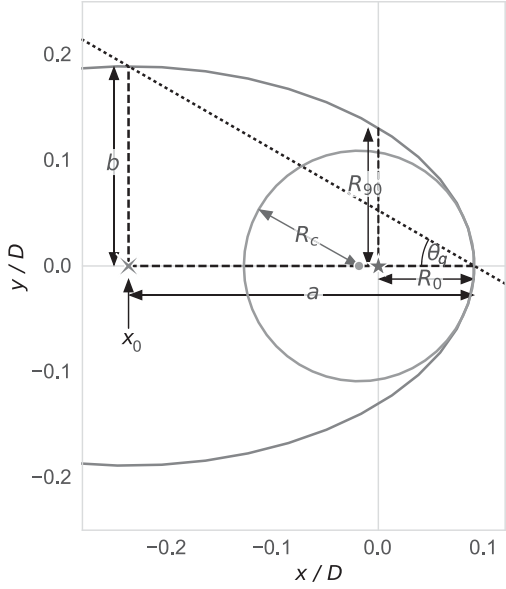


**Figure 6.** Unit vectors in the body frame that are normal and tangential to the surface  $R(\theta)$  in a plane of constant azimuth,  $\phi$ .

(a)



(b)

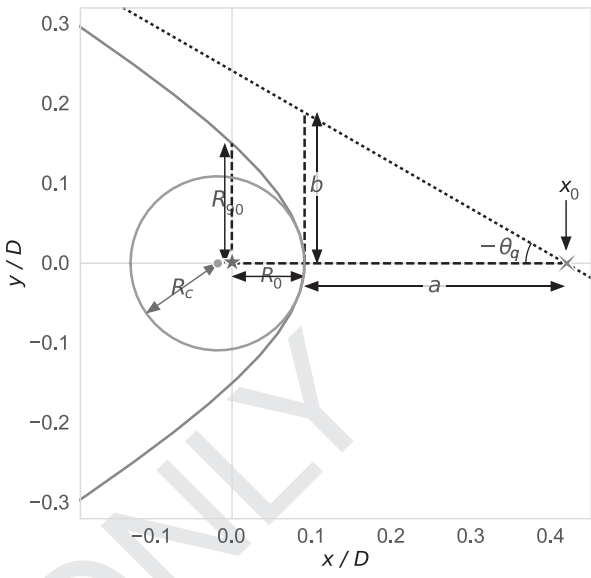


**Figure 7.** Example off-centre conic sections that can form quadrics of revolution: (a) ellipse, (b) hyperbola. The relationship is shown between the conic section parameters  $a$ ,  $b$ ,  $\theta_Q$  and the bow shock characteristic radii  $R_0$ ,  $R_{90}$ ,  $R_c$ , as defined in Fig. 4. The origin (centre of the weaker flow) is indicated by a red star, the centre of curvature of the apex of the bow shock is indicated by a green dot, and the geometric centre of the conic section is indicated by a blue cross, which is offset by  $x_0$  from the origin. Note that  $R_0$ ,  $R_{90}$ ,  $R_c$ ,  $a$ , and  $b$  are all *lengths* and are always positive, whereas  $x_0$  is a *displacement* and may be positive or negative.

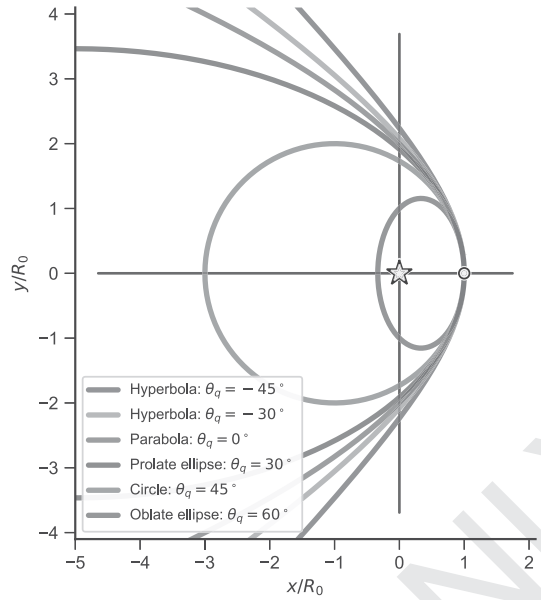


**Figure 8.** Example of a family of conic sections, all with the same planitude (flatness at apex, marked by white dot):  $\Pi = R_c/R_0 = 2$ . The quadric angle,  $\theta_Q$ , varies over the family (see the text), with lower values of  $\theta_Q$  giving larger values of the alatitude,  $\Lambda = R_{90}/R_0$ , meaning more open wings. Different values of  $\Pi$  can be achieved for the exact same quadrics by sliding them along the  $x$ -axis, which will also change the axis scales since these are normalized by  $R_0$ .

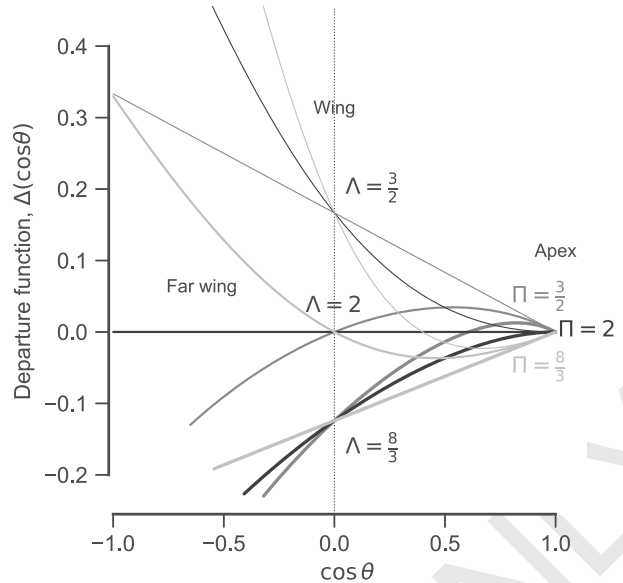


**Figure 9.** Parabolic departure function,  $\Delta(\cos \theta)$ , for conic sections with different planitude and alatitude, centred on that of the confocal parabola,  $(\Pi, \Lambda) = (2, 2)$ , which has  $\Delta(\cos \theta) = 0$ . Planitude (shown by different line colours) determines the slope of  $\Delta$  at the apex,  $\cos \theta = 1$ . Alatitude (shown by different line widths) determines the value of  $\Delta$  at  $\cos \theta = 0$ . All conics with  $\Pi = \Lambda$  have departure functions that are straight lines.

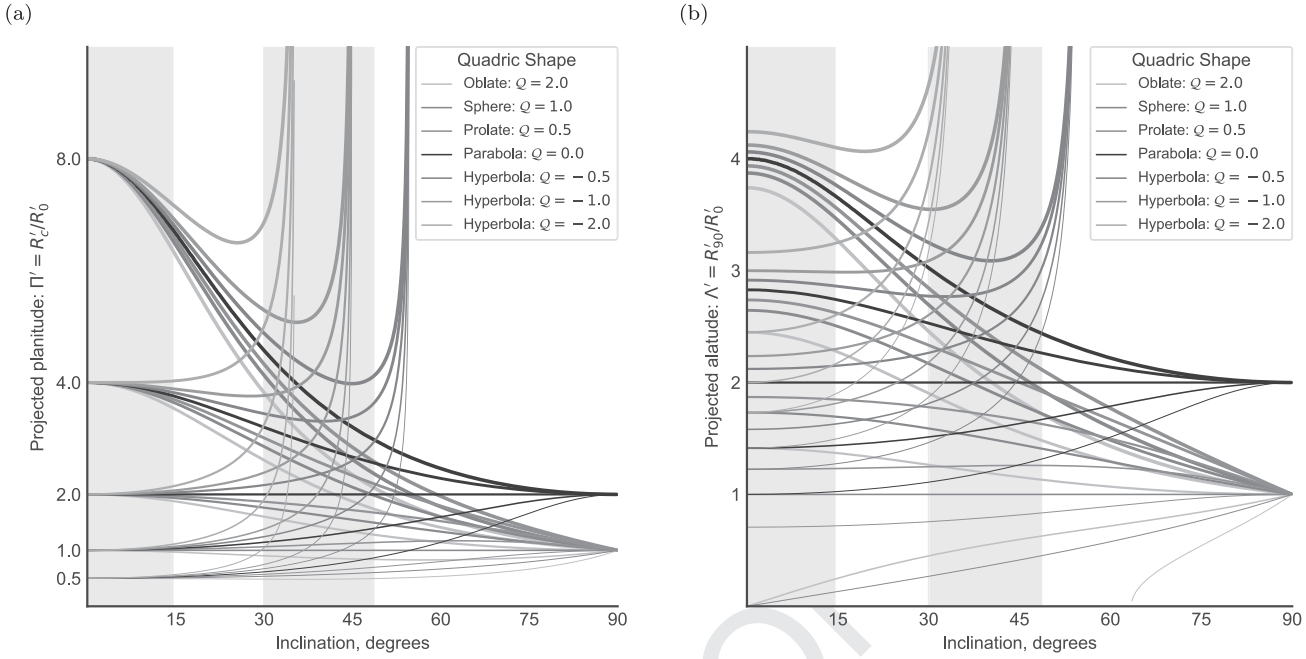
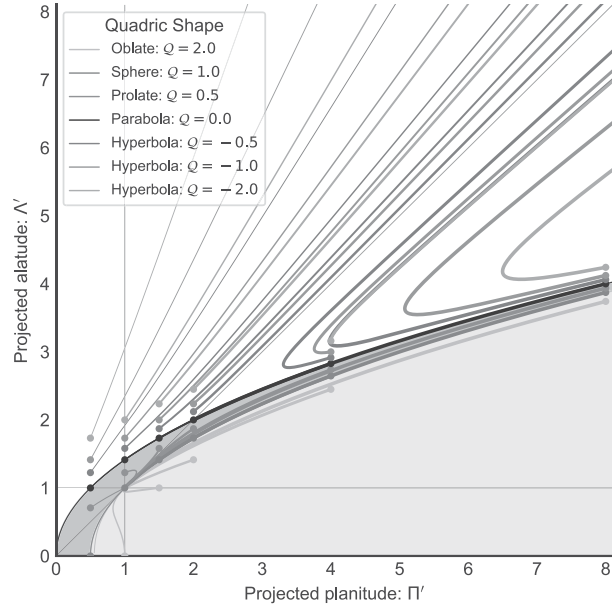


**Figure 10.** Effects of projection on quadrics of revolution: variation with inclination,  $|i|$ , of bow size and shape. Different line colours correspond to varying quadric parameter,  $Q$  (see key), while variation in line width corresponds to variation in the ‘true’ planitude,  $\Pi$ , or apex radius of curvature. Vertical grey rectangles show quartiles of  $|\sin i|$ , which will be equally populated for an isotropic distribution of orientations. (a) Projected planitude:  $\Pi'$ . (b) Projected alatitude,  $\Lambda'$ .

(a)



(b)

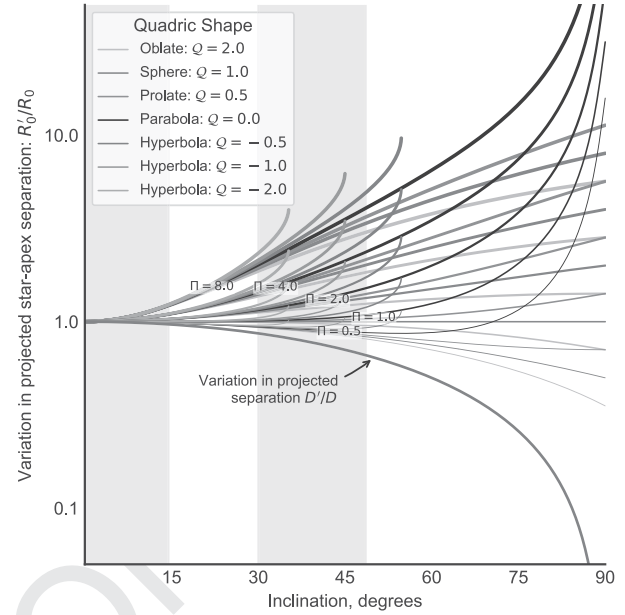


**Figure 11.** As Fig. 10, but (a) diagnostic planitude–alatitude diagram:  $\Lambda'$  versus  $\Pi'$ , and (b) projected/true star–apex distance:  $R_0'/R_0$  versus  $|i|$ . In panel (a), shading indicates different classes of quadrics: hyperboloids (white), prolate spheroids (dark grey), and oblate spheroids (light grey), with the limiting case of paraboloids shown by the thin black line.

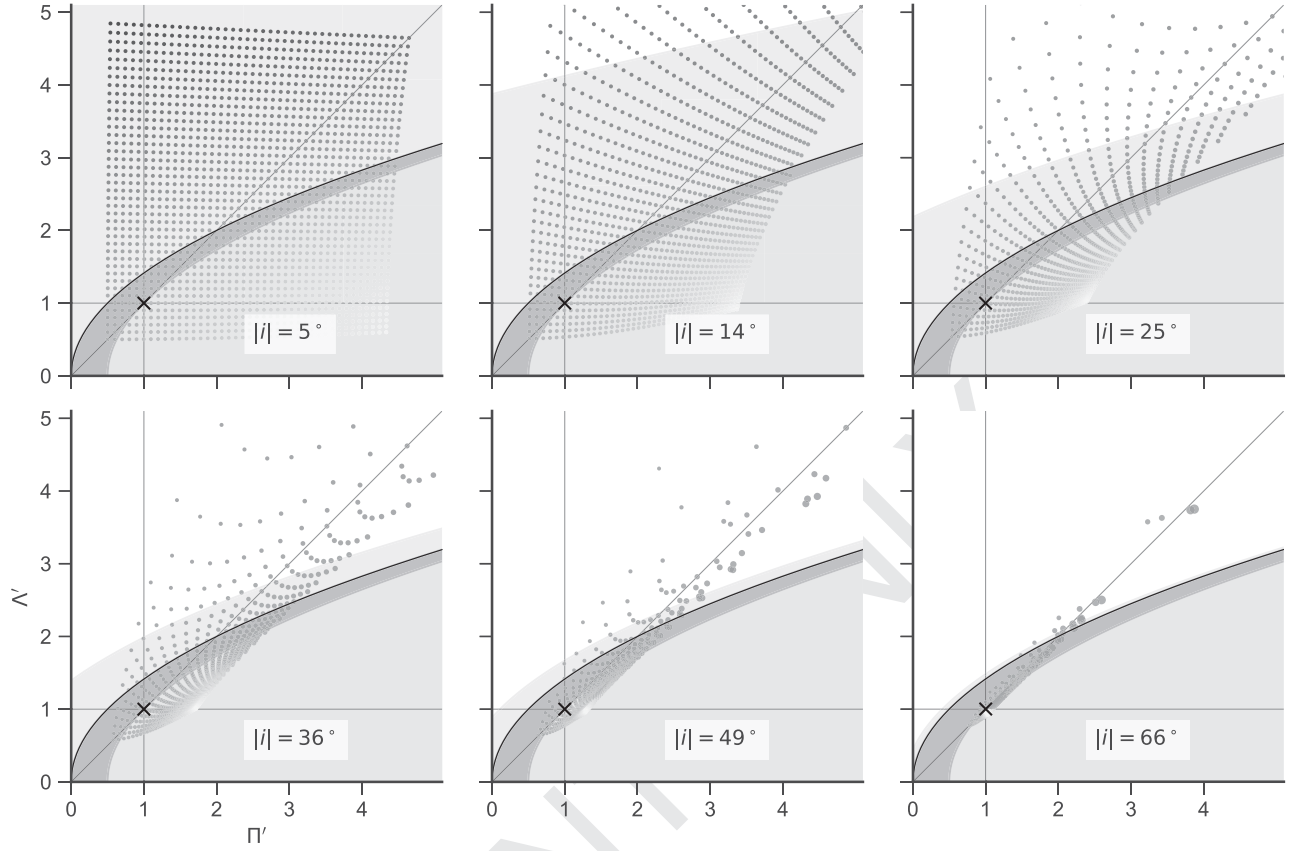


**Figure 12.** Variation with inclination angle of the apparent shape of quadric bows with true planitude and alatitude that are uniformly distributed over the ranges  $\Pi = [0.5, 4.5]$ ,  $\Lambda = [0.5, 4.5]$ . Panels show the apparent  $(\Pi', \Lambda')$  as the inclination is increased through uniform intervals in  $|\sin i|$ . Symbol colour represents the quadric parameter,  $\mathcal{Q}$ , increasing from dark blue, through orange, to yellow. Symbol size is proportional to the increase in apparent star–apex distance,  $R'_0/R_0$ .

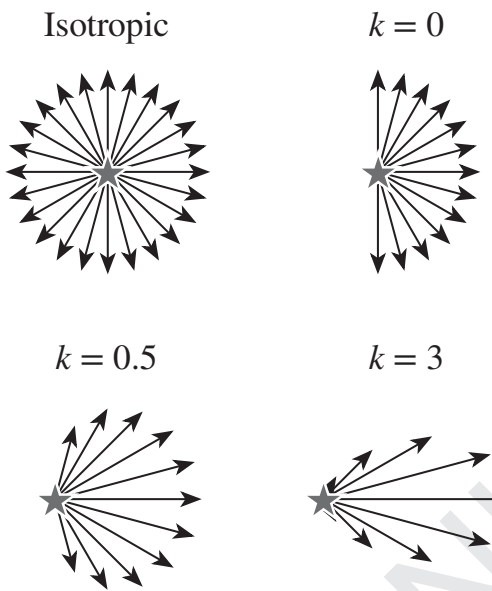


**Figure 13.** Schematic diagram of wind flow patterns in isotropic and non-isotropic cases for different values of the anisotropy index,  $k$ . Arrow length represents the wind momentum loss rate per solid angle.

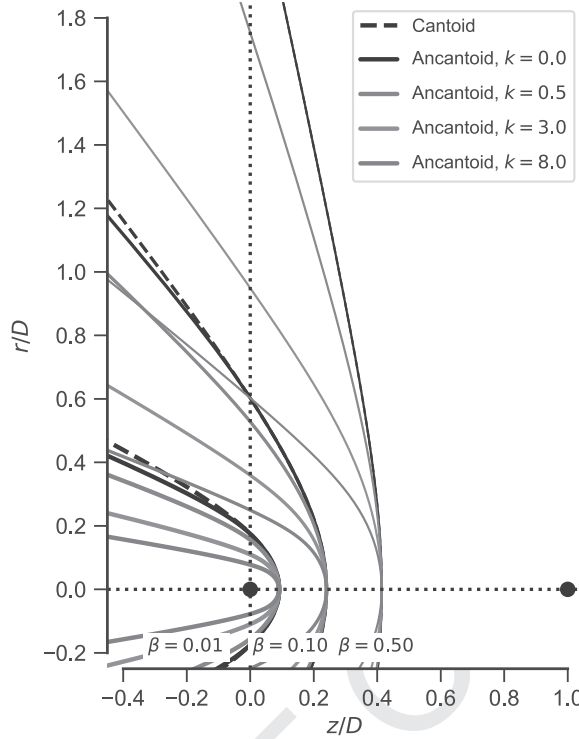


**Figure 14.** Bow shock shapes for interacting winds in the thin-shell approximation: cantoids and ancantoids. Coordinates are normalized by  $D$ , the distance between the two wind sources, which are indicated by black dots on the axis. The weaker source is at  $(0.0, 0.0)$  and the stronger source is at  $(1.0, 0.0)$ . Results are shown for different values of the wind momentum ratio,  $\beta$  (different line widths), and for the case where the weaker wind is isotropic (black lines) or anisotropic (coloured lines).

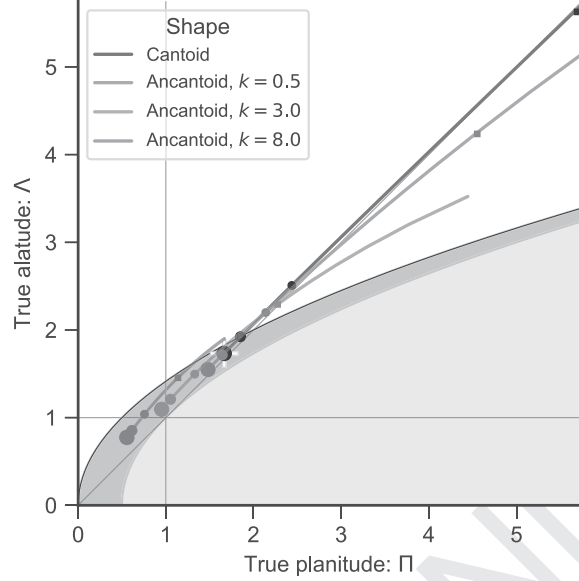


**Figure 15.** True shapes of cantoids and ancantoids in the  $\Pi$ - $\Lambda$  plane, calculated according to results of Appendix D. For each line,  $\beta$  varies over the range [0, 1] from lower left to upper right (although the black and red lines are truncated on the upper right), and line colours correspond to different anisotropy indices, matching those used in Fig. 14. Circle symbols mark particular  $\beta$  values: 0, 0.01, 0.1, from largest to smallest circle. Square symbols mark  $\beta = 0.5$ , but with  $\Lambda$  calculated exactly, instead of using the approximation of equation (D14). The white plus symbol marks the result for the wilkinoid:  $(\Pi, \Lambda) = (\frac{5}{3}, \sqrt{3})$ . Background shading indicates the domains of different quadric classes: hyperboloids (white), prolate spheroids (dark grey), and oblate spheroids (light grey).

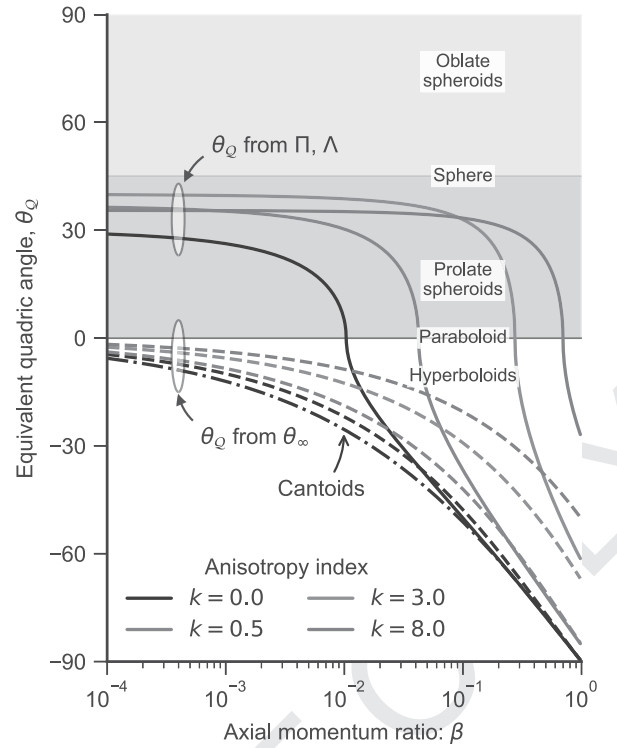
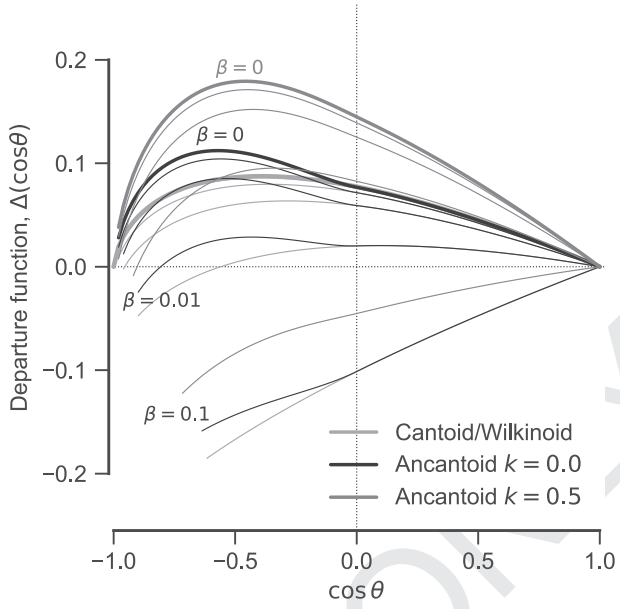


**Figure 16.** Equivalent quadric angles,  $\theta_Q$ , for ancantoids and cantoids. Solid lines show values of  $\theta_Q$  calculated from  $(\Pi, \Lambda)$ , which is representative of the shape of the head, while dashed lines show  $\theta_Q$  calculated from  $\theta_\infty$ , which is representative of the tail. Dot-dashed line shows the result for cantoids, which differ from the  $k = 0$  ancantoids in  $\theta_\infty$ , but not in  $(\Pi, \Lambda)$ . Grey shading and line colours have the same meaning as in Fig. 15.

(a)



(b)

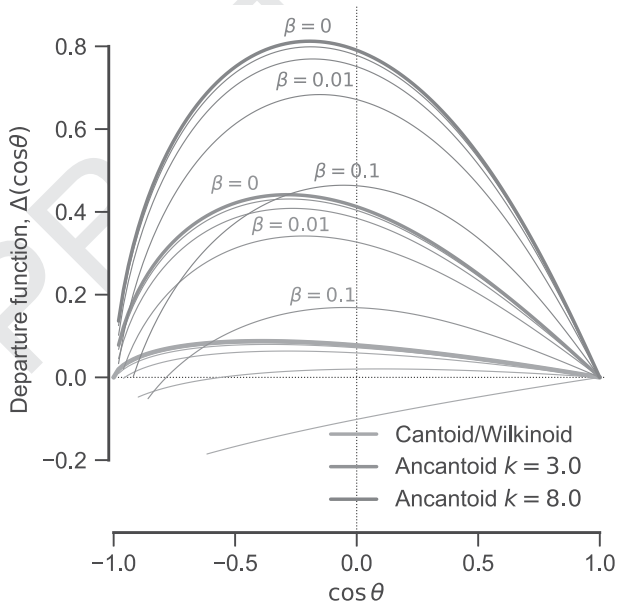


**Figure 17.** Parabolic departure function,  $\Delta(\cos\theta)$ , for ancantoids and cantoids. Heavy lines show the  $\beta = 0$  parallel-stream case (wilkinoid in the isotropic case). Light lines show increasing values of  $\beta = 10^{-4}, 0.001, 0.01, 0.1$ , as marked. (a) Cantoids (grey) and moderately anisotropic ancantoids: hemispheric,  $k = 0$  (black), and prolyd-like,  $k = 0.5$  (red). (b) Cantoids (grey) and extremely anisotropic, jet-like ancantoids:  $k = 3$  (purple) and  $k = 8$  (blue).

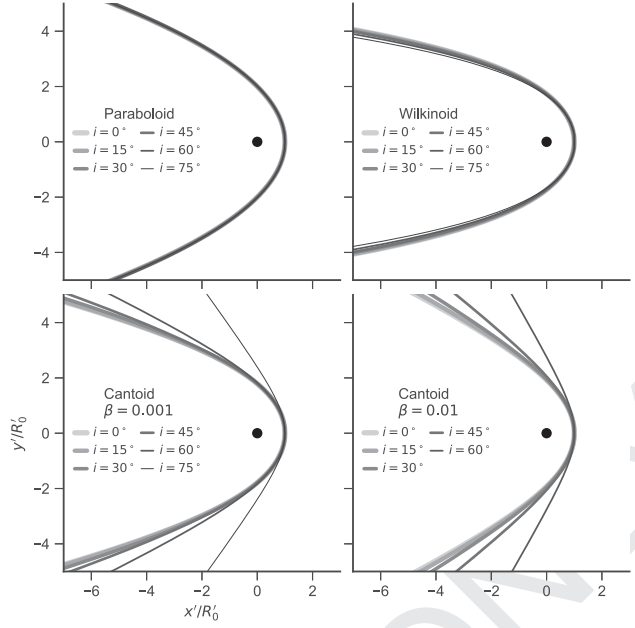


**Figure 18.** Apparent bow shapes as a function of inclination angle for isotropic thin-shell models. (a) Confocal paraboloid for comparison (shape independent of inclination). (b) Wilkinoid. (c) Cantoid,  $\beta = 0.001$ . (d) Cantoid,  $\beta = 0.01$ .

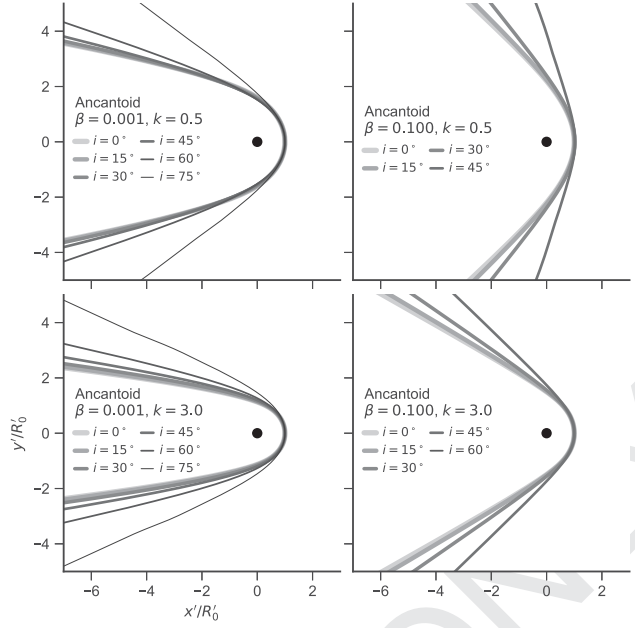
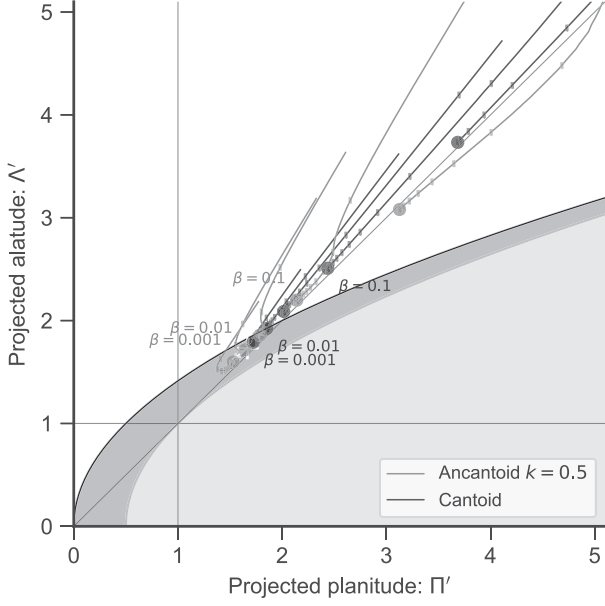


**Figure 19.** Further apparent bow shapes as a function of inclination angle for anisotropic thin-shell models (ancantoids). (a)  $\beta = 0.001, k = 0.5$ ; (b)  $\beta = 0.1, k = 0.5$ ; (c)  $\beta = 0.001, k = 3$ ; (d)  $\beta = 0.1, k = 3$ .

(a)



(b)

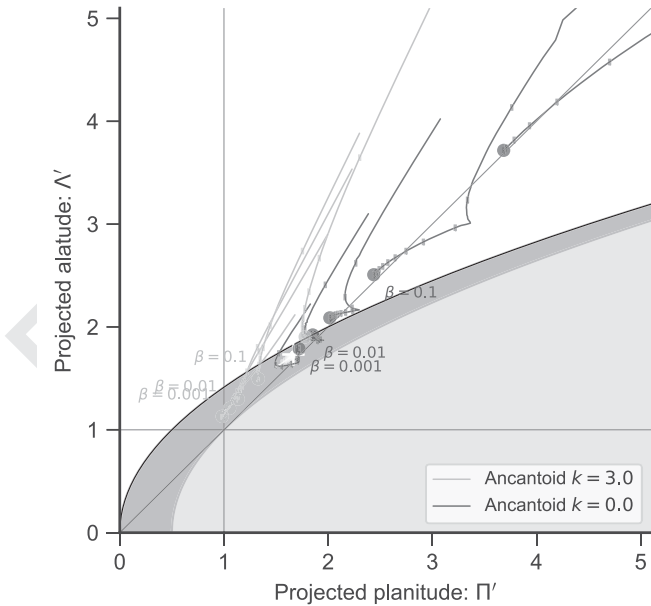


**Figure 20.** Apparent projected shapes of wilkinoid, cantoids, and ancantoids in the  $\Pi'$ – $\Lambda'$  plane. Coloured symbols indicate the  $|i| = 0$  position for  $\beta = 0.001, 0.003, 0.01, 0.03, 0.1, 0.3$ . Thin lines show the inclination-dependent tracks of each model, with tick marks along each track for 20 equally spaced values of  $|\sin i|$ . Grey shaded regions are as in Fig. 11(a). The wilkinoid track is shown in white. (a) Isotropic wind model (cantoid) and proplyd-like model (ancantoid,  $k = 0.5$ ). (b) Hemispheric wind model (ancantoid,  $k = 0$ ) and jet-like model (ancantoid,  $k = 3$ ).

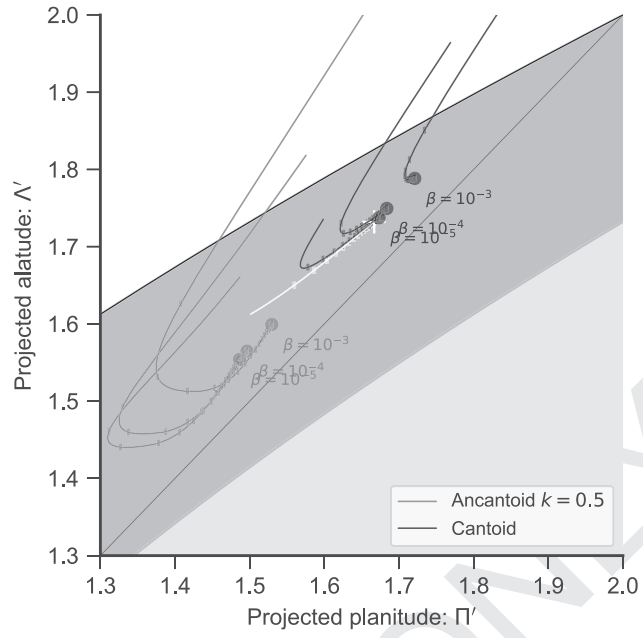


**Figure 21.** As Fig. 20(a) but zoomed in to show the wilkinoid track (white) and the convergence of the cantoid tracks (purple) to the wilkinoid as  $\beta \rightarrow 0$ .

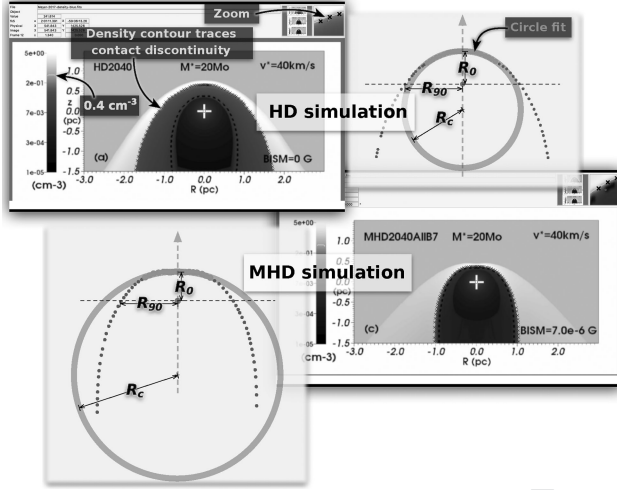
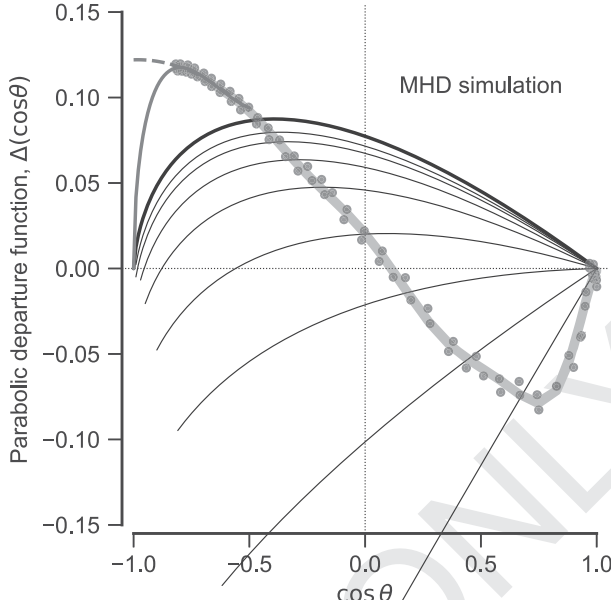


**Figure 22.** Procedure for tracing the contact discontinuity from the Meyer et al. (2017) simulations. The density maps from Meyer et al.’s fig. 3 are converted to FITS format and displayed using the software SAOIMAGE DS9 (Joye & Mandel 2003). The density contour at  $0.4 \text{ cm}^{-3}$  is displayed (shown in green in the figure), and this is traced by hand by placing ‘point regions’ on the image (shown by black ‘x’ shapes in the figure). The zoom facility of the software allows the points to be placed with any required accuracy. The points are saved to a file in the DS9 region file format, which is then read by PYTHON programs for further processing. For example, the yellow boxes show circle fits and determination of the parameters  $R_0$ ,  $R_c$ , and  $R_{90}$ . In this example, only the points shown in orange (within  $60^\circ$  of axis) are used in the fits.

(a)



(b)

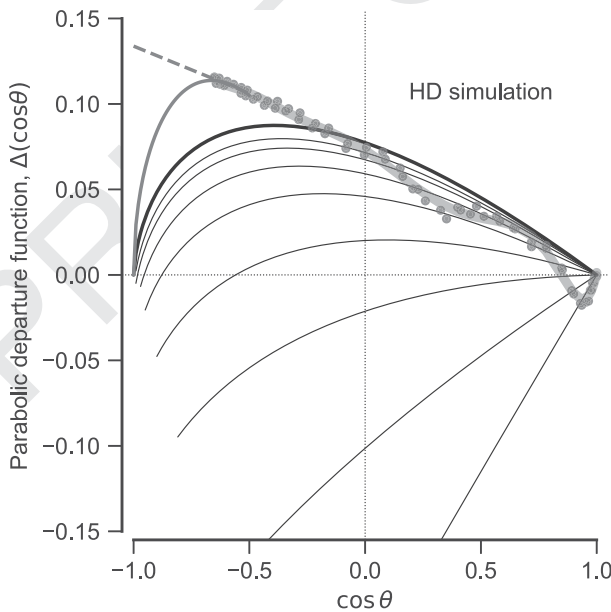


**Figure 23.** Departure function for the shape of the contact discontinuity, measured from two numerical simulations of a  $20 M_{\odot}$  main-sequence star, moving at  $40 \text{ km s}^{-1}$  through a uniform medium of density  $0.57 \text{ cm}^{-3}$  (Meyer et al. 2017). (a) MHD simulation with ambient magnetic field of strength  $7 \mu\text{G}$ , oriented parallel to the stellar velocity. (b) Hydrodynamic simulation with zero magnetic field. Blue dots show the measured shape, while the thick, pale-red line shows a 12th-order Chebyshev polynomial fit. The published shapes only extend to  $\theta \approx 130^\circ\text{--}150^\circ$ , so we extrapolate the shapes out to  $\theta = 180^\circ$ . Two different extrapolations are shown, corresponding to bows that are asymptotically closed (dashed red line) or open (solid red line). For comparison, black lines show the departure function for wilkinoids (thick line) and cantoids (thin lines).

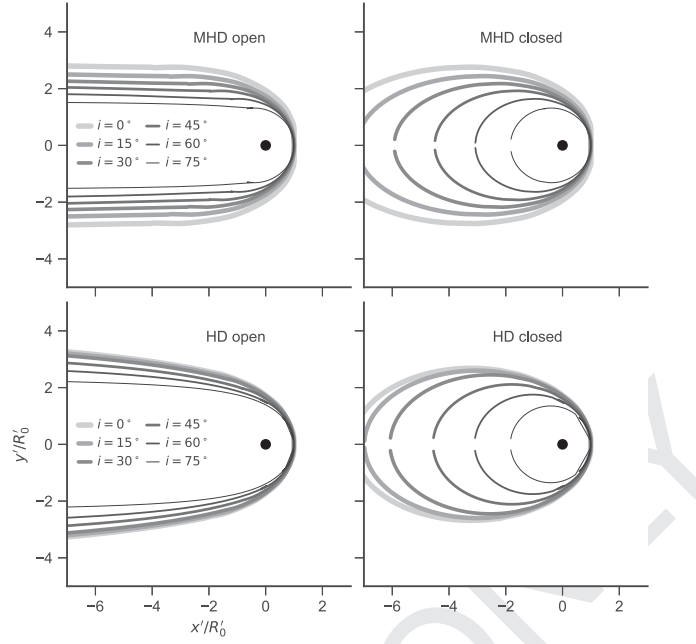


**Figure 24.** Projected shapes of contact discontinuity from simulations at different inclinations  $|i|$  (varying line colour and thickness, see key). The top row shows magnetized simulation of Fig. 23(a), and the bottom row shows non-magnetized simulation of Fig. 23(b). The left column shows asymptotically open extrapolation, and the right column shows asymptotically closed extrapolation. All shapes are normalized to the projected apex distance,  $R'_0$ .

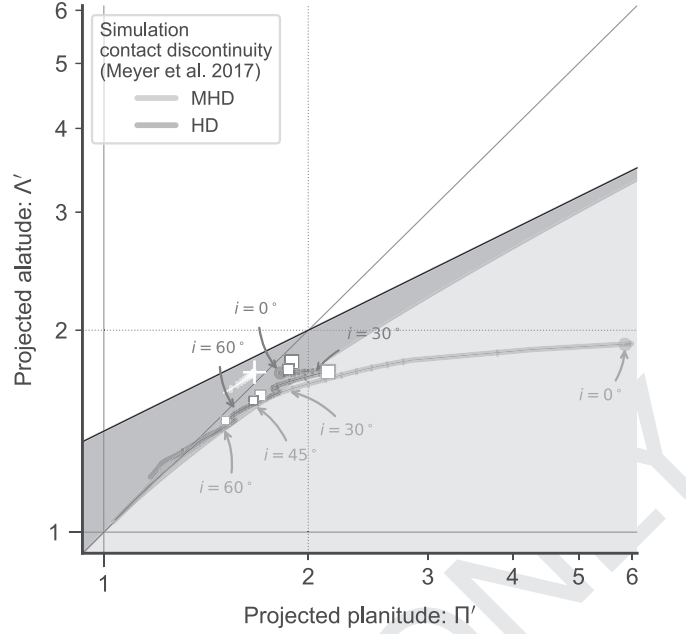


**Figure 25.** Apparent projected shapes of simulations in the  $\Pi' - \Lambda'$  plane. Thick solid lines show the predicted inclination-dependent tracks of the traced contact discontinuity shape for the asymptotically open extrapolation, with tick marks indicating 20 equal intervals in  $|\sin i|$ . Thin solid lines show the same for the asymptotically closed extrapolation, which only deviates from the open case at the high- $|i|$  end of the HD tracks. The true planitude and alatitude are marked by filled circle symbols. Open square symbols show the shapes traced from the dust emission maps at 60  $\mu\text{m}$  for inclinations of (largest to smallest) 30°, 45°, and 60°. For comparison, the wilkinoid track is shown in white. Note that the scales of both axes are logarithmic in this case.

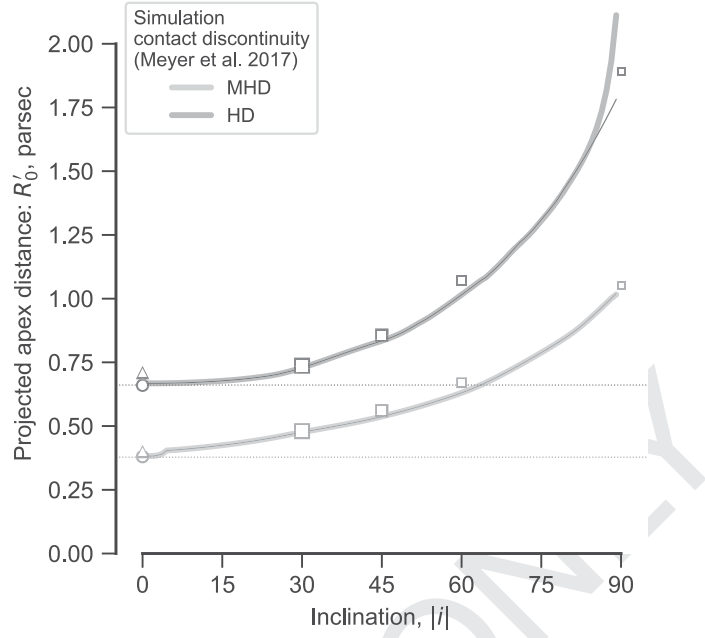


**Figure 26.** Apparent projected apex distance of simulations. Line and symbol meanings are as in Fig. 25. In addition, triangle symbols at  $|i| = 0^\circ$  denote radius measured on H $\alpha$  optical emission maps. Note that the distances for the blue square symbols have been adjusted according to the correction factor discussed in footnote 14.

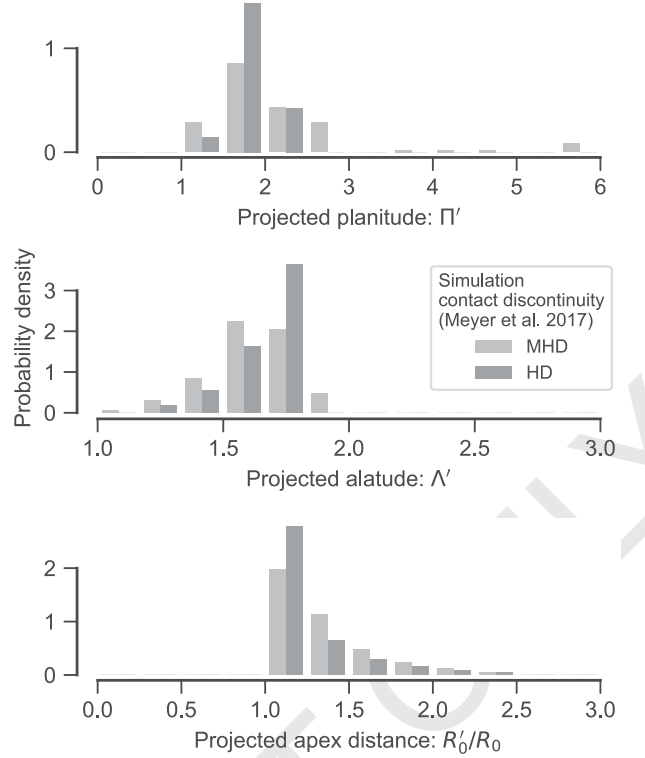


**Figure 27.** Histograms of (top to bottom) projected planitude, alatitude, and bow shock size for the shape of the contact discontinuity in the Meyer et al. (2017) simulations. The y-axis gives the probability density (per unit x-axis quantity), assuming a uniform distribution of viewing directions.

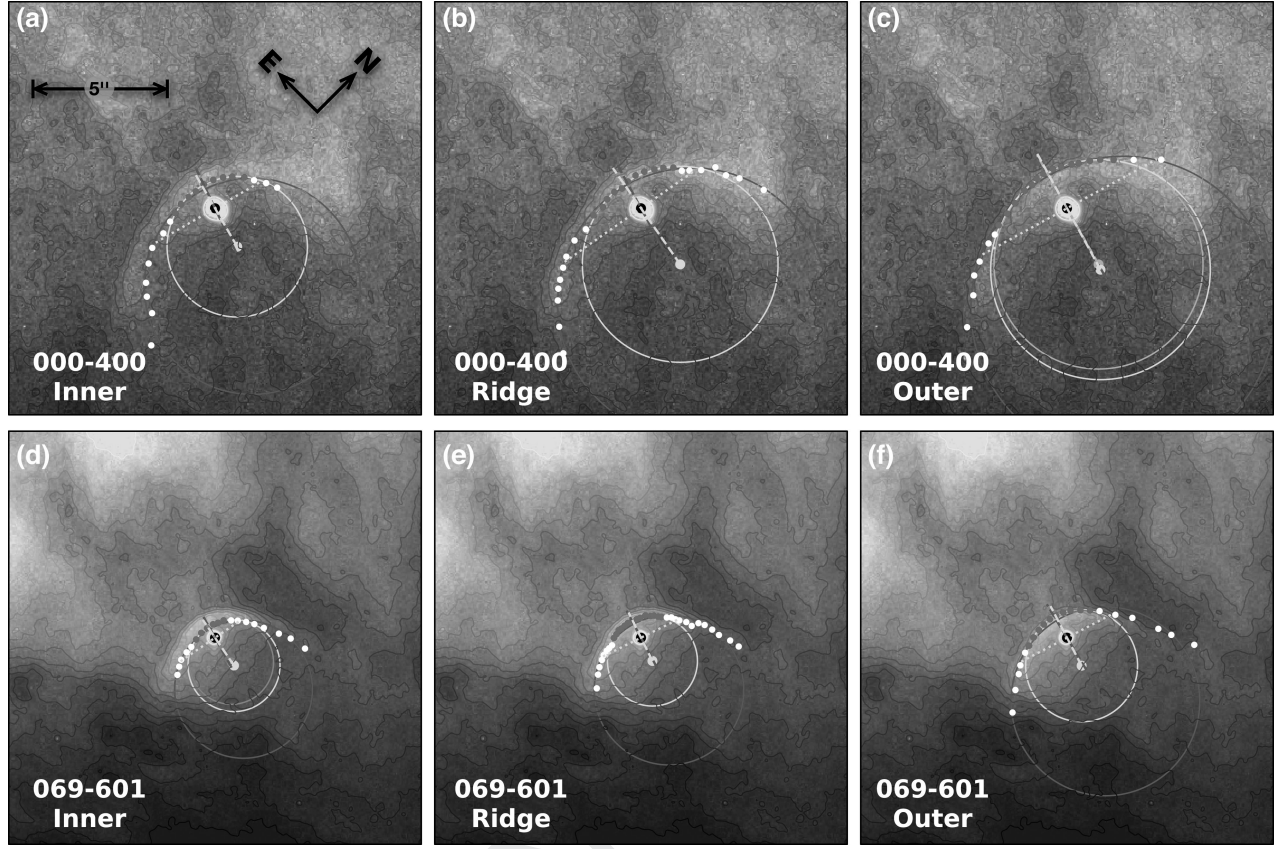


**Figure 28.** Example empirical determination of planitude and alatitude for observed bow shocks associated with proplyds in the outer Orion nebula (M42). Colour scale and contours show a *Hubble Space Telescope* H $\alpha$  image (ACS F658N filter; Bally et al. 2006) of M42 000-400 (panels a–c) and M42 069-601 (panels d–f). The image scale and orientation are indicated in panel (a) and are the same for all panels. Three different bows have been traced by eye on each object (red and white filled symbols): (a, d) inner edge, (b, e) ridge of maximum emission, and (c, f) outer edge. For each panel, the dark-coloured circle shows the initial fit to the full set of points (white and red), using the algorithm described in Appendix E. The centre of curvature and derived axis are shown by a small filled circle and dashed line in the same colour. Lighter coloured circles show three subsequent iterations where the fit is restricted to points within  $\pm\Delta\theta = 75^\circ$  of the axis. The subset of points used in the final iteration is marked in red. The perpendicular radii for the final iteration are shown by dotted lines. In panels (a), (b), and (d)–(f), the iterations converge immediately, but in panel (c) the iterations stably oscillate between two slightly different solutions.

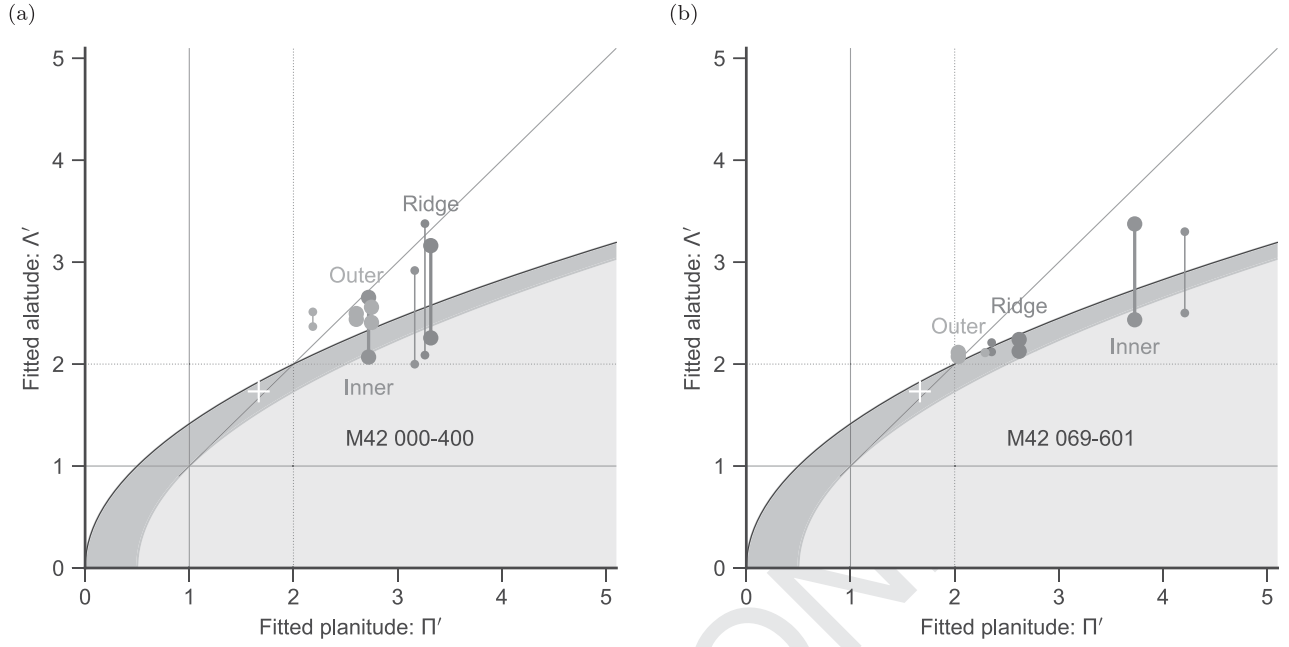


**Figure 29.** Location in the projected planitude–alatitude plane of the converged circle fits to the M42 bows: (a) 000-400, (b) 069-601. For each solution, the two values of the projected alatitude,  $\Lambda'_+$  and  $\Lambda'_-$ , corresponding to  $R_{90+}$  and  $R_{90-}$ , are joined by a vertical line. Large symbols show the results from the fits shown in Fig. 28, while small symbols show results for fits using  $\Delta\theta = 60^\circ$  instead of  $75^\circ$ . In panel (a), two slightly different  $\Pi'$  values are shown for the outer bow, since the fit does not converge to a single value [see Fig. 28(c) and Appendix E].

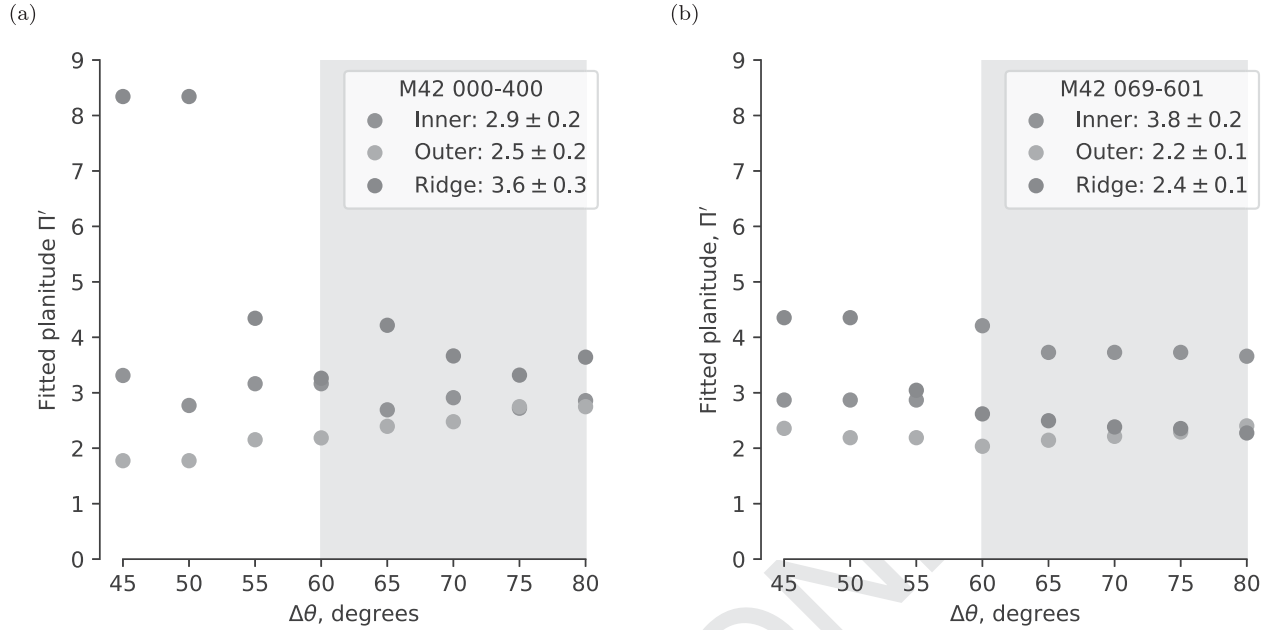


**Figure 30.** Variation of fitted planitude,  $\Pi'$ , as a function of the parameter  $\Delta\theta$ , which controls how close a point must be to the axis in order to be included in the circle fit. (a) M42 000-400, (b) M42 069-601. For the three traced bows (inner, outer, and ridge) of each object, the symbol key lists the mean and standard deviation of  $\Pi'$ , calculated over the ‘stable’ range  $\Delta\theta = 60^\circ–80^\circ$ , which is indicated by light grey shading.

# List of astronomical key words (Updated on 2017 March)

This list is common to *Monthly Notices of the Royal Astronomical Society*, *Astronomy and Astrophysics*, and *The Astrophysical Journal*. In order to ease the search, the key words are subdivided into broad categories. No more than six subcategories altogether should be listed for a paper.

The subcategories in boldface containing the word ‘individual’ are intended for use with specific astronomical objects; these should never be used alone, but always in combination with the most common names for the astronomical objects in question. Note that each object counts as one subcategory within the allowed limit of six.

The parts of the key words in italics are for reference only and should be omitted when the keywords are entered on the manuscript.

## General

editorials, notices  
errata, addenda  
extraterrestrial intelligence  
history and philosophy of astronomy  
miscellaneous  
obituaries, biographies  
publications, bibliography  
sociology of astronomy  
standards

radiation: dynamics  
radiation mechanisms: general  
radiation mechanisms: non-thermal  
radiation mechanisms: thermal  
radiative transfer  
relativistic processes  
scattering  
shock waves  
solid state: refractory  
solid state: volatile  
turbulence  
waves

## Physical data and processes

acceleration of particles  
accretion, accretion discs  
asteroseismology  
astrobiology  
astrochemistry  
astroparticle physics  
atomic data  
atomic processes  
black hole physics  
chaos  
conduction  
convection  
dense matter  
diffusion  
dynamo  
elementary particles  
equation of state  
gravitation  
gravitational lensing: micro  
gravitational lensing: strong  
gravitational lensing: weak  
gravitational waves  
hydrodynamics  
instabilities  
line: formation  
line: identification  
line: profiles  
magnetic fields  
magnetic reconnection  
*(magnetohydrodynamics)* MHD  
masers  
molecular data  
molecular processes  
neutrinos  
nuclear reactions, nucleosynthesis, abundances  
opacity  
plasmas  
polarization

**Astronomical instrumentation, methods and techniques**  
atmospheric effects  
balloons  
instrumentation: adaptive optics  
instrumentation: detectors  
instrumentation: high angular resolution  
instrumentation: interferometers  
instrumentation: miscellaneous  
instrumentation: photometers  
instrumentation: polarimeters  
instrumentation: spectrographs  
light pollution  
methods: analytical  
methods: data analysis  
methods: laboratory: atomic  
methods: laboratory: molecular  
methods: laboratory: solid state  
methods: miscellaneous  
methods: numerical  
methods: observational  
methods: statistical  
site testing  
space vehicles  
space vehicles: instruments  
techniques: high angular resolution  
techniques: image processing  
techniques: imaging spectroscopy  
techniques: interferometric  
techniques: miscellaneous  
techniques: photometric  
techniques: polarimetric  
techniques: radar astronomy  
techniques: radial velocities  
techniques: spectroscopic  
telescopes

## Astronomical data bases

astronomical data bases: miscellaneous  
atlases  
catalogues  
surveys  
virtual observatory tools

## Astrometry and celestial mechanics

astrometry  
celestial mechanics  
eclipses  
ephemerides  
occultations  
parallaxes  
proper motions  
reference systems  
time

## The Sun

Sun: abundances  
Sun: activity  
Sun: atmosphere  
Sun: chromosphere  
Sun: corona  
Sun: coronal mass ejections (CMEs)  
Sun: evolution  
Sun: faculae, plages  
Sun: filaments, prominences  
Sun: flares  
Sun: fundamental parameters  
Sun: general  
Sun: granulation  
Sun: helioseismology  
Sun: heliosphere  
Sun: infrared  
Sun: interior  
Sun: magnetic fields  
Sun: oscillations  
Sun: particle emission  
Sun: photosphere  
Sun: radio radiation  
Sun: rotation  
*(Sun:)* solar–terrestrial relations  
*(Sun:)* solar wind  
*(Sun:)* sunspots  
Sun: transition region  
Sun: UV radiation  
Sun: X-rays, gamma-rays

## Planetary systems

comets: general

### comets: individual: . . .

Earth  
interplanetary medium  
Kuiper belt: general

### Kuiper belt objects: individual: . . .

meteorites, meteors, meteoroids  
minor planets, asteroids: general

### minor planets, asteroids: individual: . . .

Moon

Oort Cloud  
planets and satellites: atmospheres  
planets and satellites: aurorae  
planets and satellites: composition  
planets and satellites: detection  
planets and satellites: dynamical evolution and stability  
planets and satellites: formation  
planets and satellites: fundamental parameters  
planets and satellites: gaseous planets  
planets and satellites: general

### planets and satellites: individual: . . .

planets and satellites: interiors  
planets and satellites: magnetic fields  
planets and satellites: oceans  
planets and satellites: physical evolution  
planets and satellites: rings  
planets and satellites: surfaces  
planets and satellites: tectonics  
planets and satellites: terrestrial planets  
planet–disc interactions  
planet–star interactions  
protoplanetary discs  
zodiacal dust

## Stars

stars: abundances  
stars: activity  
stars: AGB and post-AGB  
stars: atmospheres  
*(stars:)* binaries (*including multiple*): close  
*(stars:)* binaries: eclipsing  
*(stars:)* binaries: general  
*(stars:)* binaries: spectroscopic  
*(stars:)* binaries: symbiotic  
*(stars:)* binaries: visual  
stars: black holes  
*(stars:)* blue stragglers  
*(stars:)* brown dwarfs  
stars: carbon  
stars: chemically peculiar  
stars: chromospheres  
*(stars:)* circumstellar matter  
stars: coronae  
stars: distances  
stars: dwarf novae  
stars: early-type  
stars: emission-line, Be  
stars: evolution  
stars: flare  
stars: formation  
stars: fundamental parameters  
*(stars:)* gamma-ray burst: general  
*(stars:)* **gamma-ray burst: individual: . . .**  
stars: general  
*(stars:)* Hertzsprung–Russell and colour–magnitude diagrams  
stars: horizontal branch  
stars: imaging  
**stars: individual: . . .**  
stars: interiors

stars: jets  
 stars: kinematics and dynamics  
 stars: late-type  
 stars: low-mass  
 stars: luminosity function, mass function  
 stars: magnetars  
 stars: magnetic field  
 stars: massive  
 stars: mass-loss  
 stars: neutron  
*(stars:)* novae, cataclysmic variables  
 stars: oscillations (*including pulsations*)  
 stars: peculiar (*except chemically peculiar*)  
*(stars:)* planetary systems  
 stars: Population II  
 stars: Population III  
 stars: pre-main-sequence  
 stars: protostars  
*(stars:)* pulsars: general  
***(stars:)* pulsars: individual: ...**  
 stars: rotation  
 stars: solar-type  
*(stars:)* starspots  
 stars: statistics  
*(stars:)* subdwarfs  
*(stars:)* supergiants  
*(stars:)* supernovae: general  
***(stars:)* supernovae: individual: ...**  
 stars: variables: Cepheids  
 stars: variables: Scuti  
 stars: variables: general  
 stars: variables: RR Lyrae  
 stars: variables: S Doradus  
 stars: variables: T Tauri, Herbig Ae/Be  
*(stars:)* white dwarfs  
 stars: winds, outflows  
 stars: Wolf-Rayet

**Interstellar medium (ISM), nebulae**

ISM: abundances  
 ISM: atoms  
 ISM: bubbles  
 ISM: clouds  
*(ISM:)* cosmic rays  
*(ISM:)* dust, extinction  
 ISM: evolution  
 ISM: general  
*(ISM:)* HII regions  
*(ISM:)* Herbig–Haro objects

**ISM: individual objects: ...**

*(except planetary nebulae)*  
 ISM: jets and outflows  
 ISM: kinematics and dynamics  
 ISM: lines and bands  
 ISM: magnetic fields  
 ISM: molecules  
*(ISM:)* photodissociation region (PDR)  
*(ISM:)* planetary nebulae: general  
***(ISM:)* planetary nebulae: individual: ...**  
 ISM: structure  
 ISM: supernova remnants

**The Galaxy**

Galaxy: abundances  
 Galaxy: bulge  
 Galaxy: centre  
 Galaxy: disc  
 Galaxy: evolution  
 Galaxy: formation  
 Galaxy: fundamental parameters  
 Galaxy: general  
*(Galaxy:)* globular clusters: general  
***(Galaxy:)* globular clusters: individual: ...**  
 Galaxy: halo  
 Galaxy: kinematics and dynamics  
*(Galaxy:)* local interstellar matter  
 Galaxy: nucleus  
*(Galaxy:)* open clusters and associations: general  
***(Galaxy:)* open clusters and associations: individual: ...**  
*(Galaxy:)* solar neighbourhood  
 Galaxy: stellar content  
 Galaxy: structure

**Galaxies**

galaxies: abundances  
 galaxies: active  
*(galaxies:)* BL Lacertae objects: general  
***(galaxies:)* BL Lacertae objects: individual: ...**  
 galaxies: bulges  
 galaxies: clusters: general

**galaxies: clusters: individual: ...**

galaxies: clusters: intracluster medium  
 galaxies: distances and redshifts  
 galaxies: dwarf  
 galaxies: elliptical and lenticular, cD  
 galaxies: evolution  
 galaxies: formation  
 galaxies: fundamental parameters  
 galaxies: general  
 galaxies: groups: general

**galaxies: groups: individual: ...**

galaxies: haloes  
 galaxies: high-redshift

**galaxies: individual: ...**

galaxies: interactions  
*(galaxies:)* intergalactic medium  
 galaxies: irregular  
 galaxies: ISM  
 galaxies: jets  
 galaxies: kinematics and dynamics  
*(galaxies:)* Local Group  
 galaxies: luminosity function, mass function  
*(galaxies:)* Magellanic Clouds  
 galaxies: magnetic fields  
 galaxies: nuclei  
 galaxies: peculiar  
 galaxies: photometry  
*(galaxies:)* quasars: absorption lines  
*(galaxies:)* quasars: emission lines  
*(galaxies:)* quasars: general

(galaxies;) **quasars: individual:** . . .  
(galaxies;) quasars: supermassive black holes  
galaxies: Seyfert  
galaxies: spiral  
galaxies: starburst  
galaxies: star clusters: general

**galaxies: star clusters: individual:** . . .  
galaxies: star formation  
galaxies: statistics  
galaxies: stellar content  
galaxies: structure

ultraviolet: general  
ultraviolet: ISM  
ultraviolet: planetary systems  
ultraviolet: stars  
X-rays: binaries  
X-rays: bursts  
X-rays: diffuse background  
X-rays: galaxies  
X-rays: galaxies: clusters  
X-rays: general  
**X-rays: individual:** . . .  
X-rays: ISM  
X-rays: stars

### Cosmology

(cosmology;) cosmic background radiation  
(cosmology;) cosmological parameters  
(cosmology;) dark ages, reionization, first stars  
(cosmology;) dark energy  
(cosmology;) dark matter  
(cosmology;) diffuse radiation  
(cosmology;) distance scale  
(cosmology;) early Universe  
(cosmology;) inflation  
(cosmology;) large-scale structure of Universe  
cosmology: miscellaneous  
cosmology: observations  
(cosmology;) primordial nucleosynthesis  
cosmology: theory

### Resolved and unresolved sources as a function of wavelength

gamma-rays: diffuse background  
gamma-rays: galaxies  
gamma-rays: galaxies: clusters  
gamma-rays: general  
gamma-rays: ISM  
gamma-rays: stars  
infrared: diffuse background  
infrared: galaxies  
infrared: general  
infrared: ISM  
infrared: planetary systems  
infrared: stars  
radio continuum: galaxies  
radio continuum: general  
radio continuum: ISM  
radio continuum: planetary systems  
radio continuum: stars  
radio continuum: transients  
radio lines: galaxies  
radio lines: general  
radio lines: ISM  
radio lines: planetary systems  
radio lines: stars  
submillimetre: diffuse background  
submillimetre: galaxies  
submillimetre: general  
submillimetre: ISM  
submillimetre: planetary systems  
submillimetre: stars  
ultraviolet: galaxies